

LOW AMPLITUDE FATIGUE HARDENING  
OF COPPER SINGLE CRYSTALS

LOW AMPLITUDE FATIGUE HARDENING  
OF COPPER SINGLE CRYSTALS

by

DOUGLAS M. SHINOZAKI

A Thesis

Submitted to the Faculty of Graduate Studies  
in Partial Fulfilment of the Requirements  
for the Degree  
Master of Science

McMaster University

October 1968

MASTER OF SCIENCE (1968)  
(Metallurgy and Materials Science)

McMASTER UNIVERSITY  
Hamilton, Ontario

TITLE : Low Amplitude Fatigue Hardening of Copper Single Crystals

AUTHOR: Douglas M. Shinozaki, B.Eng. (McMaster University)

SUPERVISOR: Professor J. D. Embury

NUMBER OF PAGES: (vi); 101

SCOPE AND CONTENTS:

The detailed dislocation microstructure was determined as a function of low amplitude fatigue in the hardening regime. Copper single crystals were cycled in uniaxial, symmetric push-pull at room temperature.

The dislocation microstructures were observed by thin film electron microscopy for various extents of hardening. An attempt was made to correlate surface slip line observations to the dislocation microstructures. On the basis of a similarity to the dislocation distributions observed in stage two of uni-directional work hardening, a model for fatigue hardening was proposed. Hirsch's stress relief theory of stage two work hardening was used to account for the observed dislocation distributions.

## ACKNOWLEDGMENTS

The work which is presented in this thesis does not reflect the many hours of experiment and discussion which were necessary. The author is sincerely grateful to Dr. J. D. Embury for his patient advice and guidance throughout these many hours. The constant interest which he showed in this work was an encouragement during the lean days of experimental difficulties.

Special thanks are due also to Dr. D. F. Watt who designed many of the experiments used in this thesis, and who lent his considerable experience to the author.

The author appreciates the work done on the drawings in his thesis, and the assistance in many other ways from Mr. Rick Jarachowicz.

And also, thanks to Mrs. Marilyn Foster for the accurate typing of this thesis in such a short time.

Finally, the author is indebted to his fellow members of the research group: Mike Schankula, Don Timbres and Bob Shewfelt; and to Roy Cornwell; for their advice and criticism through the months.

## TABLE OF CONTENTS

		<u>Page</u>
CHAPTER 1	INTRODUCTION	1
CHAPTER 2	LITERATURE REVIEW	4
2.1	Introduction	4
2.2	Work Hardening in Uni-directional Stage II	4
2.3	Particular Work Hardening Mechanisms for Stage II	5
2.4	Seeger's Long Range Stress Theory	6
2.5	Hirsch's Stress Relief Model	8
2.6	Summary of Work Hardening Models	10
2.7	Fatigue Hardening	10
2.8	Point Defect Theories of Fatigue Hardening	12
2.9	Dipole Debris Mechanisms	16
2.10	Other Recent Models	16
2.11	Dislocation Microstructures at Saturation	20
CHAPTER 3	EXPERIMENTAL PROCEDURE	22
3.1	Introduction	22
3.2	Growth of Copper Single Crystals	22
3.3	Square Crosssection Machining	24
3.4	Fatigue Adaptor	27
3.5	Single Crystal Dimension Measurements	27
3.6	Fatigue Cycling	28
3.7	Electropolishing	28

	<u>Page</u>	
3.8	Replica Techniques	29
3.9	Electron Microscopy	30
3.10	Outline of Procedure	32
CHAPTER 4	EXPERIMENTAL RESULTS	34
4.1	Introduction	34
4.2	Part I. Geometry and Density of Dislocations	37
4.3	Summary of Part I	57
4.4	Part II. Burgers Vector Pairs	59
4.5	Electron Micrographs of Sections Cut Parallel to $(\bar{1}01)$ Planes	63
4.6	Summary of Part II	71
4.7	Part III. Slip Line Observations.	73
CHAPTER 5	DISCUSSION	76
5.1	Comparison to Other Theories	78
5.2	Proposed Model for Fatigue Hardening	82
5.3	Forest Dislocations as Initial Barriers to Slip	85
5.4	Stress Relief by Secondary Slip	87
5.5	Orientation of Braids	88
5.6	Dipoles in Hardening	90
5.7	The Saturated State	91
5.8	Dislocation Microstructure and Strain Amplitude	92
5.9	Experimental Errors	93
5.10	Summary	95

	<u>Page</u>
CHAPTER 6      CONCLUSIONS	97
BIBLIOGRAPHY	100
APPENDIX I      Formation of Dipoles	
APPENDIX 2      Burgers Vector Analyses	
APPENDIX 3      Calculations	

## CHAPTER 1

### INTRODUCTION

Fatigue is most often associated with a fracture which results from the application of alternating stresses which are substantially less than the nominal fracture stress. The major part of the literature on fatigue has been concerned with fatigue fracture and its engineering applications. Only a small fraction of the published work, most of it recent, has contributed to an understanding of a dislocation model on fatigue.

The postulation of a reasonable dislocation theory on fatigue is important for developing a more fundamental understanding of practical engineering problems in cyclic straining. In addition, such a theory would allow direct comparison to dislocation theories in other modes of metallic deformation. The result would be a more complete and coherent picture of the dislocation mechanisms in the broad problem of fracture.

If we stress a crystal in such a way that the plastic strain we introduce into the crystal is constant over each half cycle (plastic strain range), the peak stress will increase on each cycle. This hardening effect will be very rapid in the first few tens of cycles (if the plastic strain amplitude is "low") but gradually taper off until no hardening occurs on further cycling. The initial period is termed the "rapid hardening" stage, while the final period of zero hardening is

termed the "saturated state". The period between these two is a transition region.

The rate of hardening, and the peak stress reached in the saturated state, depend on the plastic strain "amplitude" ( $\frac{1}{2}$  of the plastic strain range). The higher the plastic strain amplitude, the higher is the final state peak stress, and the faster the rate of hardening (Kemsley and Paterson 1960). The arbitrary definition of what "low amplitude" fatigue encompasses will be explained in the text.

This description of fatigue suggests that there are two stages which may be considered in an investigation: the saturated state and the hardening state.

The saturated state has been examined very carefully (Watt 1967) but the hardening has not. In addition, although considerable qualitative work has been reported on the saturated state dislocation microstructure, very little quantitative work has been done because of the complexity of the observed microstructure.

A careful study of the hardening state, particularly the dislocation microstructure, would be useful not only in defining the mechanism of hardening in fatigue, but also in revealing how the saturated state microstructure is generated. A knowledge of the origins of the saturated state would yield further information on the dislocation arrangement at saturation.

The problem was therefore to develop a model for fatigue hardening based on experimental results. The philosophy of the experimental technique was to derive the maximum information out of a simple system.

Because of the extensive literature available on the uni-directional work hardening in copper single crystals, this system was chosen for study in fatigue hardening. This allowed comparison of experimental results, particularly dislocation microstructures, between the two types of hardening.

The copper single crystals were grown in an orientation which in uni-directional deformation was considered a "single slip orientation". These were then cycled in the low amplitude regions (to permit direct comparison to Watt's results) to various numbers of cycles in the hardening stage. The dislocation microstructures of each sample were quantitatively examined by electron microscopy. Surface observations were also made in an attempt to correlate these with the observed dislocation microstructures.

In this way, a consistent dislocation model for fatigue hardening was developed from the detailed experimental results.

## CHAPTER 2

### Literature Review

#### 2.1 Introduction

The problem of fatigue hardening poses two questions: firstly, what is the nature of the barriers to slip, and secondly, how can such barriers be generated by reverse straining. The nature of the barriers can be determined unambiguously by direct observations of thin films in the electron microscope. The second problem is primarily an exercise in imagination and ingenuity combined with a knowledge of present hypotheses on dislocation mechanisms and an adequate interpretation of the direct observations of the nature of the barriers.

This literature review is therefore used to examine the present hypotheses on dislocation interactions which are pertinent to fatigue hardening.

#### 2.2 Work Hardening in Unidirectional Stage II

The stress-strain curve for uni-directionally deformed single crystal copper shows three distinct stages. An "easy glide" region of low hardening rate, a second stage which has a high and linear rate of hardening, and a third stage which shows a parabolic decrease in the rate of hardening.

For reasons which become clear later in this work, the linear hardening stage two dislocation mechanisms were of particular interest.

The principal dislocation theories which attempt to explain linear work hardening (where "work" hardening refers to uni-directional effects) depend on either long range elastic interactions or short range interactions (such as cutting of forest dislocations, etc). It is generally accepted that the dislocation microstructure of stage II is characterized by the presence of a significant proportion of secondary dislocations (Basinski and Basinski 1964) corresponding to activity on secondary systems (Clarebrough and Hargreaves, 1959). However, this slip activity must be limited in extent since x-ray diffraction and shape change studies show that almost all strain is carried by the primary system.

The dislocation microstructure has been examined in the electron microscope by various experimentors. In particular, some excellent micrographs have been published by Basinski (1964), Steeds and Hazzledine (1964) and Hirsch (1963). All of these show the dislocations of the primary and secondary systems to be concentrated into narrow, elongated regions which appear similar in form to "braids". The internal structure of the braids is in general, extremely complex in the later stages of linear hardening, and only proportional amounts of primary and secondary dislocations can be estimated. Individual Burgers vectors and isolated interactions in the braids cannot be distinguished at these later stages. Basinski and Basinski (1964) show that the density of secondary dislocations in copper single crystals is comparable to that of primary dislocations throughout stage II.

### 2.3 Particular Work Hardening Mechanisms for Stage II

It is important to realize that there is still considerable

controversy in work hardening concerning the dislocation interactions responsible for the hardening. The macroscopic effects, such as slip line behaviour, magnetic effects (Kronmüller 1967), shape changes, back reflection x-ray diffraction results, stress-strain curve relationships (for changing temperature, strain rate, etc.) have been used by some investigators (Seeger, Kronmüller, et al.) to develop a self-consistent long range stress theory of work hardening. Their skepticism about the validity of thin film electron microscope observations has limited their use of direct observation of dislocation interactions and hence limited the detail to which they can describe the dislocation microstructures generated by their mechanisms.

The fundamental experimental difference therefore, between Seeger's school of thought and Hirsch's group has been the much more heavy reliance of Hirsch et al. on electron microscope observations. The relative merits of either argument appear to be quite evenly balanced.

It is generally assumed that electron microscope observations are reliable, at least to the extent of illustrating the geometry of obstacles and their composition although not necessarily in explicitly showing the dislocation interactions which cause hardening.

The following section gives an outline of the important characteristics of each theory of work hardening in stage II, starting with Seeger's theory and ending with Hirsch's most recent attempt.

#### 2.4 Seeger's Long Range Stress Theory (Seeger 1963)

Seeger assumes that the flow stress is determined by the maximum internal stress that has to be overcome in passing a dislocation through

the softest region of the crystal (that is: halfway between neighbouring pile-ups of dislocations). The existence of some form of infinitely strong barriers (for example, Lomer-Cottrell locks) is initially assumed. The pile-ups of primary dislocations against these barriers can be approximated by a continuous distribution or "a giant dislocation of Burgers vector  $nb$ ". By analogy to the stress necessary to pass a single edge dislocation between two other edge dislocations of the same sign, Seeger calculates the stress necessary to pass a single edge between the two pile-ups approximated by two "giant" dislocations. This passing stress is then the flow stress required for the long range stress theory.

Hirsch (1967) effectively argues against this model in the following manner. The plotted stress fields of dislocation pile-ups show that if the pile-up is formed by a stress  $\tau_a$  ( $\approx$  flow stress) then the internal stress at some distance from the pile-up is always less than  $\tau_a$ . A dislocation passing such a pile-up therefore always sees an opposing stress which is less than  $\tau_a$  and hence would pass through without being completely blocked. The internal long range stress fields of pile-ups cannot therefore determine the flow stress unaided by some other mechanism. Even the calculation of backstresses generated by interacting internal stresses of pile-ups shows that the backstress from the pile-ups never exceeds the stress at which they were formed.

However, it should be noted that if the pile-ups are close enough, it appears that the short range backstress from individual dislocations can now exceed the stress at which pile-ups were formed. Such a theory can possibly generate a form of linear work hardening, but long range stresses alone cannot.

## 2.5 Hirsch's Stress Relief Model

The rationale which appears to have the greatest validity was suggested by Hirsch (1964) and explained in detail three years later (Hirsch (1967)). The general description of the model and its consequence is as follows:

Stage I deformation produces some kind of barriers to slip. The commencement of Stage II corresponds to the relieving of internal stresses of pile-ups of primary dislocations by secondary slip. The complex tangles in the regions of these initial tangles become even more effective barriers to slip resulting in a hardening effect. The strain is still largely carried by primary dislocations since the slip distance of secondary dislocations is very small.

The ease with which secondary sources are activated in the process of stress relief determines the extent and effectiveness of the obstacle to primary slip. Thus the orientation and other parameters affecting the ease with which such sources are operated determine the hardening rate.

One would therefore expect that the density of all dislocations would decrease with distance from the centre (or initiating line of tangling) and the generated obstacles would be ribbon-like with a width approximately equal to the pile-up length and thickness equal to the "stopping" cross-section of the obstacle.

The hardening mechanism is explained in the following way. The mean free path of dislocations determines the amount of plastic strain per slip line and also the increase in primary dislocation density. The

mean free path is in turn determined by the density and radius of obstacles. When the obstacle density and radius as generated by Stage I work hardening become great enough, the mean free path is small enough that sufficient numbers of primary dislocations pile up at these obstacles to produce an appreciable internal stress at the head of the pile-up. The internal stresses so produced, together with the appropriate component of the applied stress eventually generate secondary dislocations. The obstacle radius is effectively increased and this leads to hardening of potential primary sources.

The amount of secondary slip therefore determines the mean free path and the extent of hardening. This explains why the ease with which secondary sources operate is important to the rate of hardening.

Hirsch proposes that the applied stress has the effect of increasing the number of slip lines and decreasing the scale of the microstructure, but does not cause the nature of the structure to change, which remains fundamentally the same as that at the beginning of Stage II.

The barriers, even though they are basically the same as at the first of Stage II, become more effective obstacles not only because they grow in size, but also because the secondary slip gives rise to an increased dislocation density in the tangle, which makes the obstacle more effective in stopping dislocations.

The most important result of Hirsch's model in relation to fatigue hardening is that it predicts a high density of secondary dislocations, comparable to the primary density, which is localized in the immediate neighbourhood of the initial obstacles to slip.

## 2.6 Summary of Work Hardening Models

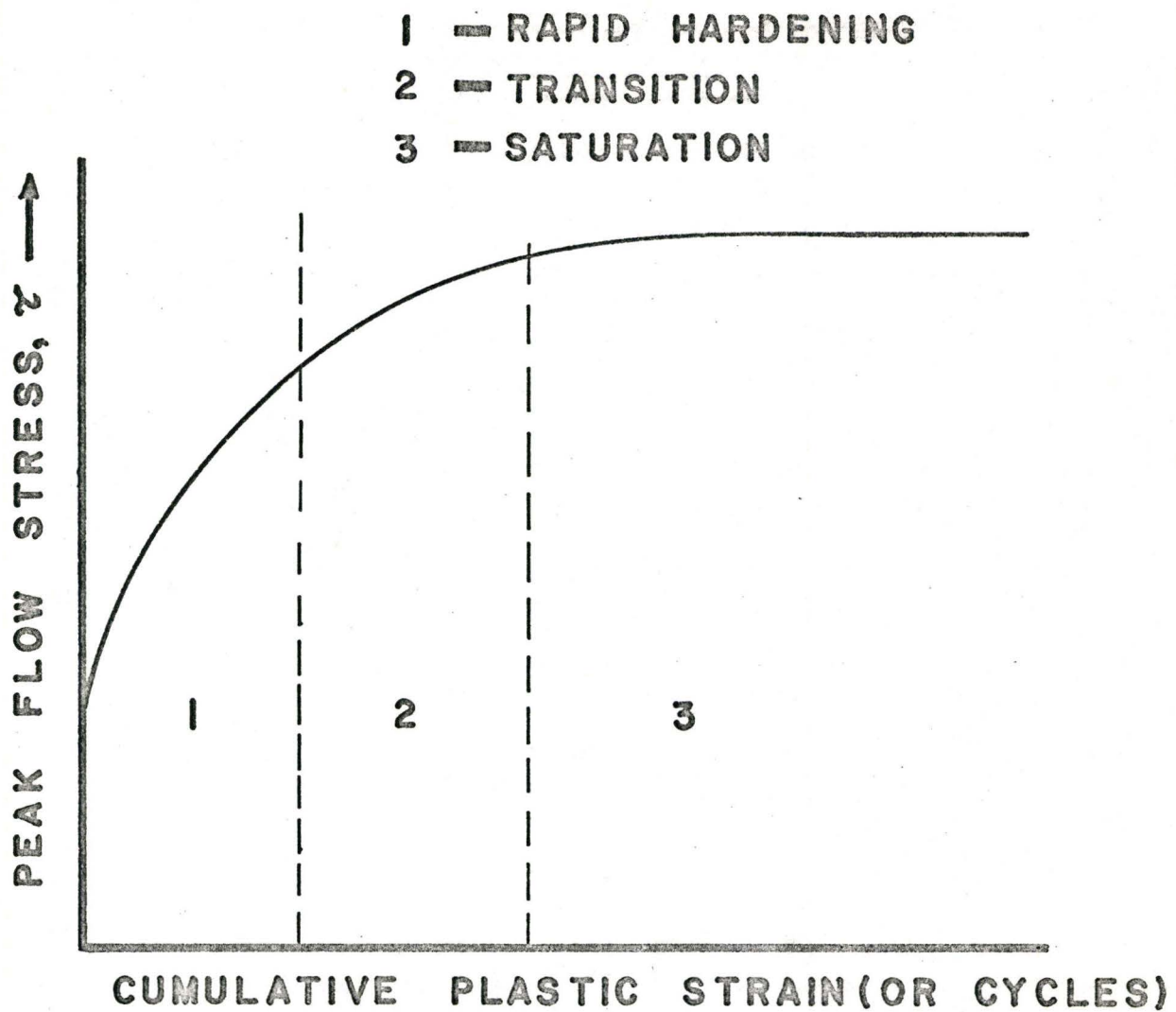
The models which have been proposed for Stage II unidirectional work hardening are very specific and predict experimentally verifiable results. The basis upon which they have been developed is very substantial. Reference to reviews in work hardening such as that given by Holt, Nabarro and Basinski (1964) shows that the experimental work which has been performed in work hardening has been extremely consistent. Much of the work has been done on single crystal copper deformed in uniaxial tension. The use of such a simple system by many of the workers in the field has made available a large quantity of comparable results. The models can therefore be developed in a much more detailed manner using the considerable data present in the literature.

## 2.7 Fatigue Hardening

### 2.7.1 Introduction

In contrast to the detailed models built on substantial experimental evidence found in work hardening, there are considerably more general models based on much less experimental evidence in fatigue hardening. In addition, the experimental results available in fatigue are often the product of non-comparable techniques (see Discussion).

The greater part of the literature on fatigue deals mainly with the saturated state and not the hardening state. (In cycling at constant plastic strain, the initial cycles show a rapidly increasing peak stress while the later cycles (1,000 cycles onwards in low amplitude fatigue) show very little increase in peak stress: this later period is known as the saturated state. The various stages are shown in Figure 2.1). The



SCHEMATIC OF A CYCLIC STRAIN —  
HARDENING CURVE.

FIGURE — 2.1

FROM FELTNER — (1965).

literature which deals with the saturated state behaviour of metals can be found reviewed in a complete manner in Watt's Ph.D. thesis (1967).

There are two kinds of mechanisms which have been proposed in the past to explain fatigue hardening. The first kind utilizes point defects such as vacancies and interstitials in various ways, while the second suggests dipole "debris" are the significant elements in hardening. These two sorts of mechanisms will be considered first, and some other postulations which do not fit either category will be added later.

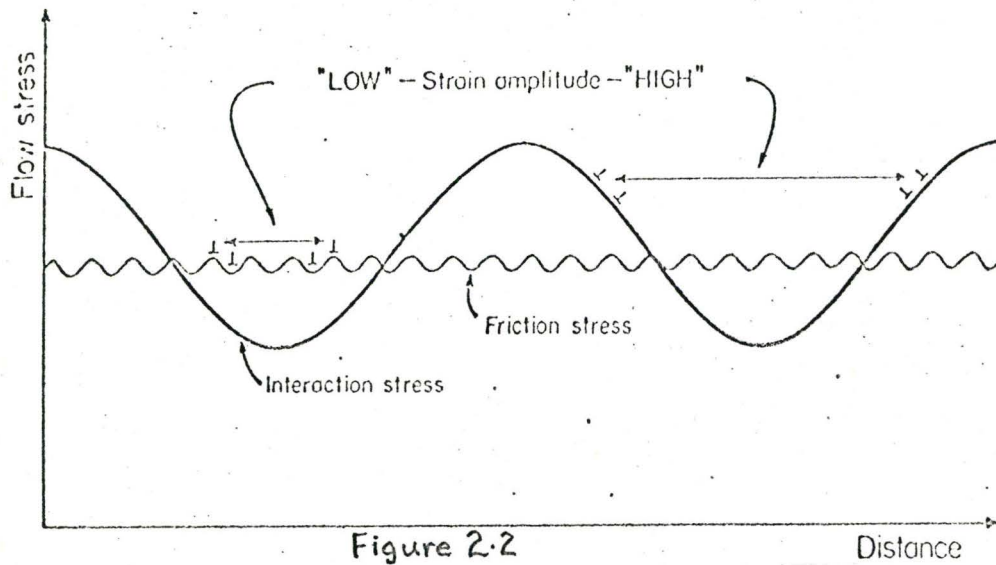
## 2.8 Point Defect Theories of Fatigue Hardening

In the point defect theories, there are two basic types. The first was suggested by Broom and Ham (1957). This involved the diffusions of point defects to dislocations, producing jogs in the case of vacancies and impurity "atmospheres" in the case of interstitials. Either jogs or atmospheres would reduce the ease with which dislocations move in the matrix. Alternatively, the point defects conglomerate into vacancy clusters which act as particles to harden the metal. No definite experimental evidence was shown by Broom and Ham to verify these proposals; however in 1959, they elaborated upon their original model. They suggested that the large temperature dependence of the yield stress indicated a thermally activated process such as the movement of jogs, the unpinning of dislocations from "atmospheres" or the cutting of small obstacles by glide dislocations. The hardening was capable of being "aged" into the crystal by warming a sample fatigued at 78°K to 293°K and allowing the point defects to diffuse to the dislocation, jogging them or pinning them with atmospheres.

Utilizing point defects in a different way, Avery and Backofen (1963) proposed a more elaborate model for fatigue hardening. This was based on some experimental results obtained by cycling metals of various stacking fault energies (cycled under a constant deflection bending strain). The experimental results were classified into two categories: one relating to the mechanical response of the samples in the hardening regime; the other to surface slip behaviour.

The four point bending procedure and the observation of cumulative slip lines make the second set of results quite difficult to interpret in terms of hardening behaviour. However, the first set of results is quite significant. These showed that the overall rate and extent of hardening decrease with decreasing stacking fault energy. In addition, the hardening characteristics are dependent primarily upon stacking fault energy and not very directly upon the operative slip systems, grain boundaries, and so on.

The similarity of polycrystal and single crystal work hardening rates is explained in terms of the primary hardening obstacles being point defects. Avery and Backofen suppose that the internal stress is a sum of the dislocation pile-up and tangle stresses which are of "long wavelength" and a friction stress of "short wavelength" due to point defects. At low amplitudes, the mean free path for dislocations between the long wavelength peaks is much longer than the actual path length of the glide dislocations. The hardening is therefore controlled by the short wavelength stress field (due to point defects). The schematic of this "wavelength" theory is shown in Figure 2.2.



Thus, the rate of hardening was thought to depend on the rate of dislocation loop formation, which depends on the rate of point defect formation. The point defects arise from the dragging of jogs behind screw dislocations. Notice that the jogging process is not the hardening mechanism, but is only a part of it. In fact, this meant that as the stacking fault energy decreased, the rate of vacancy formation decreased (since there were

fewer jogs), the rate of loop formation decreased, and finally the hardening rate decreased.

Avery and Backofen further suggested that the approach to saturation may be explained by the onset of dynamic recovery processes (cross-slip, or "sweeping up" of point defect obstacles) which eventually balance the hardening processes. The alternative, they say, is that the plastic strain becomes reversible, as would be the case for dislocations bowing back and forth between pinning points.

Recently, Nine and Kuhlmann-Wilsdorf (1967) published an explanation for the dislocation microstructure. It was developed primarily to account for persistent slip bands, a saturated state phenomenon in which bands of slip lines and intrusions and extrusions are formed with clear areas of no slip activity between the bands.

The hardening in this rationale is again thought to be due to point defect "debris" - dislocation interaction. Cell walls are the result of "sweeping up" of debris by moving dislocations in the manner suggested by Sharp and Makin (1964). (In this mechanism, Sharp and Makin show by calculation that a dipole can be trapped in the vicinity of a dislocation of the same Burgers vector, and in fact can be "swept" along with the dislocation if it moves). This process produces clear areas which separate regions of high dislocation density. The cyclic straining generates a series of twist walls with an axis of rotation parallel to the slip plane normal. Tilt boundaries form perpendicular to the slip plane and the elimination of some tilt walls by cell rotation results in dislocation free channel from which persistent slip bands are formed.

## 2.9 Dipole Debris Mechanism of Hardening

In 1965, Feltner proposed a hardening rationale which contained a specific hardening mechanism and some calculations explaining it. His model for hardening was one which assumed that the barriers to slip are the prismatic dislocation loops formed during the early straining of the crystal. The moving screw dislocations generated loops in the manner suggested by Fourie and Murphy (1962). Such debris builds up in density until the screws responsible for carrying the strain initially, become entirely pinned by the loops. As this state is approached, the loops themselves rather than the long dislocations become the strain carrying elements. The saturated state is simply described as that where the dipoles carry the total strain by a "flip-flop" mechanism (Figure 2.3) suggested by Gilman (1963), and therefore is that state where no further hardening (characterized by the production of debris) occurs. The temperature dependence of the saturated state flow stress is explained by the temperature dependent point defect-loop interaction where the point defects are generated by the short movement of jogged screws at saturation.

## 2.10 Other Recent Fatigue Hardening Models

Kettunen (1967) has performed some constant stress fatigue hardening tests and postulated a mechanism for hardening based on some electron microscopy and surface metallography.

He suggested that small stress amplitudes resulted in an almost entirely reversible strain at saturation. At higher strains, however, the hysteresis loop opens out and plastic strain is evident.

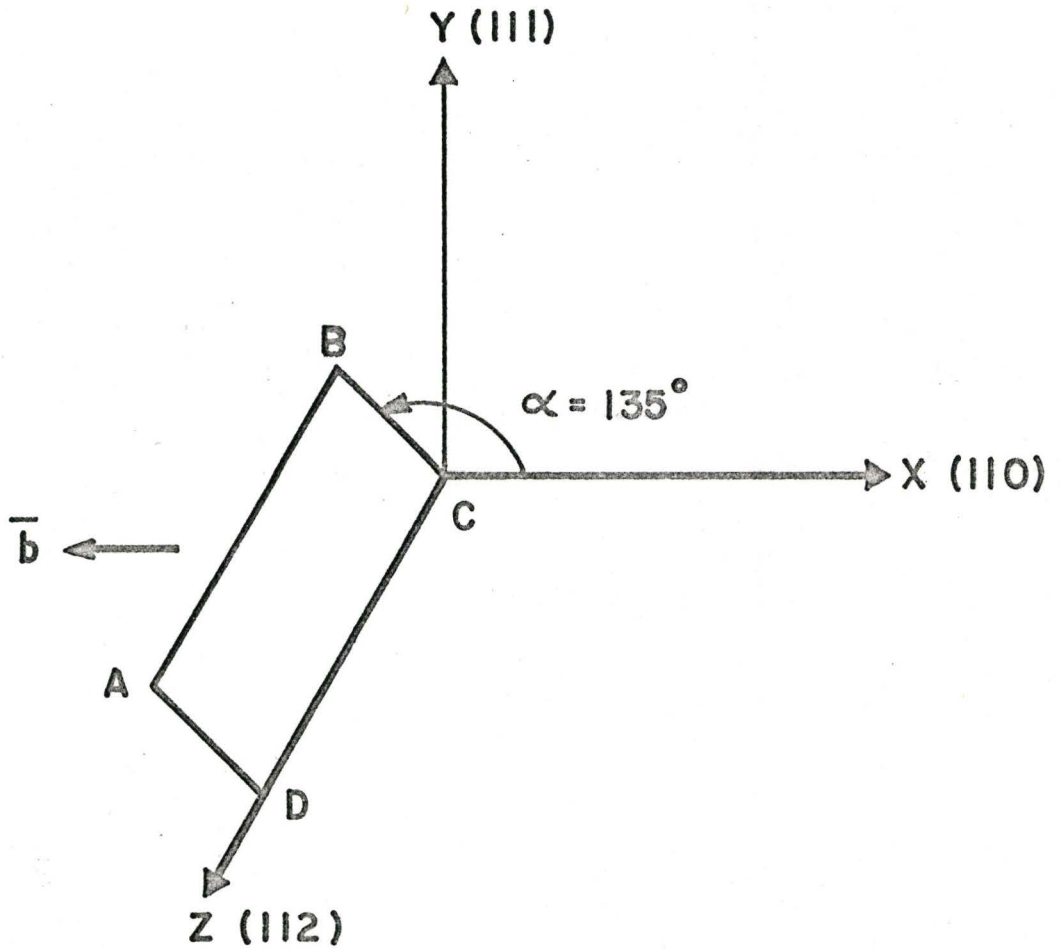


FIGURE- 2.3

EQUILIBRIUM POSITION OF A  
DIPOLE IN A FACE-CENTERED CUBIC  
CRYSTAL (FELTNER - 1965).

The metallographic results show similarities to unidirectional deformation at corresponding stresses. A cell structure is evident at higher amplitudes, while a mat structure parallel to the primary slip plane is visible at lower amplitudes.

The fatigue hardening phenomenon is related to the forest dislocations as obstacles, however no detailed model for hardening is suggested.

The most recent significant work was published by Hancock and Grosskreutz (1968). The strain amplitude they used was in the intermediate to high amplitude region, and the results must be interpreted accordingly. Basically, over the first 100 cycles, they determined that number of dislocation bundles per unit volume increases, the density of dislocations within the bundles increases, the length of primary dipoles decreases and the number of  $\langle 110 \rangle$  faulted dipoles decreases. (These are Frank dislocations lying along  $\langle 110 \rangle$  directions).

They propose that initial hardening is due to parallel interaction of edge dislocations on nearly slip planes which form dipoles and multipoles. These bundles of primary dislocations grow with cycling and reduce the mean free path of the strain carrying dislocations (moving between the bundles). To accommodate the strain, the density of mobile dislocations increases and further growth of the bundles results in dislocation walls which are stabilized by  $\langle 110 \rangle$  faulted dipoles near the walls.

Secondary dislocations are generated which cut the bundles of primary dislocations and vice versa resulting in more effective obstacles

to plastic flow.

Hancock and Grosskreutz suggest that the plastic strain can be carried by the "flip-flop" motion of dipoles (as suggested by Feltner) combined with the movement of dislocations between the bundles.

Perhaps more important than their hardening mechanisms, are their actual experimental results. Their electron microscope pictures show that the braids or bundles are aligned along the traces of the critical and conjugate planes and along the primary edge direction. It is rather difficult to see the extent of this alignment over the larger part of the crystal, the isolated areas shown (at high magnification) show some such results, but some ambiguity in their interpretation is still present.

At 100 cycles, the excellent low magnification composite in the (111) plane shows that the longer well defined bundles lie along the trace of the conjugate plane with some along the primary edge direction and relatively few along the trace of the critical plane. The braids at 100 cycles are still very ragged in appearance, and the cellular appearance to the arrangement is not completely defined in the thinner regions of the foil. The thicker regions near the edge of the micrograph seem to show a more highly developed appearance.

The sections taken perpendicular to the primary slip direction show edge dislocations and dipoles aligned largely along the trace of the primary plane with some forest dislocations of undetermined Burgers vector present.

At 100 cycles, these sections show an extremely regular array of narrow bundles aligned along the trace of the primary plane, with some

regions of almost mat-like appearance.

### 2.11 Dislocation Microstructures at Saturation

Segall and Partridge (1959) reported that a cell structure similar to that found in tensile tests were found in aluminum polycrystals cycled at high amplitudes (high and low amplitudes are quite arbitrarily defined by many experimenters, but in this case and in all the cases where it is used henceforth, high amplitudes refers to that strain amplitude at which a very clearly defined cell structure of quite small cell size is seen in the dislocation microstructure; low amplitude refers to that which does not show such a cell structure).

On the other hand, at low amplitudes, Segall and Partridge found no cells but only "clusters" of dipoles and dislocations with clearly defined boundaries.

In 1963, Grosskreutz and Waldon found that the cell size formed in the high amplitude region was an inverse function of the strain amplitude.

Pratt, (1967) has found a similar relationship and has derived a simple function which describes his results.

In 1962, Segall, Partridge and Hirsch identified the microstructure of metals fatigued at low strain amplitudes as dense clusters of dipoles. They found no dislocation microstructures peculiar to the persistent slip bands.

However, Laufer and Roberts (1966) have shown that "ladder-like" structures appear to be associated with persistent slip bands while the larger part of the matrix consists of dense dipole clumps. (It should

be noted that these tests were carried out in the bending mode while Segall et al. have used uniaxial fatigue).

Lukas et al. (1966) likewise show a structure peculiar to persistent slip bands. In this case they show "channels" of dislocation free matrix penetrating into the specimen from the surface.

In general, all experimenters agree on the dipole "clump" description for the matrix structure without performing Burgers vector analysis on the clumps to determine their composition. There is some discrepancy among them whether the persistent slip bands are a surface representation of internal dislocation arrangements.

## CHAPTER 3

### EXPERIMENTAL PROCEDURE

#### 3.1 Introduction

The basic purpose of this investigation was to determine the detailed dislocation microstructure as a function of fatigue deformation. Thus the experimental procedure was developed to enable both slip line observations and thin film electron microscopy to be employed on a series of specimens of identical orientation.

#### 3.2 Growth of Copper Single Crystals

In order to isolate and identify the possible dislocation interactions responsible for hardening at various stages, and to eliminate the obvious difficulties involved with altering the stress distribution among the various slip systems, a series of identically oriented single crystals was necessary.

The crystals were grown as a single long cylinder in one mould. The OFHC copper was of 99.995% nominal purity, supplied by M & T Metal Company Ltd., Hamilton, Ontario, Canada. The mould was 17 3/4" long with a 7/16" diameter hole bored into the 3/4" O.D. solid high purity graphite rod. The bored hole was extended only to within 1/4" of the bottom of the mould, so it remained in one piece and no leakage problems would be encountered. The pointed bottom was obtained from the pointed tip of the drill used to bore out the rod.

The high temperatures involved in the growth, and the relatively large weight of the copper charge and graphite mould made the support of the mould a problem. After Kanthal wire and quartz rod were found unsatisfactory, a graphite rod 1/2" in diameter was threaded into the top of the mould to support the mould through the hot zone of the furnace.

This assembly was lowered slowly through a vertical tube furnace kept at 1200°C, in a reverse flow of nitrogen gas. No seeds were used, since any orientation other than ones near the 001,  $\bar{1}11$  symmetry line of the standard projection were thought acceptable.

The result was a crystal about 12.5 inches long which was subsequently checked for grain boundaries in an  $\text{FeCl}_3$  etch described by Barrett (1959) (1 part HCl, 1 part  $\text{HO}_2$  saturated with  $\text{FeCl}_3 \cdot 6\text{H}_2\text{O}$ ). Alternate immersion in this solution and a 40% solution of nitric acid resulted in a surface which clearly showed the crystallographic planes with different reflectivities.

As an additional check, each end of the 12.5 inch crystal and 5 points along a given line along the crystal were checked by Laue back reflection x-ray patterns (accurate to about  $\pm 3^\circ$ ).

Both the etching procedure and the x-ray results showed that the sample was a single crystal of experimentally identical orientation throughout. (The orientation can be seen in Figure 4.1).

The single crystal was then sealed in vacuum and annealed for 24 hours at 950°C preceded by slow heating (100°C/hour) and slow cooling (furnace cooling).

### 3.3 Square Crosssection Machining

From the 12.5 inch single crystal, five pieces 2.5 inches long were cut by spark cutting on the Servomet sparkcutter on range .5. End on Laue patterns were used to orient the crystal so that the primary slip direction  $[\bar{1}01]$  emerged in a vertical plane parallel to the longitudinal axis. The top face (Figure 3.1) of the gauge length was machined into the centre of the cylindrical crystal by spark planing with a tool 1 inch in diameter. The flat face of the gauge length was then set in a vertical plane using set squares and the second face was machined in, perpendicular to the first face. In this way four faces were spark planed into the gauge length to equal depths.

The spark planed gauge lengths were then chemically and electrolytically polished to a depth of more than 1 mm. on each face. The surfaces were checked before and after polishing by Laue patterns. Considerable asterism was visible before, indicating damage due to spark cutting, but no asterism was detectable after polishing.

The samples were annealed individually in vacuum in quartz tubes at  $890^{\circ}\text{C} \pm 10^{\circ}\text{C}$  for 12 hours. Slow heating and slow cooling procedures were followed to minimize the dislocation content in the virgin crystals.

There were a number of reasons for using a square crosssection gauge length in this work. The primary consideration was in the ease with which slip lines could be measured directly without compensating for curvature of cylindrical specimens, etc. The flatness of the surface and the corresponding flatness of the replica made slip line length and height measurements more precise. (Slip line heights could be measured

over any portion of the replica for the square cross-section whereas the centre of the replica, where the primary slip direction emerged, was the only region where the slip lines would be at full height on the cylindrical specimen.

A second, practical reason for using square cross-sections is that cylindrical cross-sections involve a more difficult spark planing technique. The specimen to be planed must be mounted in a rotating chuck so that the planing tool would work away at the gauge length in a cylindrically symmetric manner. Mechanical irregularities in the rotating mechanism would lead to physical deformation of the specimen.

The alternative, of growing cylindrical gauge lengths into the initial single crystal, is a much more difficult procedure for a number of reasons. The graphite inserts used to produce the reduced cross-section of the gauge length must be carefully made to eliminate the possibility of extra nucleation points at the discontinuities in the curvature of the mould walls. In addition, cooling the crystal from just below the solidification point to room temperature results in differential contraction between the crystal and the mould. The graphite inserts therefore place a net tensile stress on the gauge length at room temperature and some dislocation multiplication can occur in the crystal. It was necessary to minimize the initial dislocation content in order to simplify the identification of dislocations due to fatigue deformation, especially very early in hardening.

The conclusion was that square cross-section gauge lengths offered several advantages, provided the damage introduced at the surface of the

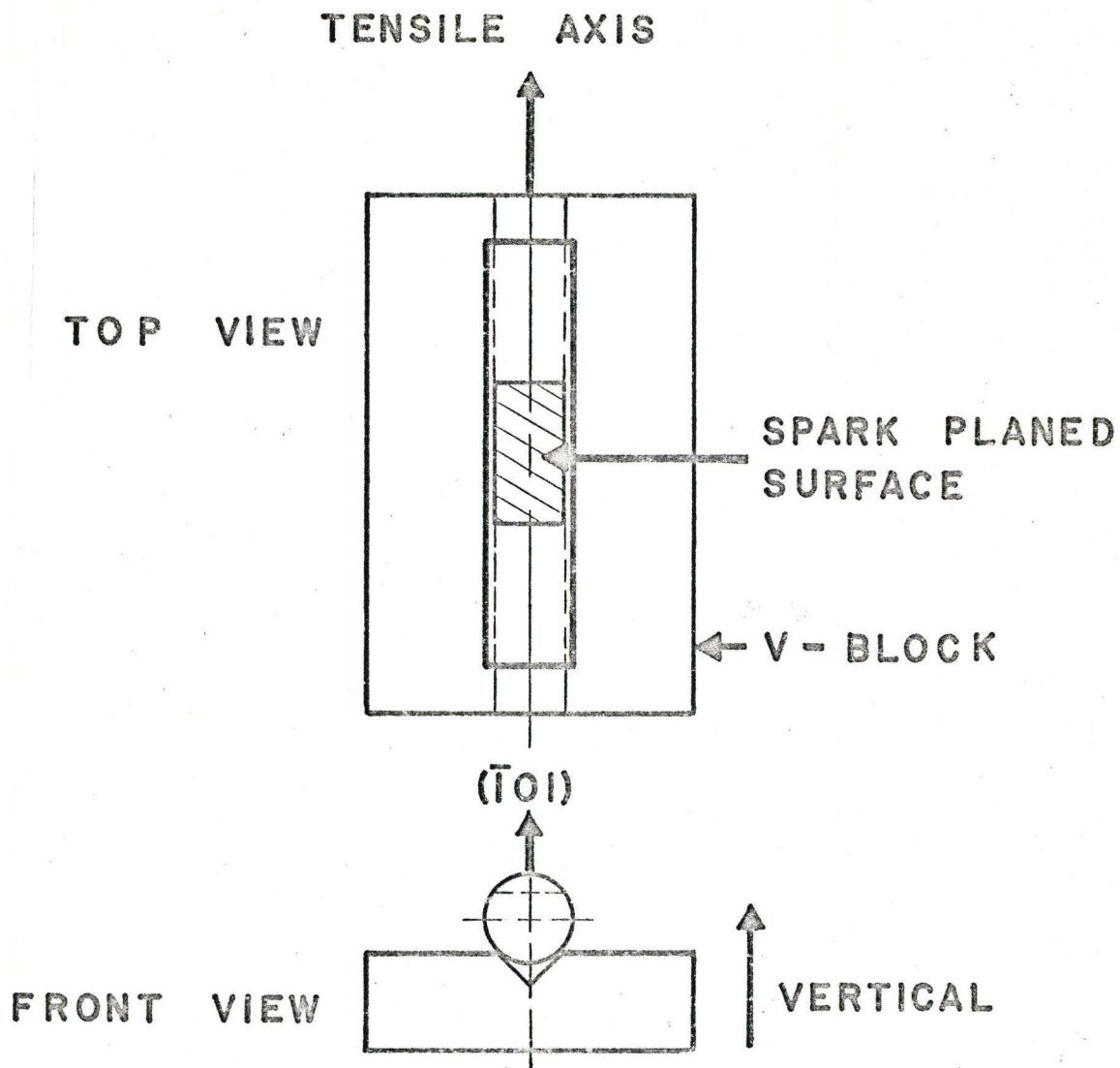


FIGURE 3.1  
VIEW OF SPARK PLANED SURFACE

specimen by the spark planing could be removed. From work reported in the literature (Steeds 1966) the depth of damage for spark planing was about 0.3 mm. As a result, it was felt that absolutely no damage would be visible below a depth of 1 mm. from the planed surface. The chemical polishing used to remove this damage was carefully controlled by swabbing and minimizing agitation around the tensile axis of the specimen so corners would not be preferentially attacked. For the particular orientation of faces chosen, no significant attack at the corners of the square crosssection was noticed in the chemical polish (50% Nitric in water). Some rounding was noticed, however, for the electrolytic polish (methyl-nitric) although this was a very slow attack.

### 3.4 The Fatigue Adaptor

The cyclic straining modification to the Instron TTC-L was designed and constructed by Watt (1967) and a full description of its advantages, specifications and design have been given in Watt's thesis (1967). The most important features of this adaptor for the present work were the open cage design, which allowed simple "in situ" electropolishing and replication of specimens; and also the complete control of the stress applied to the specimen while mounting. The only disadvantage of the jig was that considerable time was required to align the adaptor and the specimens before fatiguing could begin. The complete procedure required for this alignment has been described in Watt's thesis.

### 3.5 Single Crystal Dimensional Measurements

Prior to mounting, each crystal was measured for dimensional

consistency. Optical comparator measurements (courtesy of the Department of Mechanical Engineering) revealed any sharp changes in the parallel nature of the gauge length sides and in the "skew" of the gauge length with respect to the gripping ends. Micrometer measurements taken at 3 points along the gauge length for each pair of faces were averaged and used to calculate crosssectional areas.

### 3.6 Fatigue Cycling

The actual mounting and alignment of the fatigue specimen was described in detail by Watt (1967) and this procedure was followed for these tests. The subsequent cycling was performed at constant plastic strain by monitoring the elongation on the Instron chart recorder.

The elastic curve was extended as shown in Figure 3.2 and the plastic elongation measured off while the crosshead was moving. At the elongation necessary to give the predetermined plastic strain, the crosshead motion was reversed. The "hardness" of the gripping method, the fatigue adaptor and the Instron anti-backlash system meant very little overshoot or backlash was evident on strain reversal. The plastic strain could be measured easily to within an error of  $\pm 5\%$  at the operating beam speeds. Early in the cycling, such accuracy could be increased by reducing the beam speed so the plastic elongation could be more easily measured.

### 3.7 Electropolishing of the Bulk Specimen "in situ"

The design of the fatigue adaptor allowed "in situ" electropolishing of the specimen provided the exposed stainless steel parts

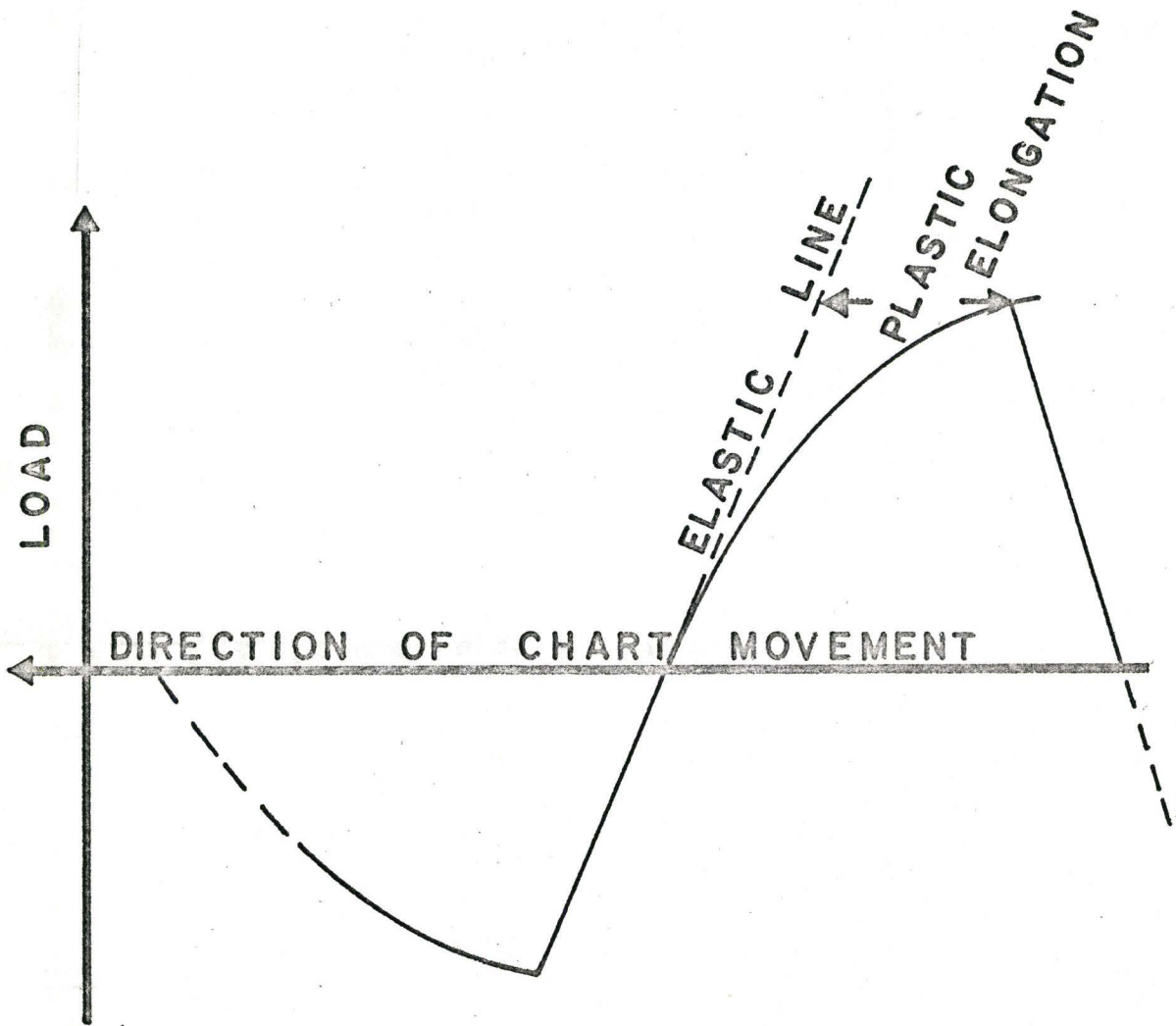


FIGURE - 3.2

METHOD OF DETERMINING  $\gamma_p$  ELONGATION DURING CYCLING.

were carefully protected in a thick layer of Microstop. Initially the electropolishing technique given by Watt (1967) was followed [that is: 6% $H_3PO_4$  in distilled water at  $\sim 0^\circ C$ ]. Polishing with this solution was very inconsistent for some unknown reason, so a 55% (volume) of 85% Orthophosphoric acid in distilled water was substituted. At  $0^\circ C$  and  $\sim 2.5$  volts, this solution appeared to work quite well, although pitting occurred periodically even though the same operating conditions were used.

After each electropolish, the samples and the fatigue adaptor were repeatedly washed in distilled water held at  $5^\circ C$ , then in water at room temperature. This procedure was followed to enable closer control of the strains introduced by the differential coefficients of thermal expansion of the stainless steel fatigue adaptor and the copper sample. (These could put loads of 60 pounds or more on the specimen. The final wash was with an ethanol spray which was dried with a hand-held hair dryer (at room temperature).

### 3.8 Replica Techniques

The slip line behaviour was studied by means of optical replicas taken from the surface at various stages during the cycling. The replicating material was in the form of .005" thick cellulose acetate sheets with matte finish on one side. A piece of acetate was cut to cover one flat of the specimen, with about 1/2" of excess on either side of the gauge length. The centre portion of the shiny side was softened by applying acetone to it from a squeeze bottle. Holding the acetate in one hand, care was taken to prevent the acetone from contacting the matte finish

side. The softened face was pressed immediately against the specimen face. After a few seconds of moderate but steady pressure, the thumb exerting the pressure was carefully taken off the back of the replica and the replica allowed to dry. After a minimum of 20 minutes drying time (30 minutes depending on the ambient temperature and humidity), the replica was carefully peeled off the specimen, cut to size and mounted on a glass microscope slide. The replica was cut to a border just outside the imprinted surface to minimize warping problems of the replica on the slide after the plastic dries completely.

The mounted replicas were examined in a standard metallographic microscope, and if the quality of the replica was sufficiently good, it was "shadowed" with approximately  $100\text{\AA}^0$  of aluminum deposited by vacuum evaporation. The aluminum increased the reflectivity of the replicating surface and also gave the slip lines higher contrast by a shadowing effect (the aluminum was evaporated onto the surface at an angle of  $10^\circ$  to the surface). These replicas were then carefully examined in a Zeiss Ultraphot microscope, and appropriate micrographs were taken.

### 3.9 Electron Microscopy

Sections were cut from the gauge lengths of the fatigued specimens in the spark cutter. From Steeds(1966) and other investigators, the depth of damage from spark cutting methods was approximately 0.3 mm. Sections were therefore cut 1.0 mm. Subsequent chemical and electrolytic polishing presumably removed all traces of the spark erosion damage from both faces.

These sections were thinned initially in a 50% (volume) solution of nitric acid in water. It was found that dropping the sample into the

beaker of acid and allowing it to sit on the bottom as it was chemically attacked resulted in an unsatisfactory, uneven surface. The best method was found to be suspension from a pair of tweezers suitably protected by Microstop. A rapid stirring rate from a magnetic mixer, combined with occasional 180° rotations of the specimen in the tweezers resulted in very even chemical thinning over the whole surface area.

As the sample became progressively thinner, the edges moved in noticeably. At this point, the sample was alternately dipped into the nitric solution and taken out, with the most of the time spent out of solution. The meniscus formed by the nitric acid on the surface when the sample was out of the nitric acid resulted in increased attack near the centre of the specimen and very little attack at the edges.

At the initial sign of perforation during the chemical thinning, the sample was lacquered off at the edges with microstop, supported by the tweezers and electropolished in a solution of 67% methanol, 33% nitric (volume) at a temperature of -20°C to -35°C. Alternate short periods of chemical and electrolytic polishing resulted in a generally smooth, rapid attack over the whole surface. The standard "window" technique was then followed for the final stages of thinning and at least thirty seconds of electropolishing was necessary just prior to cutting and mounting the thin foil in order to obtain a good surface on the specimen.

An alternative to the 50% nitric solution is one consisting of (1/3 nitric, 1/3 acetic, 1/3 phosphoric by volume), stirred at about 55 to 60°C. This chemical polish produces a smooth, bright finish provided the solution is fresh. However, edge attack was extremely rapid and considerable care was necessary in its use.

This technique was repeatedly successful for sample measuring 6 mm. x 6 mm. in crosssection, but was less successful for samples smaller than that.

The final thin foils were examined in a Siemens Elmiskop I electron microscope at 100 kV. A double tilt specimen stage and cartridge were used. A number of quantitative Burgers vector analyses were carried out to determine the types of dislocation present. In addition, low magnification pictures were taken wherever possible to obtain a more general idea of the overall configuration of dislocations.

These electron microscope observations were carried out on specimens cut parallel to (111) primary slip planes and also cut parallel to the  $(\bar{1}01)$  plane in which the primary slip direction emerges normal to the foil surface (see Figure 3.3).

Some electron microscope replica work has been done on the Phillips EM300 and also on the Siemens operating at 60kV in order to study the fine slip lines and their distribution on some specimens. The most successful replica technique was the single stage carbon-platinum replicas removed from the specimen by exposure to nitric acid vapour for 2 minutes followed by immersion in a 2% ethylenediamine solution and finally slow immersion in distilled water to lift the replica off. The small pieces of replica were collected from the surface of the water on 200 mesh grids.

### 3.10 Outline of Experimental Procedure

Utilizing the techniques as described previously, the experimental programme ran as follows. The single crystal was grown from the

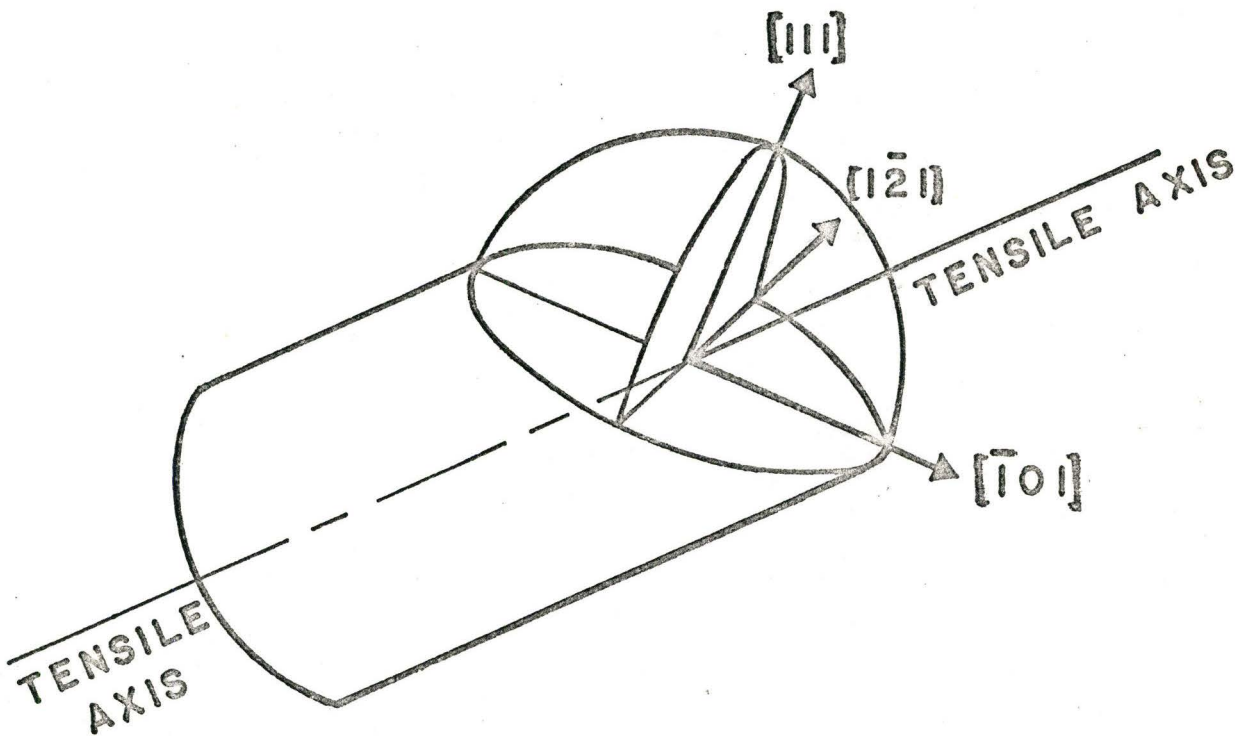


FIGURE-3.3

DIAGRAM OF TWO SECTIONS CUT —  
FROM A CRYSTAL.

high purity copper in a 12.5 inch length. This was checked for perfection by etching and x-ray work and upon confirming that it was a single crystal, it was annealed at 950°C for 24 hours. The crystal was then spark cut into 2.5 inch lengths and the square cross-section gauge lengths machined into each piece. These spark planed surfaces were chemically and electrolytically polished to a depth of 1 mm. each.

The fatigue adaptor was installed in the Instron testing machine and aligned in the manner outlined by Watt (1967). The sample was mounted in the adaptor (again according to Watt (1967)) and the sample electro-polished after mounting. The crystals were then cycled to 2,5,21,50 and 100 cycles at a constant plastic strain amplitude of  $\pm .0025$  (low amplitude). The surface slip marking were studied by means of replicas for the optical microscope. Some electron microscope replicas were taken after demounting the specimen.

Each specimen was de-mounted and then oriented by Laue x-rays for cutting in the spark cutter. The initial sections were cut parallel to the (111) planes and subsequently parallel to the  $(\bar{1}01)$  planes (for 5 and 50 cycles).

These sections were thinned chemically and electrolytically by a modified window technique to produce thin films suitable for viewing in the electron microscope. Each section was studied in the Siemens Elmiskop I at 100 kV. Various tilting experiments were performed in the microscope to obtain optimum contrast and to study Burgers vectors.

## CHAPTER 4

### EXPERIMENTAL RESULTS

#### 4.1 Introduction

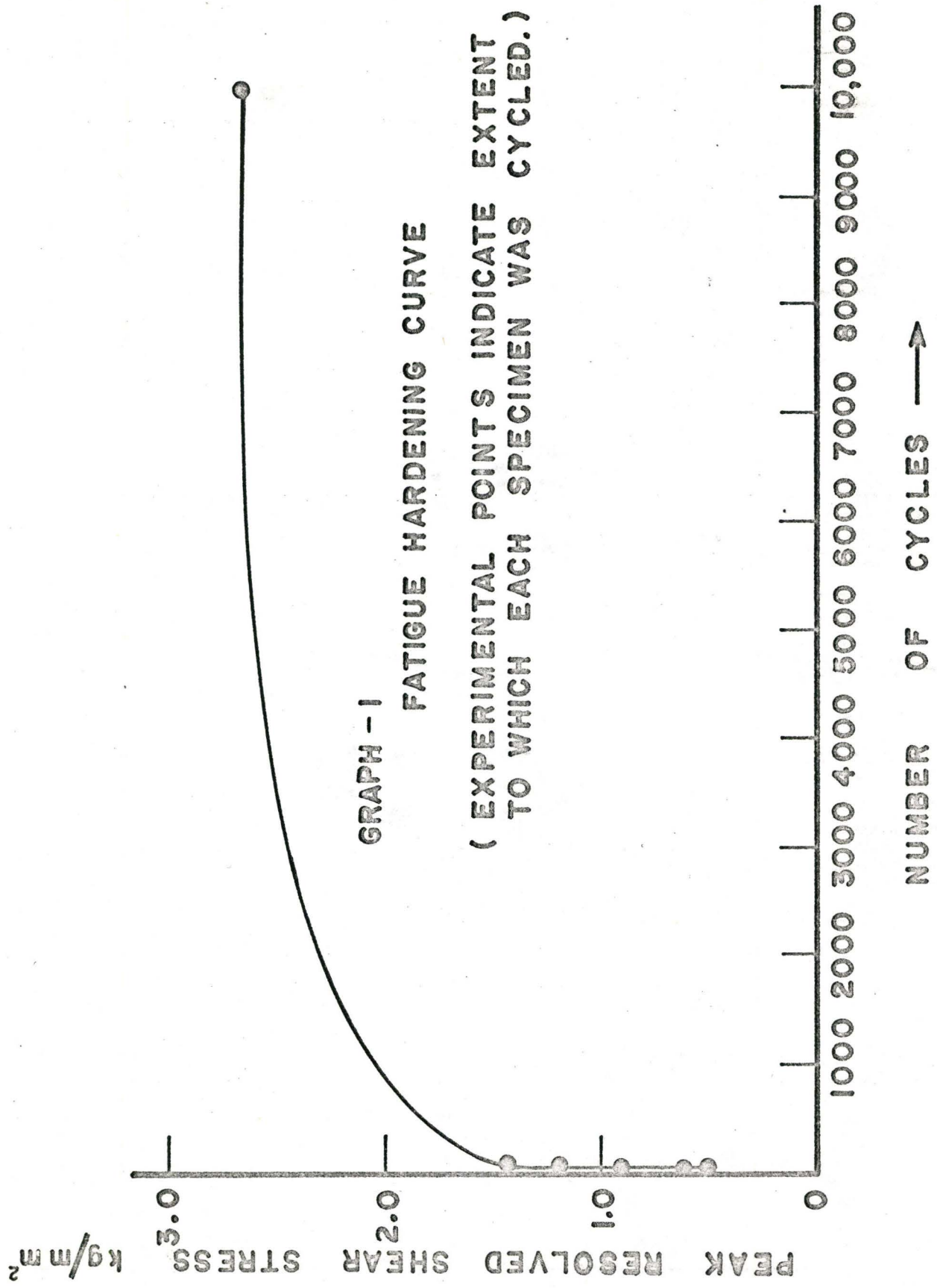
The larger part of the experimental results were micrographs of the dislocation distribution at various stages in the hardening. These are divided into two major sections to facilitate their examination. The first set of micrographs deals with the geometry and overall density of dislocations as a function of cumulative strain. Both (111) and ( $\bar{1}01$ ) sections have been utilized to show a three dimensional picture of the arrangements. The ( $\bar{1}01$ ) section has been chosen because the primary dislocations can be easily tilted out of contrast to show the density of secondary dislocations.

The second set of micrographs show some Burgers vector (Appendix 2) analyses at the 2,5, 21 and 50 cycle stages. These showed relative densities of various dislocations (primary and secondary) and some particular dislocation interactions of interest.

Each section (that is (111) or ( $\bar{1}01$ ) at each stage) is represented by only one or two micrographs. These were selected from a large number of micrographs (numbering about 100 or so for each section).

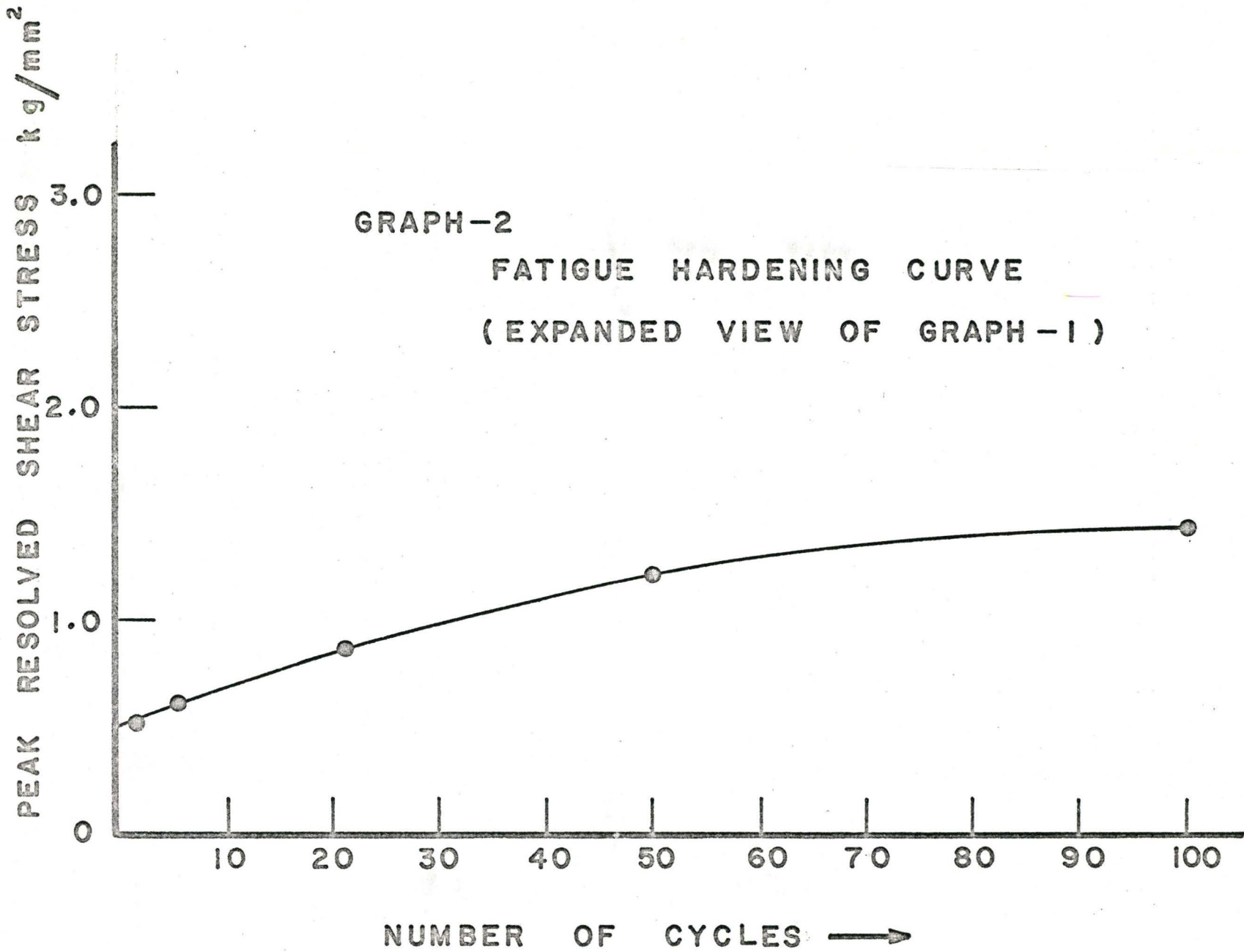
The slip line observations were included at the end to indicate the relation between the obstacle spacing and the slip lines.





PEAK RESOLVED SHEAR STRESS kg/mm<sup>2</sup>

NUMBER OF CYCLES →



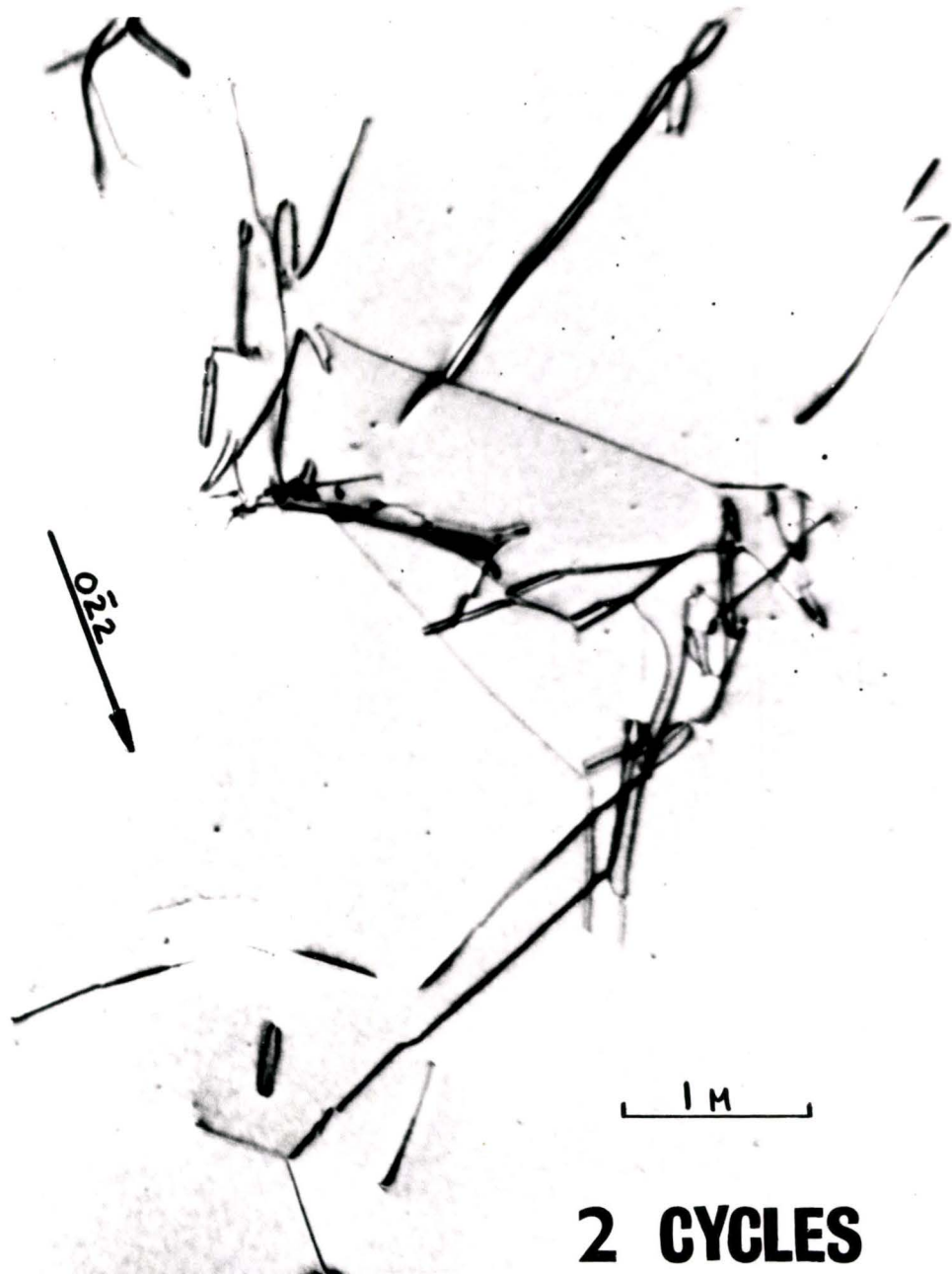
## 4.2 Experimental Results: Part I Geometry and Density of Dislocations

### 4.2.1 Electron Micrograph #1

Strain: 2 cycles

Foil Normal: [11]

This photograph shows the dislocation microstructure at 2 cycles. It should be noted that areas such as these are isolated in an otherwise dislocation free matrix. Careful examination of this micrograph reveals a number of interesting geometries in the dislocations which indicate that some very complicated interactions are occurring. However if these complex configurations are ignored, and only the long straight lengths of dislocations considered, then one can draw some conclusions in the following manner. The thin foil was cut parallel to the primary slip plane and therefore it is reasonable to assume that the long, straight lengths of dislocations seen in this micrograph are lying in the primary slip plane. (If one assumes a foil  $1000 - 2000\text{\AA}$  thick, which is in the right range, then a dislocation 3 or 4 microns long must lie at a small angle to the foil). It is probable that these dislocations also have their Burgers vector lying in the primary slip plane and in fact along  $[\bar{1}01]$  or  $[1\bar{1}0]$ , the two most highly stressed close-packed directions in the crystal.



**2 CYCLES**

#### 4.2.2 Electron Micrograph #2

Strain: 5 cycles

Foil Normal: [111]

The 5 cycle sample showed some areas such as this shown in micrograph 2, but the larger part of the crystal was much less densely packed by dislocations. There is a hint of the "braid" structure as seen in the (111) sections later in the hardening but relatively large areas of dislocation-free matrix still separate them.

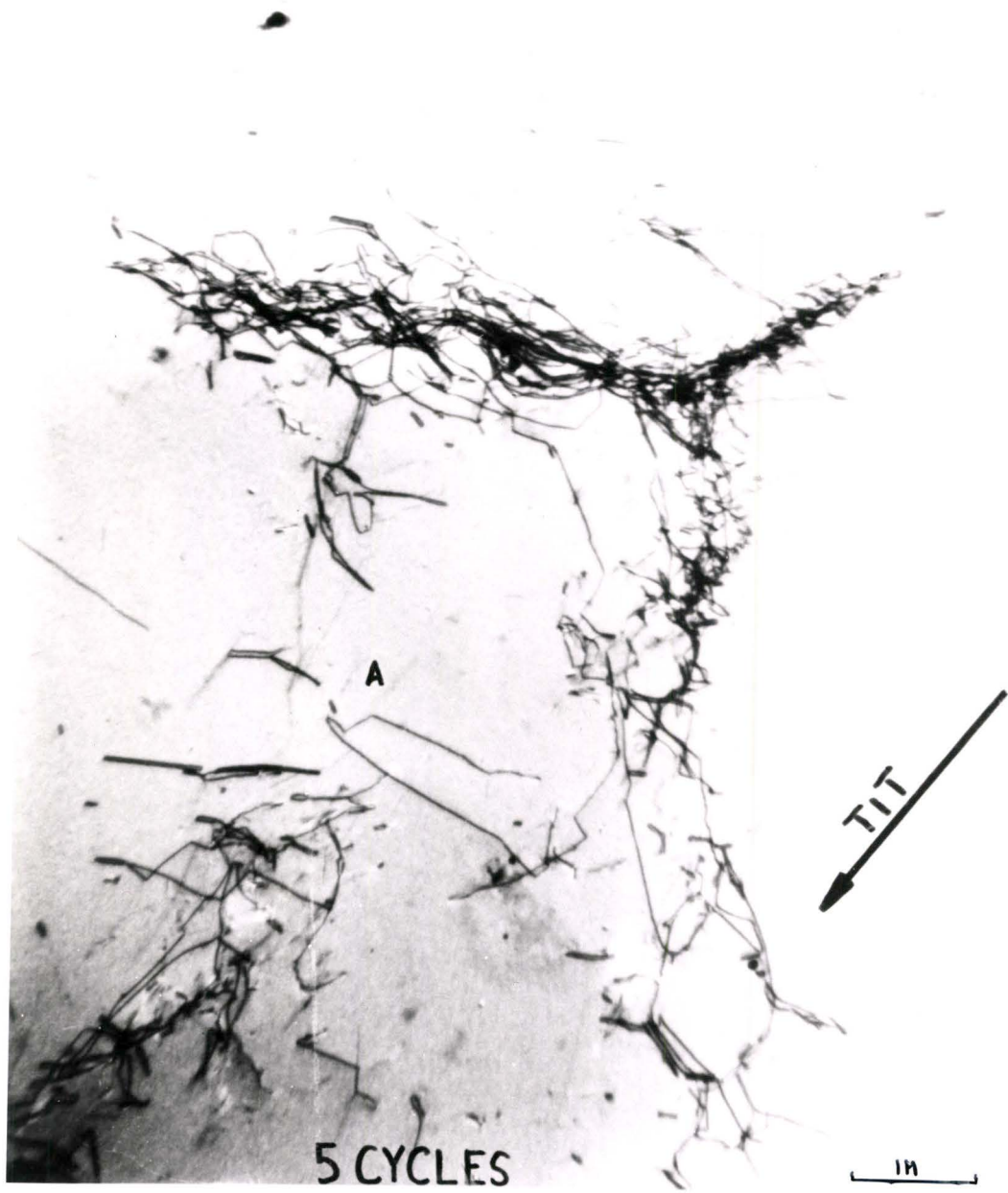
When compared to micrograph #1 (at 2 cycles), the density of dislocations is considerably greater in these elementary braids than in any areas at 2 cycles. However it is significant to notice that individual dislocations are still resolvable even within the braids and that the boundaries of the braids are ill-defined and ragged in appearance. Faint residual images (due to the edge nature) of dipoles can be seen at point A in the micrograph. This can be verified by examination of a companion photograph of this same area under a different operating reflection.

The majority of these dislocations are either  $\frac{a}{2} [\bar{1}01]$  primaries or  $\frac{a}{2} [1\bar{1}0]$  coplanars, with some undetermined secondaries also present. This predominance of primary plane dislocations is strikingly evident in a later micrograph of a thin foil perpendicular to this section.

On a larger scale, there is no noticeable single preferred orientation for the braids, although three distinct traces, along the critical and conjugate traces and along the primary slip direction were seen, often in a "Y" configuration. There are some braids also aligned

along  $[\bar{1}21]$ , the primary edge dislocation orientation. So it is not clear at this stage if the braids will eventually build up preferentially along any one direction.

Particular attention should be paid to the fact that the dipoles are still quite long and the tangles not very dense.



A

TIT

5 CYCLES

1μ

### 4.2.3 Micrograph #3

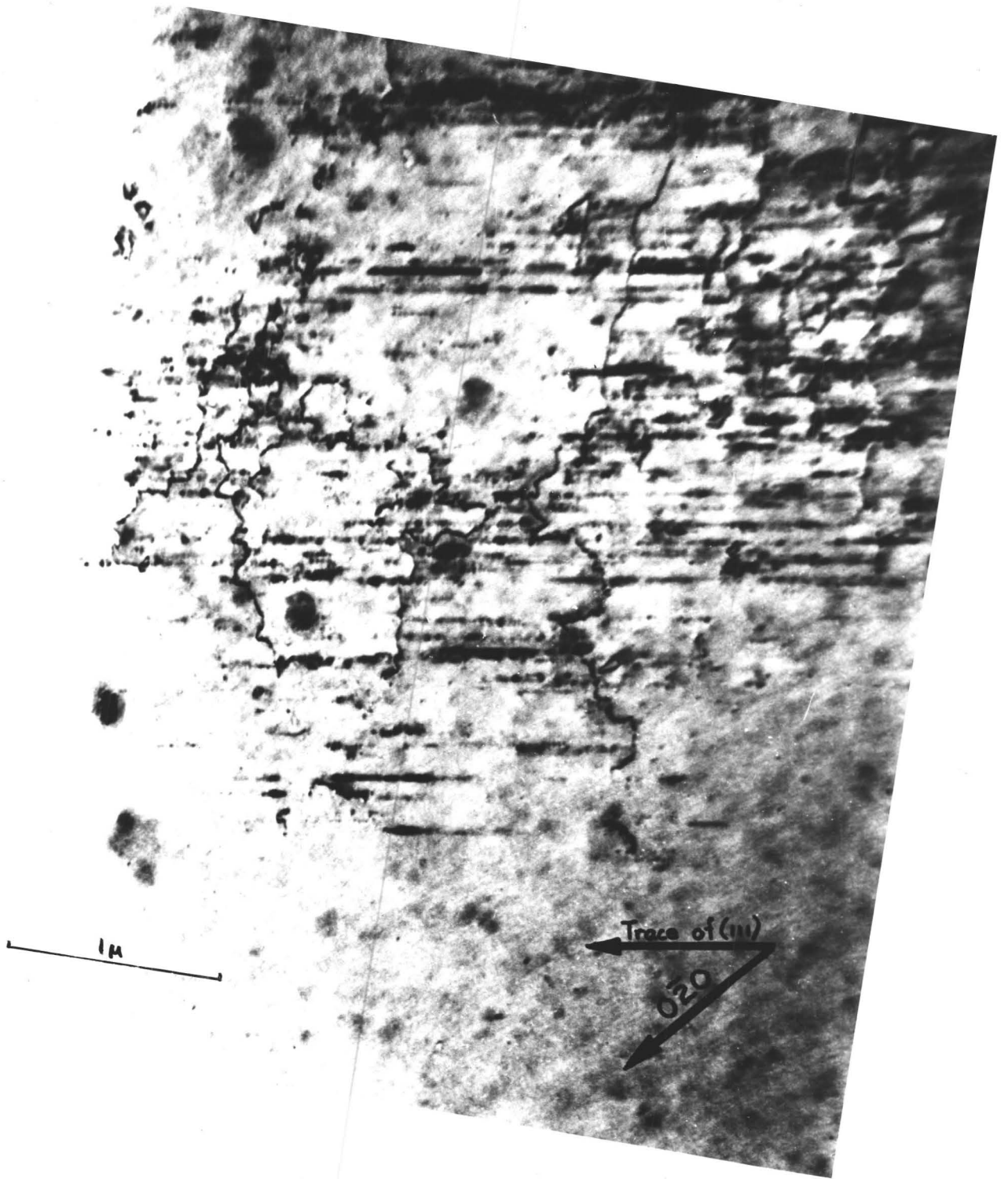
Strain: 5 cycles

Foil Normal:  $[\bar{1}01]$

This area in a  $(\bar{1}01)$  section shows a large patch of dipoles lying in the primary plane (elongated faint images along the trace of the primary plane) associated with a number of long lengths of twisted, heavily jogged forest dislocations.

Under the  $[0\bar{2}0]$  operating reflection, the primary dislocations are out of contrast while the coplanar (next most highly stressed) dislocations are in contrast. This latter type accounts for the dipoles which are in contrast along the trace of the primary plane.

Both micrograph #9 and #3 show that the forest dislocations appear to be involved in the blocking of slip from very early in hardening (5 cycles). Micrograph #3 shows that there are some large patches of dipoles and dislocation lying in the  $(\bar{1}01)$  plane. This may be compared with the observation in micrograph #2 that braids were seen to lie along  $[\bar{1}2\bar{1}]$  directions in some cases. However, in both foils, the braids lying along  $[\bar{1}2\bar{1}]$  in the  $(111)$  section and large patches in the  $(\bar{1}01)$  sections were quite rare. In the  $(\bar{1}01)$  section, the smaller dipole patches of the order of size of that seen in micrograph #9 were much more common. These smaller patches apparently are the end-on views of elementary braids which lies along  $[\bar{1}01]$ , or  $[\bar{1}\bar{1}0]$  or  $[0\bar{1}\bar{1}]$  in the primary plane. The braids therefore may be described as patches which are extended in planes perpendicular to the primary plane. The traces of these patches in the primary plane are along the close-packed  $\langle 110 \rangle$  directions and along the primary edge direction  $[\bar{1}2\bar{1}]$ .



#### 4.2.4 Electron Micrograph #4

Strain: 21 cycles

Foil Normal: [111]

This typical area at 21 cycles shows an arrangement which looks similar to that seen at 5 cycles. The internal structure of this braid is not much different from the earlier braids. However examination of a large area of the thin foil indicated that the microstructure is much more uniform at 21 cycles than at 5 cycles. That is, the braids are much more numerous and closer together than at 5 cycles. Particular regions (such as that seen in electron micrograph #15) at 21 cycles show braid configurations which are much more dense and complex in their internal structure. In addition, there appears to be finer debris present near these braids at 21 cycles and many of the dipoles are visible only as small "specks" on the micrograph.

It is apparent that the "Y" configuration seen here and at 5 cycles is a very common arrangement in the early stages of hardening. The three-fold symmetry of the arrangement is fairly general and no particularly preferred orientation is yet seen in the overall geometry.



#### 4.2.5 Electron Micrograph #5 and Electron Micrograph #6

Strain: 50 cycles

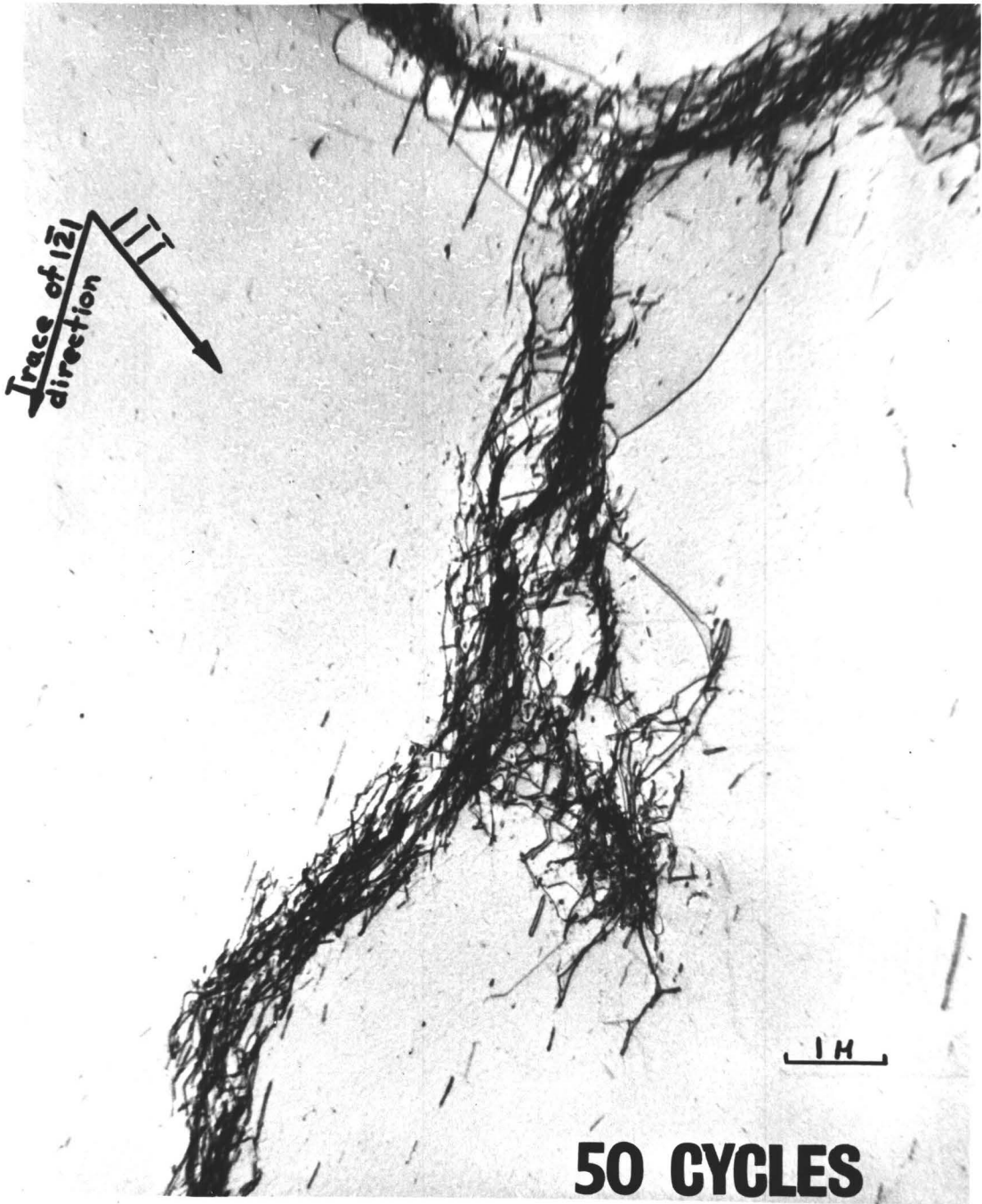
Foil Normal:  $[\bar{1}\bar{1}\bar{1}]$

This area is representative of the 50 cycle specimen. The braids are now much more highly developed, they are denser, with very short dipoles within them, and on a general scale, they are beginning to show a definite basis for a "cellular" structure of some sort. (These "cells" refer to a 2-dimensional cellular arrangement in the primary slip plane -- the generation of a 3-dimensional structure is discussed later in conjunction with the  $(\bar{1}01)$  sections.

This particular micrograph shows the primary dipole loops oriented along the major portion of the braid lying along  $[01\bar{1}]$ , the trace of the critical plane. The upper and lower "arms" of the braid lie approximately along  $[\bar{1}\bar{1}0]$  and  $[\bar{1}01]$ , similar to the 3-fold orientations seen earlier.

In addition to this micrograph at 50 cycles, a low magnification composite was also possible and is shown in the next electron micrograph #6. This shows the overall geometry of the braids at 50 cycles. As can be seen, there is no well defined preferred orientation to the structure as yet. Unfortunately, no diffraction pattern is available with this composite to show the directions. However, if the dipoles are assumed to be predominantly  $\frac{a}{2}[\bar{1}01]$  and  $\frac{a}{2}[\bar{1}\bar{1}0]$ , then the vertical direction is approximately  $[02\bar{2}]$ , or the trace of the critical plane.

Earlier thin foils (21 cycles, 5 cycles) do not show this sort of continuity of the braids through the matrix but show more or less isolated braids of various orientations.





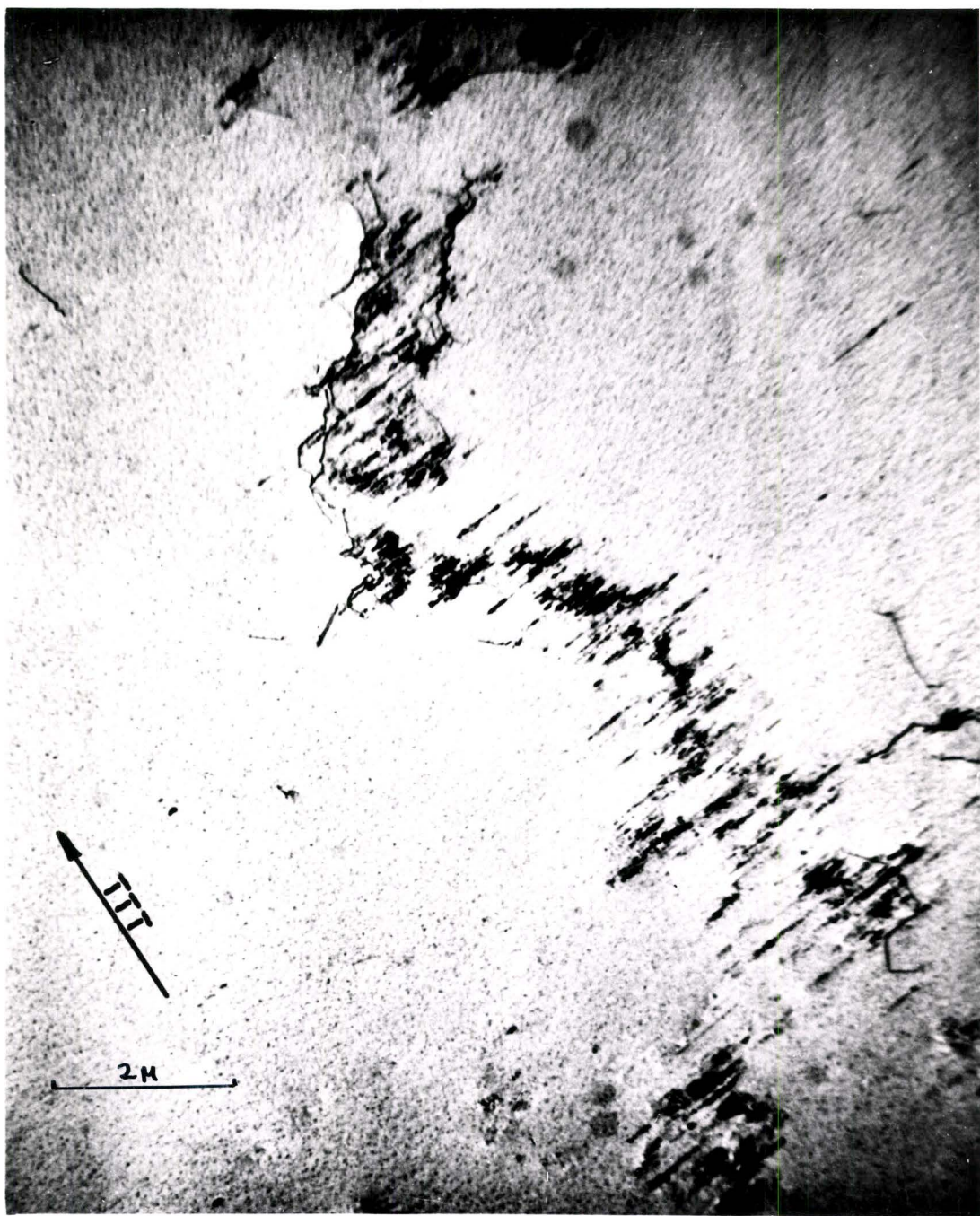
#### 4.2.6 Micrograph #7 and Micrograph #8

Strain: 50 cycles

Foil Normal:  $[\bar{1}01]$

The  $(\bar{1}01)$  section at 50 cycles shows a generally more highly developed structure. The areas of densely packed dislocations are now more numerous than those seen at 5 cycles in the  $(\bar{1}01)$  plane. In addition, the tangles appear to be denser in localized regions in the braids. The trace of the primary plane is still easily visible in the faint residual images of the primary plane dipoles. Under the operating reflection  $[\bar{1}\bar{1}\bar{1}]$  for both micrographs, the primary and coplanar dislocations are both out of contrast and should show faint images. There are apparently a great many non-coplanar dislocations which are in good contrast and which are localized in the denser patches mentioned above. These dislocations are apparently very short and too densely packed to resolve individually. The long forest dislocations which were noted at 5 cycles are still visible and their density has not increased noticeably.





#### 4.2.7 Electron Micrograph #9

Strain: 100 cycles

Foil Normal: [111]

The 100 cycle specimen shows a ragged elongated cellular arrangement of braids lying in the primary plane. The debris (fine dipole loops) are now resolvable only as fine specks in and near the tangles. The braids are preferentially oriented along the  $[01\bar{1}]$  direction, which is the trace of the critical plane. This will later be shown to be indicative of more slip activity on the critical plane than on any other secondary plane.



#### 4.2.8 Micrograph #10 and Micrograph #11

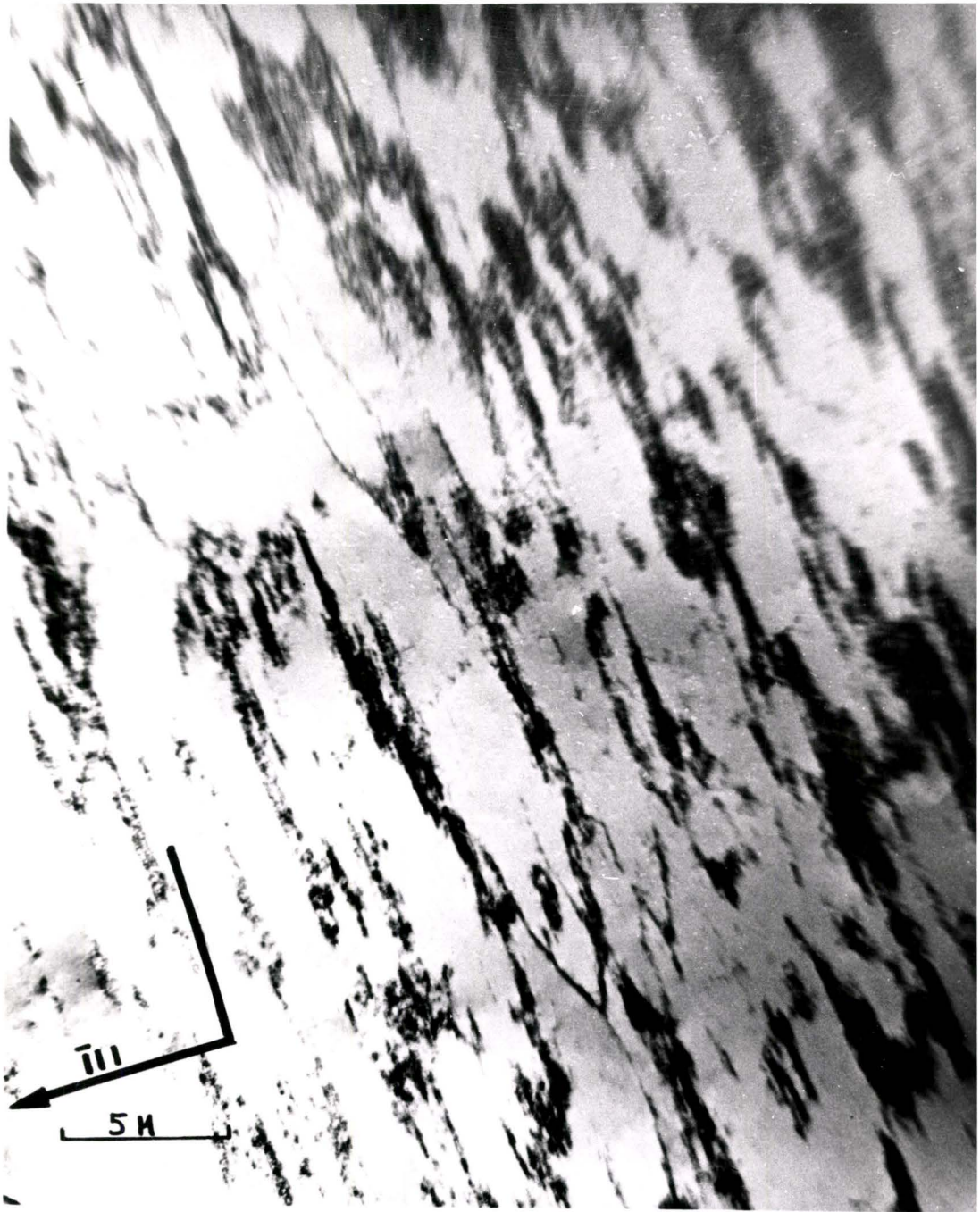
Strain:  $\sim 10,000$  cycles (saturated state)

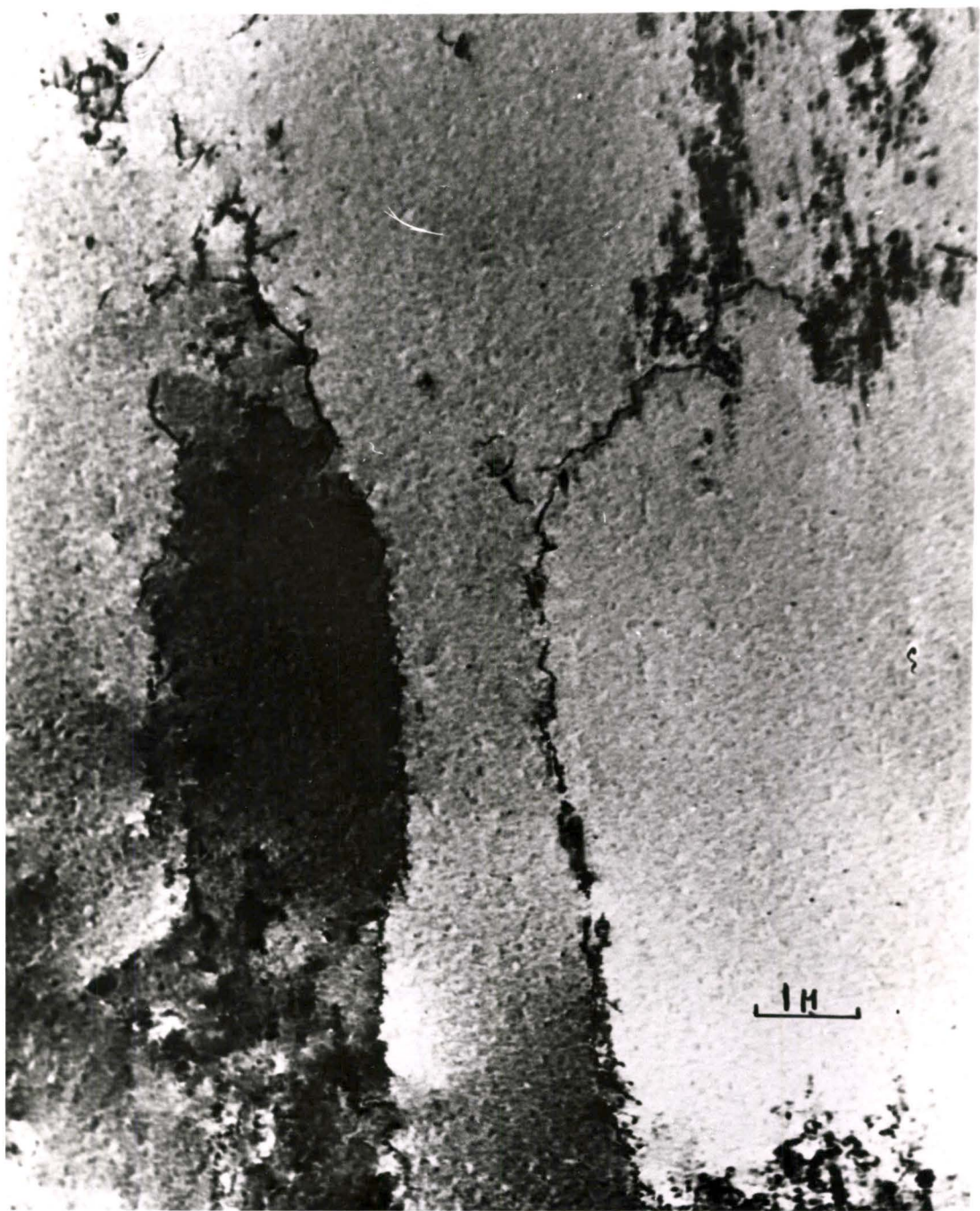
Foil Normal:  $[111]$

This structure, as seen at 10,000 cycles, is believed to be representative of the overall dislocation distribution at the saturated state. It is not clear whether this representative structure breaks down into some other configuration at isolated regions in the crystal where some sort of microstructural instability arises, ie. persistent slip bands, or some other process is responsible for the surface topology at saturation. This is a problem requiring a considerable amount of electron microscopy on the saturated state crystal.

The preferred orientation for the braids is along the trace of the critical plane  $[01\bar{1}]$ . Under the given operating reflection, the primary and coplanar dislocations are in contrast and the secondary dislocations  $[110]$ ,  $[101]$  are out of contrast.

The micrograph #11 is a higher magnification of an area from the same foil as #10. It shows a commonly seen type of cell seen at saturation in which there is a misorientation across the wall (as indicated by the change in contrast from one side of the wall to the other).





### 4.3 Summary of Part I: Geometry and Density of Dislocations in Fatigue Hardening

The results in Part I have shown that the overall arrangement of dislocations becomes more uniform as the hardening progresses. At the same time, the density of dislocations in the crystal increases.

The initial barriers to slip in the first few cycles of hardening appear to be the forest dislocations which pierce the primary plane and dislocations and dipoles are arranged in the immediate neighbourhood of forest dislocations at 5 cycles. Up to 21 cycles, the geometry of braids which are so initiated remains virtually the same. The braids are aligned along  $\langle 110 \rangle$  directions in the primary plane and along  $[\bar{1}\bar{2}1]$ . They are often seen in a "Y" configuration at 5 and 21 cycles.

Although the geometry is similar, the density of dislocations is increasing from 5 to 21 cycles as the braids become more evenly distributed and closer together towards 21 cycles. The density of dislocations within the braids is also increasing slightly from 5 to 21 cycles.

At 50 cycles, the braids have become very dense, with very fine dipole debris packed tightly together with dislocations in the braids. The braids have also become more uniformly distributed and show long, continuous lengths. No specific orientation direction for the braids is seen at 50 cycles.

At 100 cycles, the density of braids and dislocations within braids has increased noticeably. The braids are preferentially aligned along the  $[0\bar{1}\bar{1}]$  direction, the trace of the critical plane. A ragged,

elongated cellular structure is seen which is uniform across the crystal.

From 100 cycles to saturation, the scale of this cellular structure does not change although the dislocation dipoles within the braids become much finer and the density of dislocations within the braids increases.

In summary, the principal element in the dislocation substructure after 5 cycles appears to be the dislocation dipole lying in the primary plane. The dislocation dipoles become finer with cycling and eventually become fine "specks" in the microstructure. The geometry of the braids around forest dislocations suggests that the forest dislocations are important to early hardening. And finally, the braids become more aligned along a single direction later in hardening (after 50 cycles.)

#### 4.4 Experimental Results - Part II - Burgers Vector Pairs

##### 4.4.1 Micrograph #12

Strain: 2 cycles

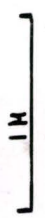
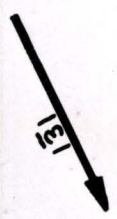
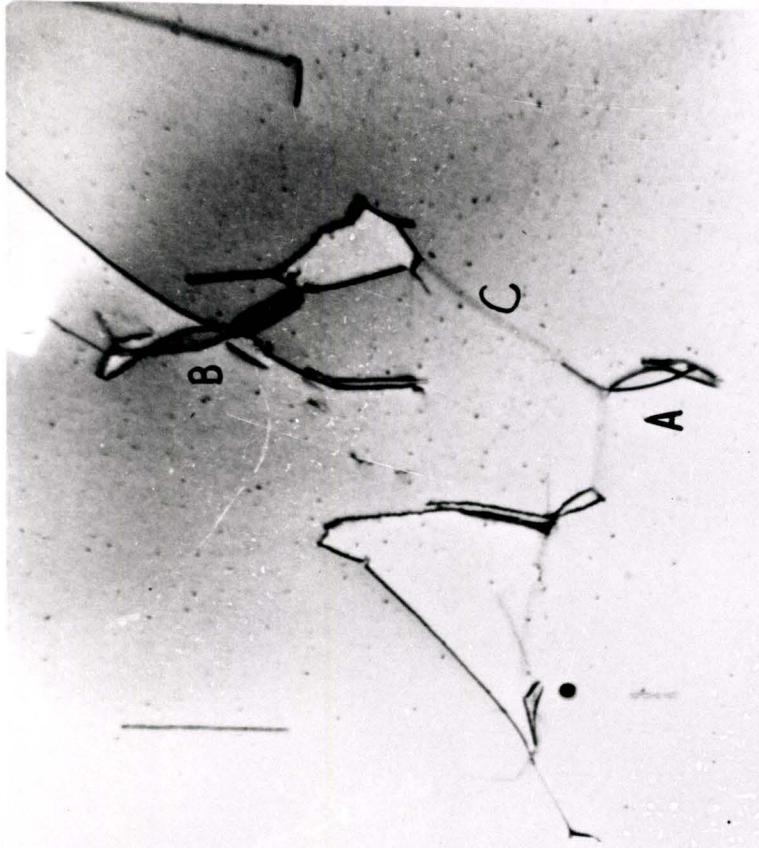
Foil Normal: [111]

This pair of photographs shows an area which is comparable to micrograph #1 (also at 2 cycles). If one looks carefully at the "loop" configuration at the point labelled "A" there is apparently a very complex interaction occurring. And again, at "B", if one compares the 2 micrographs and the changing contrast along the continuous dislocation lines, one can see some sort of interaction which is rather difficult to interpret even on a geometric basis. Such reactions are quite common throughout the foil at 2 cycles, but until further careful study is made on a number of other micrographs, it would be mere speculation to suggest an interaction which would account for these arrangements.

The dislocation at the point labelled "C" (out of contrast in the second micrograph, is in fact a coplanar dislocation  $\frac{a}{2} [\bar{1}\bar{1}0]$  (next most highly stressed).

The other long dislocations are the primary  $\frac{a}{2} [\bar{1}01]$ , of mainly edge orientation.

The conclusion must be that the coplanar  $\frac{a}{2} [\bar{1}\bar{1}0]$  system is very active, perhaps almost as much as the primary system, since it is operative as early as 2 cycles, when few stress raising obstacles are visible. These coplanar dislocations are also quite long and not necessarily associated closely with other dislocations (which may act as stress raising obstacles.).



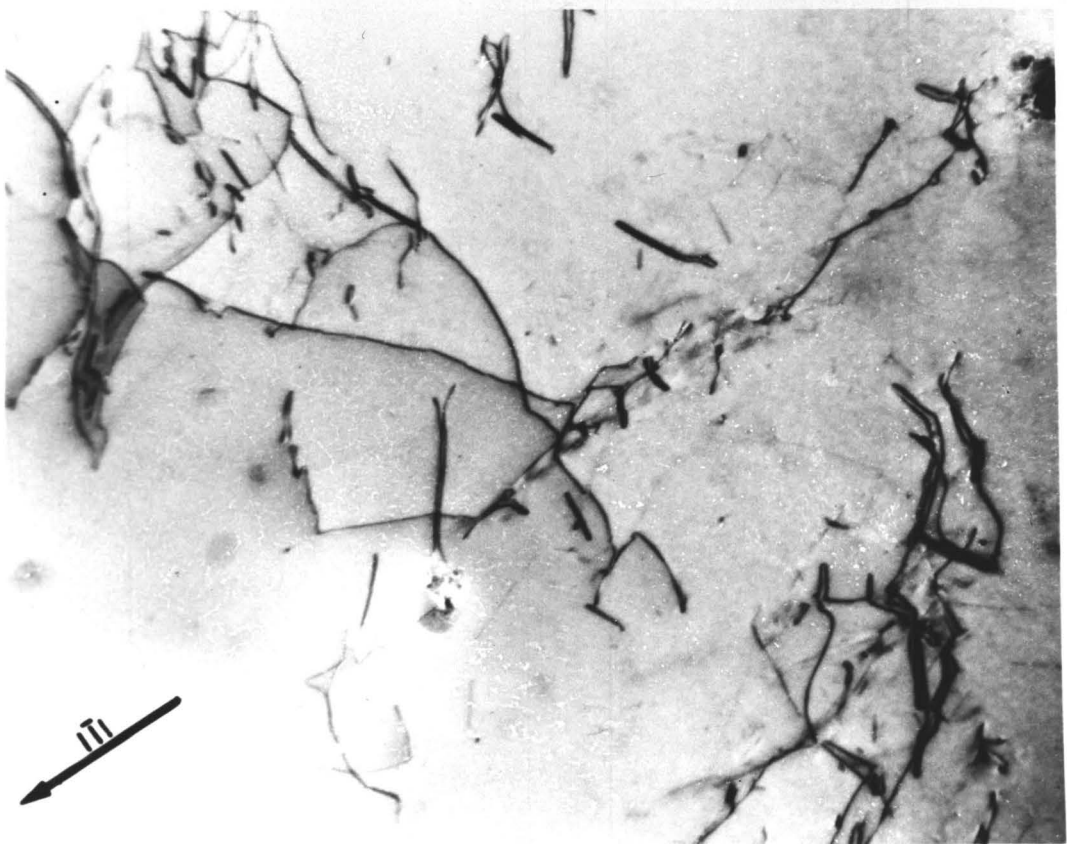
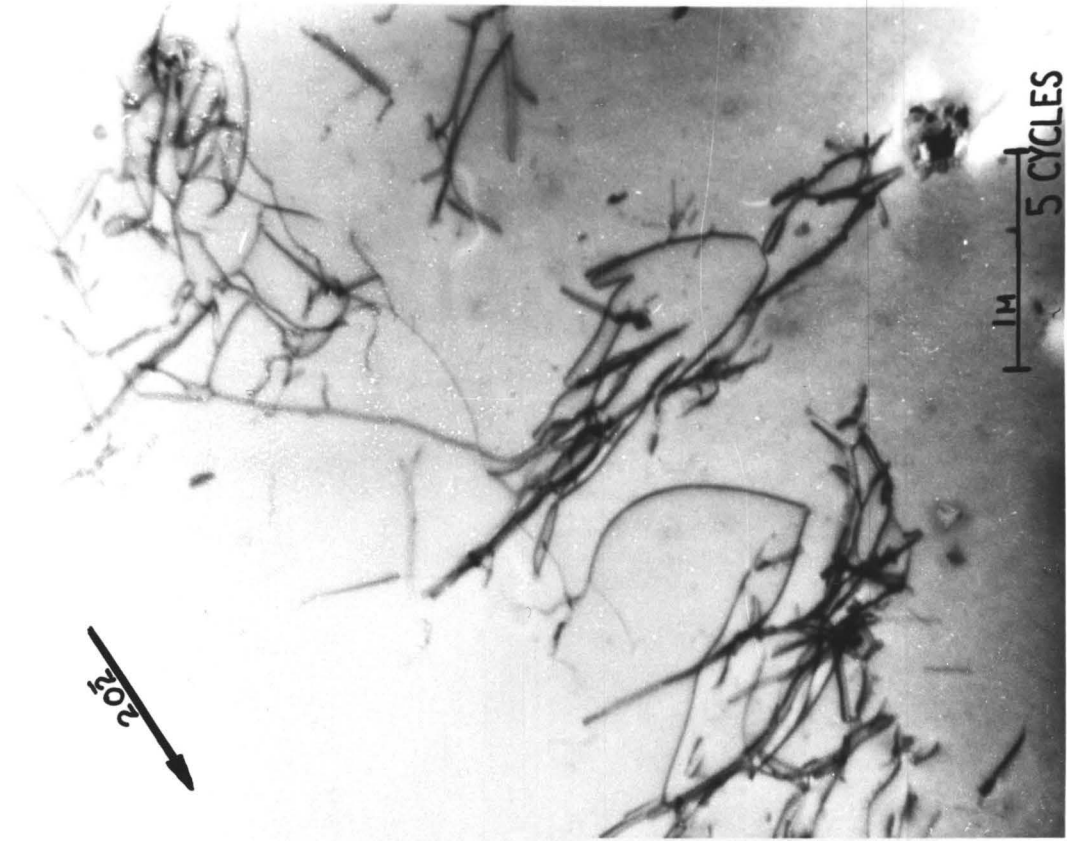
#### 4.4.2 Micrograph #13

Strain: 5 cycles

Foil Normal:  $[111]$

This Burgers vector pair shows the relative densities of the primary  $\frac{a}{2} [\bar{1}01]$  and the coplanar  $\frac{a}{2} [1\bar{1}0]$ . Under the first operating reflection  $[1\bar{1}1]$ , the primary dislocations are out of contrast. Comparison with the second micrograph shows the  $\frac{a}{2} [\bar{1}01]$  dislocations to be of mainly edge orientation. Considering the dislocations in contrast under  $g = 1\bar{1}1$ , it is expected that the longer lengths of dislocations lie in the plane of the foil, or close to the primary plane  $(111)$ . In addition, if one supposes that the next most highly stressed system, the coplanar  $[1\bar{1}0]$  (Schmid factor .423) is much more likely to generate dislocations than the other coplanar  $[01\bar{1}]$  (Schmid factor .037), then most of the remaining dislocations should be  $\frac{a}{2} [1\bar{1}0]$ . If this reasoning is valid, then it may be concluded that the coplanar  $\frac{a}{2} [1\bar{1}0]$  dislocations generally lie along  $[\bar{1}\bar{1}2]$  (edge orientation).

The complex dislocation interactions mentioned in connection with the previous micrograph (at 2 cycles) are again seen at 5 cycles. It appears that many of the complicated configurations are due to the interactions of primary and coplanar dislocations which, as mentioned above, are mainly edge type.



## 4.5 Electron Micrographs of Sections Cut Parallel to $(\bar{1}01)$ Planes

### 4.5.1 Micrograph #14 - Burgers Vector Analysis

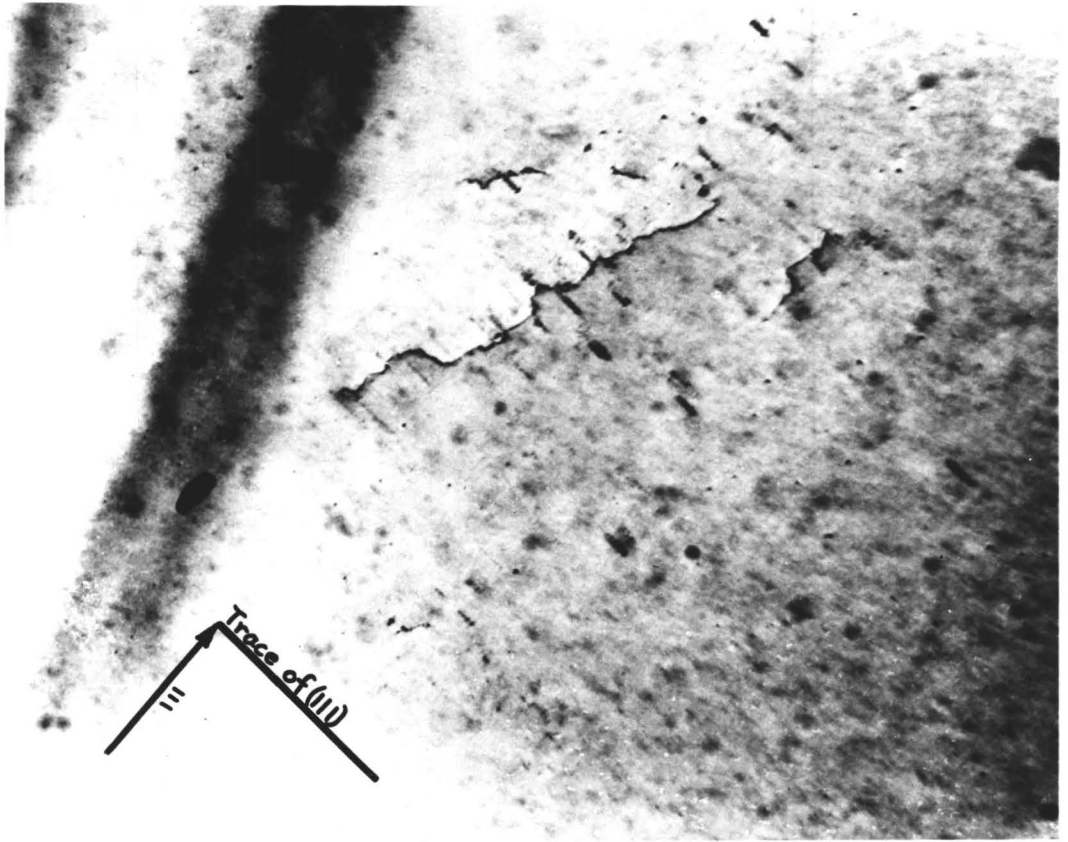
Strain: 5 cycles

Foil Normal:  $[\bar{1}01]$

This pair of micrographs shows an example of arrangement of dipole and forest dislocations at 5 cycles. The dipoles and dislocations of the primary plane are generally associated with a forest dislocation of some kind.

Under the first operating reflection  $g_1 = 111$ , the forest dislocation is in clear contrast: it can be seen threading the primary planes (111). In the immediate vicinity of this forest dislocation, the dipoles lying in the primary plane (along the trace of (111)) can be seen in faint contrast. These are the  $\frac{a}{2} [\bar{1}01]$  type dipoles which, because of their edge nature, show a faint residual image (as explained in any theoretical explanation of Burgers vectors).

Under the second operating reflection  $g_2 = [\bar{1}\bar{1}\bar{1}]$ , the forest dislocation disappears. The only dislocations which appear in  $[111]$  and disappear in  $[\bar{1}\bar{1}\bar{1}]$  are the forest dislocations  $\frac{a}{2} [110]$  and  $\frac{a}{2} [011]$ . The trace of both types of dislocations, whether screw or edge type, would both lie along the direction of the forest seen here. One may therefore say that the forest dislocation is of Burgers vector  $\frac{a}{2} [110]$  or  $\frac{a}{2} [011]$  and is of mainly screw orientation, since if it were in edge orientation, it would lie at a steep angle to the foil and would not show such a long length.



#### 4.5.2 Micrograph #15

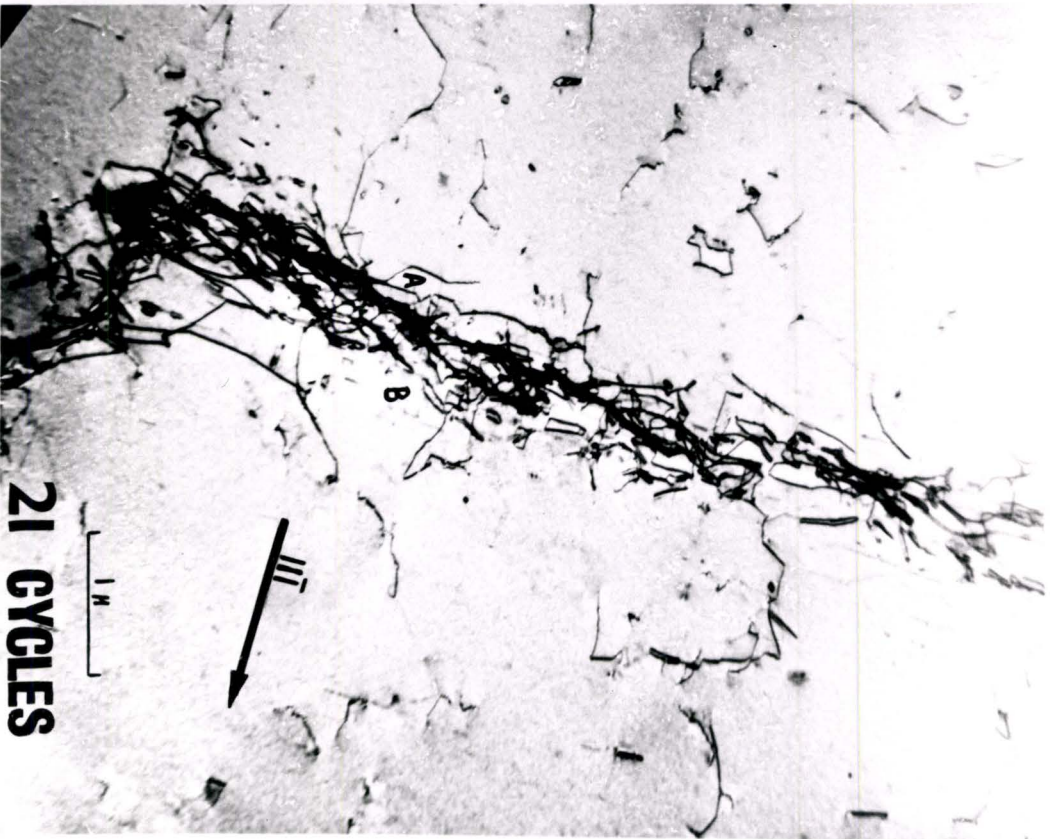
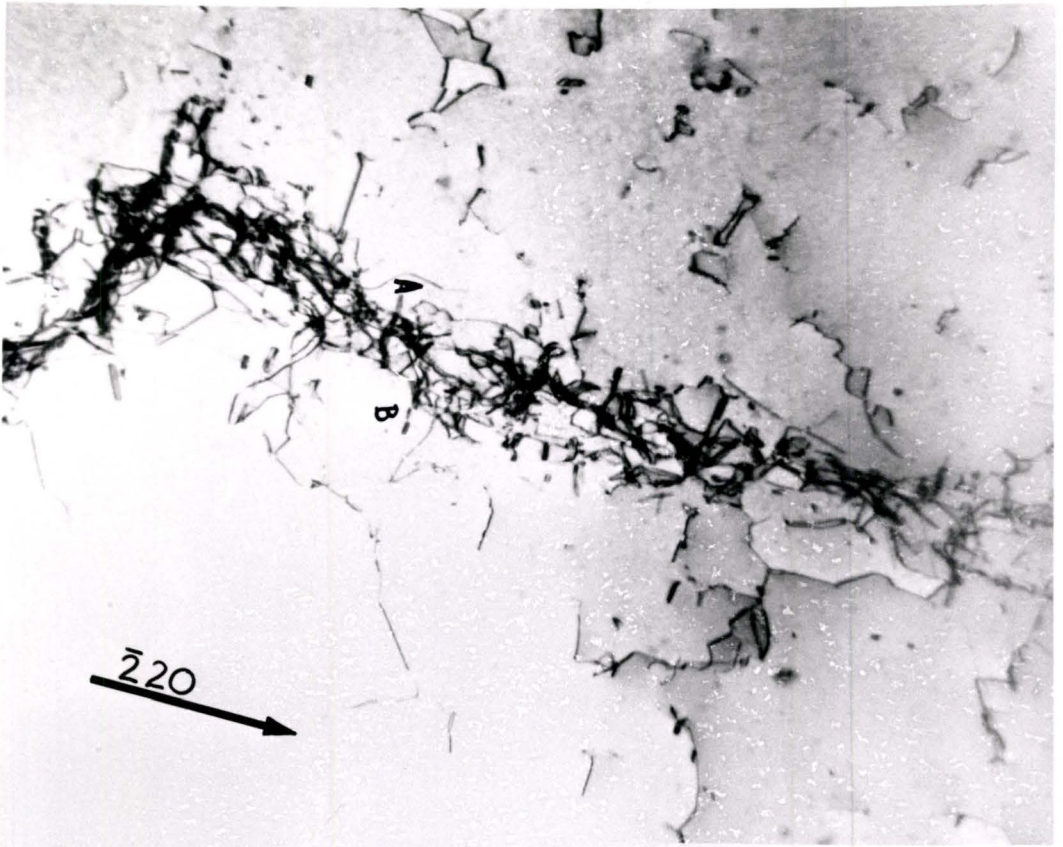
Strain: 21 cycles

Foil Normal: [111]

At 21 cycles, as mentioned previously, the braids are generally more dense, with a great deal more fine debris (dipole loops) present. This is seen to a greater extent in this particular area than in the one in micrograph #3 (21 cycles).

The particular aspect of this Burgers vector pair which is of interest is the proportion of coplanar dislocations  $\frac{a}{2} [1\bar{1}0]$  present in these relatively dense braids. Under the second operating reflection ( $g = 11\bar{1}$ ) the coplanars disappear (for example, the dipoles just above the point labelled "B") and it can be seen that these are again of mainly edge orientation.

There are a considerable number of dislocations lying close to  $[1\bar{2}1]$  and being in contrast under both reflections. These are presumably primary edge dipoles and dislocations. In addition, some dislocations are out of contrast under  $[\bar{2}20]$  (for example, just to the right of point A) and are in contrast under  $[11\bar{1}]$ . The dislocation has a Burgers vector  $\frac{a}{2} [110]$  and lies along  $[\bar{2}20]$ , the trace of the conjugate plane. This is therefore a Lomer-Cottrell lock formed by the operation of the primary and conjugate systems. It may be pointed out that the Schmid factor for the conjugate system is 0.137 whereas for the primary system it is 0.443. These short segments of Lomer-Cottrell locks are found in areas near the braids; presumably they also exist in the centres of braids where the dislocation density is too high to resolve individual dislocations.



#### 4.5.3 Micrograph #16

Strain: 50 cycles

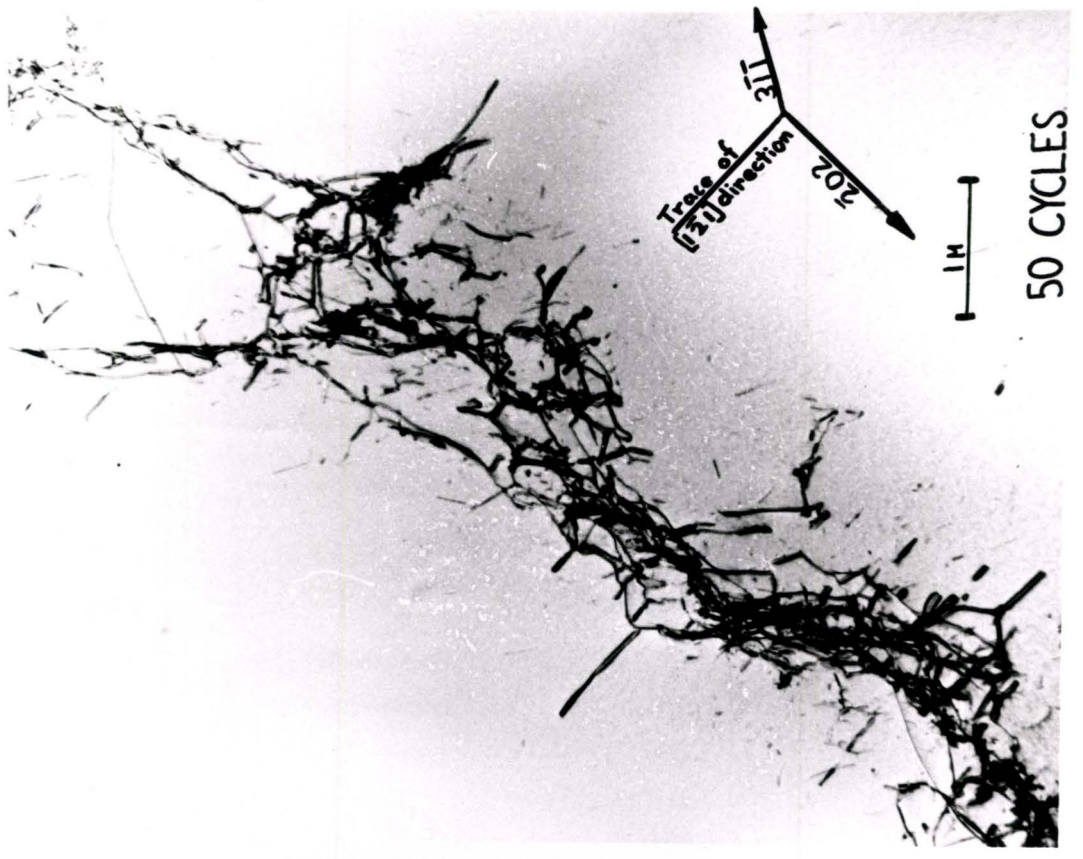
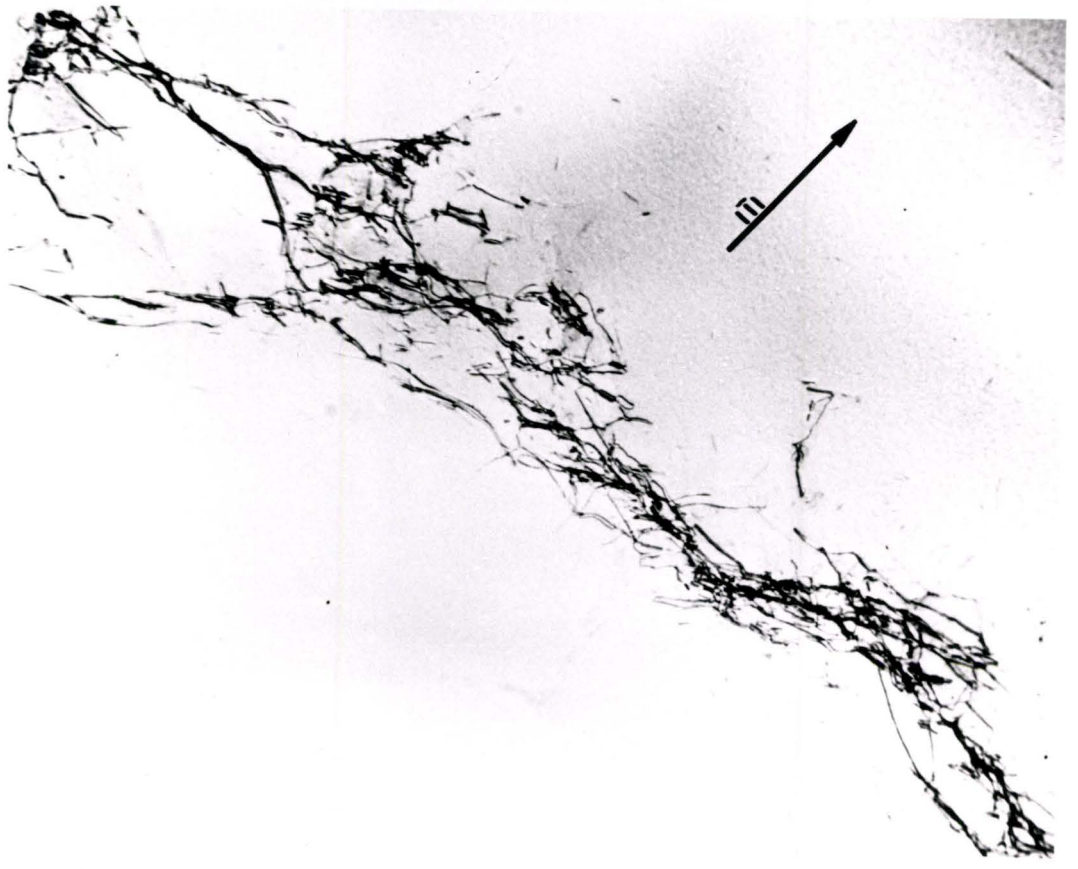
Foil Normal:  $[111]$

The 50 cycle microstructure was shown to be more homogeneously distributed than at 21 cycles, although particular regions at the earlier stage were similar to some areas at 50 cycles.

This Burgers vector pair shows a braid lying along  $[\bar{2}02]$  and indicates the density of non-primary dislocations at 50 cycles. Under  $[1\bar{1}1]$ , the primary dislocations (mainly edge type) are out of contrast while the non-primary (including coplanar) dislocations are in contrast. The density of secondary dislocations is seen to be quite high.

The second micrograph was taken while two operating reflections were of equal strength: the  $\bar{2}02$  and  $3\bar{1}\bar{1}$ . Under  $3\bar{1}\bar{1}$ , the primary and coplanar were both half images ( $\bar{g}\cdot\bar{b} = 2$ ) while under  $\bar{2}02$ , the primary was a half image and the coplanar a whole image.

For example, at some dislocations along the trace of  $\bar{1}\bar{1}2$  (edge orientation for coplanar dislocations), there is one strong image and one weak image parallel to each other. This is a typical type of image when 2 such reflections are operative.



#### 4.5.4 Micrograph #17 - Burgers Vector Determination

Strain: 50 cycles

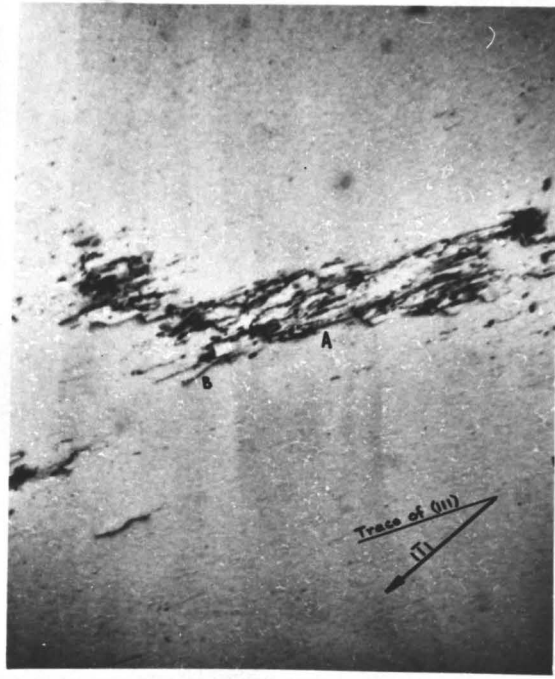
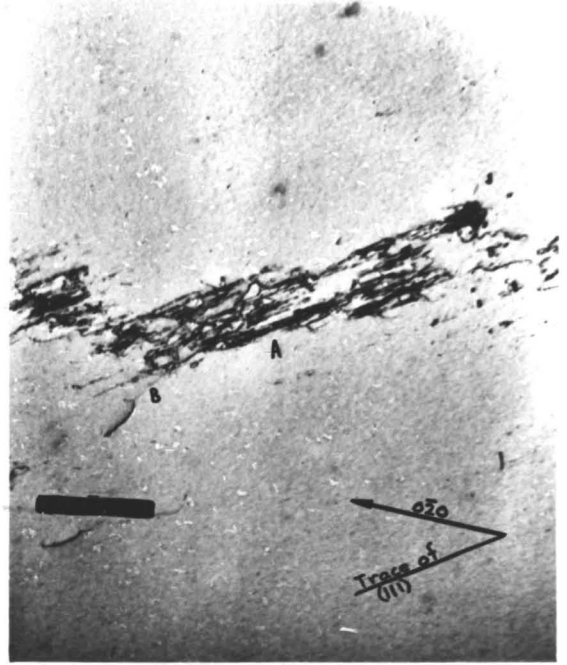
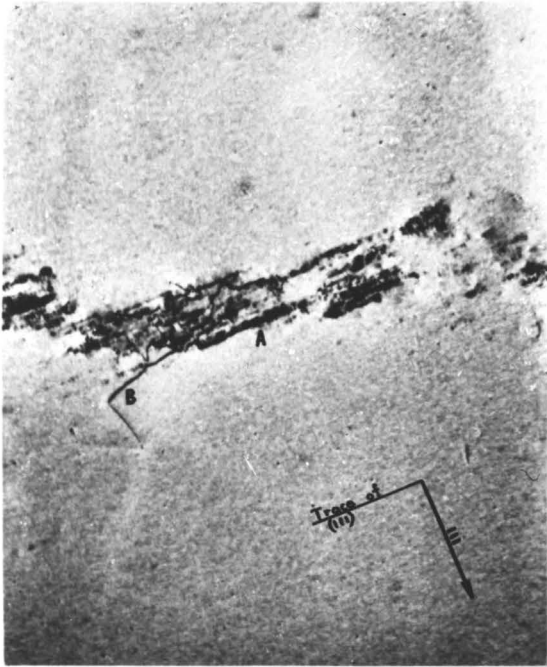
Foil Normal:  $[\bar{1}01]$

This is a group of 3 micrographs under different operating reflections taken of the same area.

Under all three reflections, the primary dislocations  $\frac{a}{2} [\bar{1}01]$  are out of contrast, the remainder are either coplanar  $\frac{a}{2} [1\bar{1}0]$  or non-coplanar secondaries.

Under the first operating reflection  $g_1 = 111$ , the coplanar  $\frac{a}{2} [1\bar{1}0]$  dislocations are out of contrast. The images seen here, are therefore the non-coplanar secondaries -- which appear as very short lengths concentrated in extremely dense packets (A). These packets are seen in random regions in the braid and are visible in all three reflections, although individually they are not entirely in contrast over all three reflections (only parts are sometimes seen). This suggests that these dense collections contain a number of types of secondary dislocations some of which go out of contrast under the different reflections. The longer forest dislocations similar to those seen at 5 cycles are again either  $\frac{a}{2} [110]$  or  $\frac{a}{2} [011]$  type (visible in  $111$ , invisible in  $1\bar{1}1$ ).

The long dislocation at B has a Burgers vector  $\frac{a}{2} [101]$  (critical) and lies along the edge direction  $[12\bar{1}]$  for a critical dislocation.



1M

#### 4.6 Summary: Part II - Burgers Vector Results

The Burgers vector analyses show that the initial barriers to slip in the first few cycles of fatigue hardening are forest dislocations, some of which have Burgers vectors either  $\frac{a}{2} [011]$  or  $\frac{a}{2} [110]$ . These analyses at 2 and 5 cycles also show that most of the dislocations which carry the strain lie in the primary plane and have Burgers vectors of the primary  $\frac{a}{2} [\bar{1}01]$  or the next most highly stressed system, the coplanar  $\frac{a}{2} [1\bar{1}0]$ . In the thin foils examined, these dislocations are generally in the edge orientation. A number of complex dislocation interactions are visible in the 2 and 5 cycle foils, however even the Burgers vector analyses do not clarify their exact mechanisms.

At 21 cycles, there is again a considerable fraction of coplanar  $\frac{a}{2} [1\bar{1}0]$  and primary  $\frac{a}{2} [\bar{1}01]$  dislocations present in the braids, with some secondary dislocations visible. In particular, Lomer-Cottrell locks were found to lie along the length of the braids in the immediate vicinity of the densely packed region at the centre.

At 50 cycles, there is a considerable density of non-primary dislocations present in the braids. The sections cut perpendicular to the primary plane revealed small "packets" of densely packed dislocations with various secondary system Burgers vectors. These "packets" were visible at random points in the braids in this  $(\bar{1}01)$  section.

The long forest dislocations of Burgers vector  $\frac{a}{2} [110]$  or  $\frac{a}{2} [011]$  were again visible at 50 cycles in the  $(\bar{1}01)$  section and their density was not visibly changed.

In summary, the Burgers vector results showed primarily that secondary dislocation content was quite high in the braids after the

first few cycles. The initial barriers to slip were forest dislocations, against which dipoles and dislocations of the primary plane are stopped. The later periods of hardening (21, 50 cycles) show Lomer-Cottrell locks within the braids.

#### 4.7 Experimental Results - Part III: Slip Line observations

The slip line replicas were taken from each sample at various stages during the cycling. Before cycling was started, and after a preliminary electropolish, the gauge length surface was checked for surface smoothness and any possible slip line markings left previous to electropolishing. In all cases, no slip lines were seen at any point on any surface before cycling commenced. This indicates that no macroscopic plastic deformation was introduced into the specimen during mounting or aligning; a verification of the stresses recorded on the chart during mounting (nevermore than 10 pounds -- much below the flow stress for the first half cycle).

At the end of cycling for each specimen (2, 5, 21, 50, 100 cycles), the cumulative slip line pattern was replicated, the surface was electropolished to a considerable depth to eliminate all traces of the cumulative slip (this was checked again by replicas) then the specimen was cycled through one complete cycle. At least three replicas were taken from each surface of the gauge length at this point. The specimen was then de-mounted. In the case of the 21 cycle and 50 cycle specimens, Watt's slip-unslip experiment (1967) was carried out to check for reversibility of slip. It was generally found that no such effect occurred but rather that new slip lines appeared after the compressive stroke and the tensile slip lines all remained (indicating that it is not a reversible mechanical process).

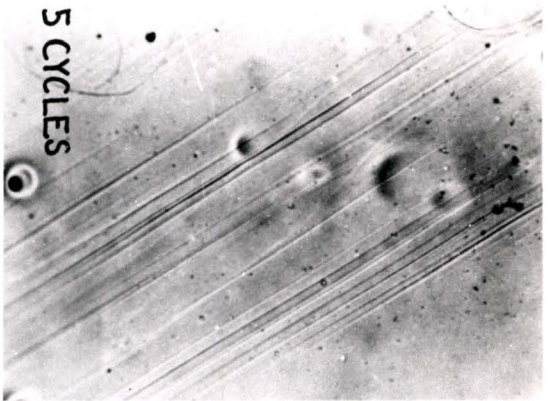
The 100 cycle specimen was checked with replicas at 2, 5, 20, 50 and 100 cycles as outlined above. These were compared to the results

from each crystal and found to agree quite well. The slip line results were all taken from the 100 cycle specimen in order to have a more consistent story. Photograph #18 shows the slip line behaviour over the first 100 cycles from a given surface of the 100 cycle specimen (the  $[\bar{1}01]$  primary slip direction emerges directly out of this face).

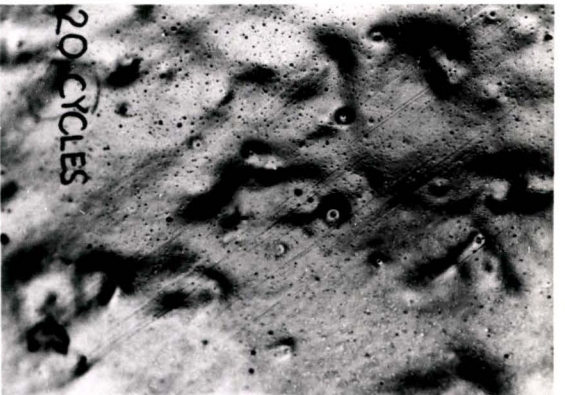
The significant result to note here is that the slip lines get progressively shorter and finer during the rapid hardening stage. The individual micrographs were taken at low magnification, so the length of slip lines is still quite long at 100 cycles and is at least one order of magnitude greater than comparable mean free paths seen in the micrographs showing the dislocation microstructure. Thus, no direct correlation can be made between the obstacle spacing and the slip line length except the qualitative statement that a decrease in obstacle spacing is reflected in a reduction in the slip line length as noted by Mader in unidirectional deformation.



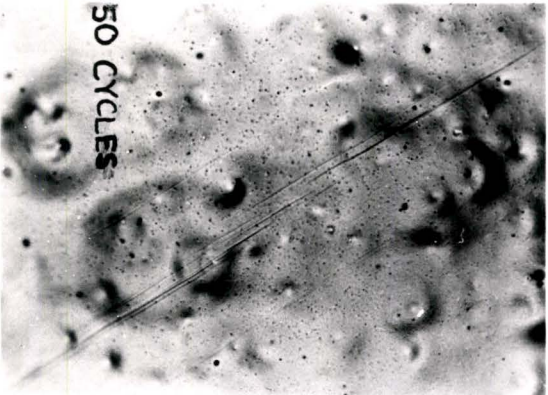
2 CYCLES



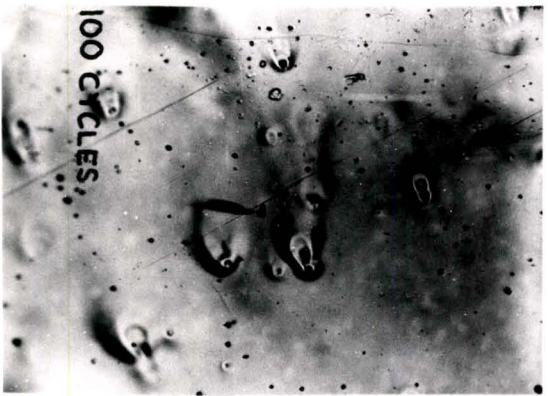
5 CYCLES



20 CYCLES



50 CYCLES



100 CYCLES

Development of Slip Lines  
During Early Stages of  
Fatigue Hardening

200 μ

## CHAPTER 5

### DISCUSSION

The large uncertainty in fatigue hardening theories is mainly due to a lack of reliable, self-consistent experimental results. This lack is an indication not only of insufficient numbers of experiments, but also of the difficulty in comparing results derived by various techniques. The experimental work which has been reported in the literature has often been of excellent quality, but different workers have used different approaches (such as in the mode of stressing: bend tests, torsion tests, uniaxial tests and constant stress or strain tests). The question is basically whether the mechanical response, dislocation microstructure and surface topology resulting from one approach can be compared with those of any other.

The bend test introduces varying stress levels across the cross-section of the specimen, and it is questionable that the dislocation microstructure generated by such a stress field is the same as that for a uniaxial test (except at some points in the cross-section). The problem of how instabilities in the dislocation microstructure can arise and therefore produce the observed persistent slip band phenomenon obviously depends on the homogeneity of the dislocation microstructure and the nature of the barrier distribution.

It would appear that the bend test may be less than satisfactory to investigate these problems.

The same difficulty arises in the torsional test, where the slip systems which are activated depend on the particular region of the single crystal one is considering. Surface slip activity, dislocation microstructure and mechanical response become rather difficult, if not totally impossible to interpret. (However, Nine and Kuhlmann-Wilsdorf (1967) have attempted it.) Even if it were possible, there is a further problem of relating such results to others from bend tests (Laufer and Roberts (1966)).

Constant stress tests, as opposed to constant strain tests, introduce another, different problem. As mentioned earlier in the literature review, Kettunen uses constant stress and analyzes all of his results without emphasizing the difference between such tests and ones at constant strain. The whole question of fatigue hardening depends on the nature, and mode of generation of obstacles to slip. If a constant stress test is used, unless an extremely tiny stress is used (less than  $1 \text{ kg/mm}^2$ ), the strain introduced into the sample on the first quarter cycle is much higher than that put into a sample fatigued at low amplitude constant strain. In fact, if the saturated state stress (for low amplitude) is used as the stress limit, then the first quarter cycle (whether tensile or compressive) corresponds to unidirectional stressing up to stage II or perhaps even as far as stage III. The barriers to dislocation movement which are formed are exactly those formed in uni-directional tests into stage II or III. If one compares this to a constant strain test, where the first quarter cycle is only into the easy glide stage I, then the barriers to slip created in constant stress are very different from

those in constant strain after the first quarter cycle. If the nature and distribution of obstacles are very different after 1/4 cycle, then the hardening mechanisms between 1/4 cycle and saturation will be different.

The only way the two modes of testing can be compared is by performing hardening experiments on a number of identically oriented crystals and comparing the dislocation microstructures as they build up in hardening. The results would not only show how the hardening mechanisms differ, but also how the barrier distribution at saturation compares to the barrier distribution after stage II work hardening. In view of the qualitative similarity between the microstructures, such a direct comparison may reveal quantitative similarities and provide a more solid basis for use of work hardening mechanisms in fatigue.

### 5.1 Comparison of Experimental Results to Other Theories

Feltner (1965) The experimental results clearly show that the dislocation-dipole tangles develop into effective obstacles very early in the hardening regions. Feltner's fundamental premise that the dipole debris act as the primary hardening obstacles is therefore not justified. Although the debris may indeed affect the hardening, its importance relative to the much more effective dislocation braids appears to be minimal. As seen in micrograph #5, almost all dipoles are incorporated into the braids at 50 cycles. The low magnification composite (micrograph #6) at 50 cycles also shows that very few dislocations or dipoles can be found in the matrix.

The mode of carrying strain suggested by Feltner (flip-flop motion of dipoles) would be most effective for non-interacting dipoles. That is, the short range interaction of dipoles with other dipoles, with primary and with secondary dislocations, would hinder the flip-flop process. The dislocation microstructure shows that as hardening progresses, the density of dipoles and dislocations from all systems increases in the braids. In addition, the dipoles become much finer in scale and hence would become more difficult to flip (since the sessile ends would be relatively more important). This raises the problem of how strain can be accommodated by dipoles flipping and flopping if they become harder to flip with hardening. The movement of dislocations between the braids must simultaneously become more difficult. The hardening obstacles must increase in density and/or effectiveness. Feltner's proposal that dipole debris act as obstacles must therefore mean that such dipoles must be becoming more common in the region between the braids. Since they do not, they must not act as the obstacles primarily responsible for hardening. The braids, however, do react in that manner -- their density and effectiveness as obstacles increase as hardening proceeds. The movement of dislocations in the matrix thus becomes more difficult. In this way strain can be transferred to the dipoles flipping, provided the rate of increase of hardening by braid formation is greater than the rate of increase of making dipoles harder to flip.

The question remains whether dipoles which flip from one position to the other actually carry an appreciable amount of the strain at saturation. The proposal that dipoles act as primary hardening obstacles seems to be invalid.

Perhaps a hint as to whether dipoles do carry most of the strain at saturation may be given by the following observation. The production of persistent slip bands at saturation suggests that slip is inhomogeneous in the crystal. If dipoles carry the strain, one cannot explain how inhomogeneities may be generated in the matrix or how intrusions and extrusions are formed.

Broom and Ham (1959)

The principle of hardening due to point defect diffusion is not easily proven or disproven by electron microscope techniques, simply because the defects are unresolvable by the microscope. However the supposition that vacancies diffuse to dislocations, thereby jogging the dislocations and effectively pinning the line at that point, can be checked qualitatively by observing the distribution of cusped dislocations in the matrix. If the jogging mechanism is significant, one would expect that dislocations away from the tangled regions would be heavily jogged. The jogging of dislocations in the centres of tangles would be much less important to hardening since it is apparent that dislocations in the matrix carry the strain in hardening (at least early in that stage) and hence hardening obstacles must be generated which impede their motion.

Therefore one should study dislocations of the primary system in the matrix (tangle-free areas). Careful observations of such areas throughout the hardening regions show that there are few regions of heavily jogged dislocations outside of tangled regions. This is particularly true of specimens from the very early stages (2, 5 cycles) where

there is evidence of long, jog-free lengths of dislocations (see micrograph #1 and #2). The hardening at these points is apparently occurring mainly by interactions of dislocations on the primary plane with each other and with forest dislocations (see micrograph #14) and not by jogging mechanisms.

At greater numbers of cycles (21, 50, 100 cycles) where the braid-like formations become much more well defined, there is evidence of considerable jogging of dislocations within the braids (especially visible in  $(\bar{1}01)$  sections: micrograph #7). This is probably due to mutual cutting processes of non-parallel dislocations, particularly since there are comparable numbers of primary and secondary dislocations in the tangles.

The role of vacancies in fatigue may be not in the actual hardening mechanisms, but rather in a form of dynamic recovery process, where the vacancies can diffuse to jogged dislocations in the braids and allow non-conservative motion of the jogged segments into lower energy configurations relative to other dislocations in the tangles. This, of course, has not been experimentally proven, but with the large numbers of jogs and the apparent high density of vacancies in fatigued metals (Broom and Ham (1959)), some such process must occur. There is also the probability of climb of the longer dislocations in the braids into more stable arrangements. This suggests that experiments in fatigue hardening at lower temperatures and the subsequent pinning of dislocations by neutron irradiation to prevent thermal recovery upon heating to room temperature may reveal more useful information about the dislocation

interactions and the role of vacancies in fatigue hardening.

### Avery and Backofen (1963)

This hardening rationale proposed that point defects conglomerate to form very small loops which themselves act as barriers to slip and produce a net hardening. In order to be effective obstacles relative to tangles, these loops must therefore be in the tangle free areas of the crystal and the vacancy producing jogged dislocations must be found in fairly large numbers between the braids. Neither small loops or jogged dislocations have been generally observed in regions other than the neighbourhood of braids. The conclusions must be that such a hardening mechanism is not very important in the fatigue of copper.

## 5.2 Proposed Model for Fatigue Hardening

### 5.2.1 Introduction

In order to devise a model applicable to the fatigue hardening phenomenon, it is necessary to understand all of the basic questions which must be answered simultaneously by any theory:

- (a) Why does the flow stress increase on each cycle?
- (b) Why does the hardening rate decrease and approach a "saturated state", and how is it related to strain amplitude?
- (c) How does the dislocation microstructure depend on plastic strain amplitude?
- (d) How are the elements of the microstructure (such as dipoles, Frank dislocations, etc.) formed?
- (e) Can the dislocation microstructure account for the surface markings

such as fine slip in the hardening regions, persistent slip bands in the saturated state, intrusions and extrusions, etc.?

(f) How is the dislocation microstructure stable on reverse stressing?

Any hardening mechanism which can answer all these when faced with a reasonably reliable set of experimental observations has at least some chance of success. It can be seen that the conditions given above are exactly parallel to those necessary for work hardening theories in uniaxial tension.

The present hypothesis is an attempt to rationalize the experimental results outlined in the previous chapter in such a way that the questions fundamental to the hardening model can be answered.

### 5.2.2. The Model

The most striking aspect of the dislocation microstructure as it develops in fatigue is the similarity of the overall geometry and composition (types of Burgers vectors) to those of copper deformed in unidirectional pulled well up into stage II. There are obvious characteristics in the microstructure, notably dipole concentration and formation later in hardening and some curious dislocation interactions very early in hardening, which are peculiar to fatigue. However, the qualitative descriptions of the two types of microstructures are virtually identical. This similarity suggested that the nature of the barriers to slip were also identical and consequently, the interpretation of the observations was sought in the work hardening models of stage II.

A qualitative description of the sequence of events occurring in hardening may be presented as follows. In the well annealed single

crystal, there is a random arrangement of various dislocations in the crystal (say with a density of  $10^5$ ,  $10^6$  lines/cm<sup>2</sup>). The initial tensile strain (first quarter cycle) causes the operation of the primary system such that  $\frac{a}{2}$   $[\bar{1}01]$  dislocations move. These dislocations produce dipoles (Appendix I) in one or both of two ways: the Tetelman mechanism or the Johnston and Gilman mechanism.

There appears to be no conclusive evidence favouring either mechanism, although suggestions of both have been seen.

At this early stage of the hardening, the Tetelman mechanism would produce dipoles at random through the matrix, since no criteria other than anti-parallel dislocations are necessary for it to operate. The Johnston and Gilman mechanism would produce dipoles near small obstacles which would tend to jog the glide dislocation -- such as small loops or areas of forest dislocations.

However these dipoles are produced, they are are apparently "swept" into "hard" regions by primary edge dislocations by the Sharp and Makin mechanism (1964) ( Chapter 2 ). This is especially evident in the  $(\bar{1}01)$  sections shown in micrographs #14 and #17, where high densities of primary plane dipoles are associated with a few long forest dislocations. The initial barriers to slip appear to be the forest dislocations, which stop dipoles being pushed along by glide dislocations. This seems reasonable in view of the fact that there is no apparent reason for dipoles to be formed in such a localized region at 5 cycles. Both dipole formation mechanisms require some dislocation movement on the primary plane, certainly over distances at least as long as the dipole.

Therefore one would expect that dipoles should be formed in the tangle-free matrix, at least at 5 cycles. (Later, the Tetelman mechanism may account for dipoles formed on secondary systems within the braids, but very early in hardening, where only the primary system is operative, there is no reason why primary dipoles should preferentially form over a long length of forest dislocation ). If these dipoles are formed in the matrix, there must be some mechanism of moving them into regions of forest dislocations, such as the mechanism proposed by Sharp and Makin.

### 5.3 Forest Dislocations as Initial Barriers to Slip

The primary reason for believing that forest dislocations play an important role very early in hardening is that they are the only visible barriers to glide on the primary system in the virgin crystal. There is an alternative possibility that in this particular orientation for the crystal, where primary and coplanar systems are very nearly equally stressed, the interaction of primary and coplanar dislocations can produce dislocations of the third coplanar Burgers vector which is very lightly stressed and immobile under straining. Primary system dislocations can then pile-up against these. However, such dislocations are not seen at 2 or 5 cycles, and their existence could not explain the long collections of primary dipoles which arrange themselves along forest dislocations.

A calculation of the stress field around a forest dislocation ( $\frac{a}{2}$  [110] or  $\frac{a}{2}$  [011]) acting on a primary Burgers vector dipole would be very useful in determining the effectiveness of the forest dislocation in stopping and pinning such dipoles. A method of calculation as outlined in Appendix 3 can be used to obtain the stress field in the

primary plane. However, the solutions require considerable numerical computation and will be performed later.

If this calculation shows that the forest is an effective obstacle, then the subsequent trapping of dipoles can be calculated by the method given by Chen Gilman and Head (1964). This calculation shows that dipoles can trap edge dislocations moving nearby and at the same time exert a dynamic force on moving dislocations which reduces its "mobility". The dipole arrays seen at 5 cycles are therefore effective obstacles to slip of edge dislocations.

This conclusion that forest dislocations are the primary hardening obstacles in the first few cycles agrees with the fact that the braid orientation is randomly distributed over all three close-packed directions in the primary plane. If some other obstacles such as a sessile length of dislocation produced by the reaction of primary and coplanar systems were important, one would expect a much more directional orientation of the braids in the primary plane.

In addition, Grosskreutz (1968) has observed that specimens which were "bent inadvertantly" before cycling "always hardened more rapidly, although the saturation stress was unaffected". This agrees with the concept of forest dislocations acting as initial barriers to slip, since if the crystal was "bent inadvertantly", the population of forest dislocations would be higher and the barriers to initial slip more numerous. The hardening rate, insofar as it depended on forest dislocations and pile-ups against these forests would therefore increase. The reason why the saturation stress remains constant will be discussed later.

#### 5.4 Stress Relief by Secondary Slip

The continued cycling of the crystal results in more slip on the primary plane and some kind of primary dislocation pile up at the dipole barriers. When the spacing between barriers is quite large (early in hardening), these pile-ups are quite short (see Hirsch (1967)) and the stresses at the head of the pile-up are not very large. The growth of the braids at the forest dislocations by the tangling of primary dipoles and dislocations gradually shortens the mean free path of the mobile dislocations, necessitating an increase in the population of glide dislocations. The numbers of dislocations in the pile-ups are now greater than before and the stresses along secondary systems are likewise greater. The shorter mean free path effectively means the stress to maintain the strain imposed by 1/4 cycle must increase (hardening). The stresses along secondary systems increases until slip can be generated on these systems. At this point, the heads of the pile-ups become transformed into regions of extremely complex dislocation tangles, containing dislocations of all Burgers vectors. This stress relief by secondary slip was suggested by Hirsch and Mitchell (1967) in connection with stage II work hardening (see the Literature Review).

The heads of these pile-ups are therefore located within the initial collections of primary dipoles (initial braids) and these braids become extremely effective obstacles to slip, being both "hard" to glide dislocations and fairly continuous through the matrix (see micrograph #6 showing the low magnification of the long braids now connected at 50 cycles).

This sort of dislocation microstructure can be seen in the process of generation in the first series of micrographs #1 to #11, where the braids are isolated and not very dense initially, with evidence of much parallel interaction (at 2 and 5 cycles); then they gradually join up to form more continuous networks (21 and 50 cycles) which are much more dense and contain large proportions of non-coplanar secondary dislocations (from Burgers vector analysis micrographs #15 and #16).

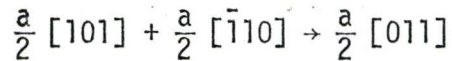
The  $(\bar{1}01)$  sections show the dipoles of the primary plane associated with forest dislocations, with most of the dislocations being of the primary system early in hardening (5 cycles) but gradually showing patches of high densities of secondary dislocations (50 cycles) which are those areas at the heads of pile-ups where secondary slip occurs. The secondary slip is very localized and very short, so no slip lines corresponding to the secondary slip systems would be expected. Also, the primary dislocations would still carry almost all of the strain imposed on the crystal.

### 5.5 Orientation of Braids

As the braids build up by secondary slip, the ones aligned along the trace of the critical plane appear to grow preferentially. (see micrograph #9 and #10). This may be explained by the production of locking dislocations along these traces.

The Schmid factor for the critical system is the highest for any non-coplanar secondary system. It is expected from this, and from the calculated stresses on secondary systems for this orientation (Mitchell (1964)) that under the combined action of the applied stress and the stress due to a pile-up of primary dislocations, the critical system

should be activated preferentially. This means that as critical dislocations are produced they can react with coplanar dislocations to produce Lomer-Cottrell locks of the type  $\frac{a}{2} [011]$  by the reaction



which lies along  $[01\bar{1}]$ , the trace of the critical plane.

From the knowledge that both the  $\frac{a}{2} [\bar{1}10]$  coplanar and the  $\frac{a}{2} [101]$  critical dislocations are highly stressed and are operated with relatively little assistance, it can be seen that such a reaction is very plausible.

The alternative of the primary plus conjugate system producing a Lomer-Cottrell along the trace of the conjugate plane is less likely since the conjugate system has a Schmid factor 0.137 and requires considerably more assistance to operate than the critical or coplanar.

One would therefore expect that relatively early (say 20 cycles), the primary pile-ups would cause secondary slip which would produce Lomer-Cottrell locks along the trace of the critical plane in the middle of the braids. The braids which lie along the trace of the critical plane would become more effective obstacles than others since the Lomer-Cottrell locks are very effective in stopping slip. Since they are more effective, they would tend to build up at the expense of other orientations of braids. The result is a tendency for braids to orient along the trace of the critical plane later in the hardening and at saturation. This can be seen in micrographs #9 and #10.

This sort of mechanism explains why the braids are randomly oriented early (2, 5, 21 cycles) in hardening and later take up a preferred

orientation (100 cycles). Lomer-Cottrell locks formed from the operation of the primary and conjugate systems are shown in micrograph #15 at point "A". This shows that such locks are generated by this sort of model and by inference, the Lomer-Cottrell locks along  $[01\bar{1}]$  can be assumed.

At this point, Grosskreutz's second observation that the random bending of crystals before cycling results in the same saturation stress can be explained. The preferred orientation of the braids and the ultimate effectiveness of the braids as obstacles depends upon the orientation of the crystal and where the Lomer-Cottrell locks are formed. The introduction of random forest dislocations and so on would result in increased hardening rate since the number of initial barriers to slip is higher. But they do not affect the later stages of braid growth, since this is largely determined by the nature and extent of the secondary accommodating slip. Hence the final dislocation structure depends primarily upon the orientation of the crystal and not so much on the initial random dislocation content. However, if the initial bending or damage to the crystal is very large, so that stage II or stage III has been reached before cycling, then the barriers are already networks of braids and it would be expected that the final structure may depend very greatly upon this initial structure. This is similar to the discussion already given in relation to the constant stress tests.

#### 5.6 Dipoles in Hardening

The role of dipoles in hardening is not completely understood, but it is apparent that they play an important role early in hardening

where they associate themselves with forest dislocation and form the nuclei for complex braids later on.

The initial dipoles are extremely long and are presumably the dipoles as formed initially. As these are pushed into tangles and secondary slip occurs in the braids, these dipoles become "chopped up" into finer and finer loops as secondary dislocations moving in the region of the braids intersect these primary and coplanar dipoles. The overall dipole density also must increase with cycling, since it is difficult to see how a few dipoles seen at 5 cycles can be chopped up into so many fine dipoles at saturation.

It has been pointed out that dipoles may be an important strain carrying element in the microstructure. However, discussion by Watt has shown that this is probably not the case.

It therefore appears that dipoles are primarily important to the hardening mechanism very early in the hardening regime. Their importance decreases as secondary slip is generated and the dipole arrays become complex tangles.

### 5.7 The Saturated State

From the hardening model proposed above, and from the dislocation microstructures visible at saturation, it seems likely that the plastic strain at saturation is carried principally by dislocations moving on the primary plane in the tangle-free matrix. The braids, which are very densely packed structures at saturation, are simply hard barriers which restrict the motion of the dislocations. The fact that the peak stress on each cycle is constant at saturation suggests that the hardening

mechanism proposed above has stopped and the braids are no longer growing and the spacing between them is not decreasing. This in turn means that a sort of equilibrium has been reached in which the dislocations moving on the primary plane no longer generate secondary slip at the heads of their pile-ups and the dislocations simply move back and forth between the braids. It is possible that the dislocations may become entangled in the braids on one half cycle, while on the reverse cycle, other dislocations are pulled free from the braids to carry the strain. The net effect is the same as if the same dislocations carry the strain in both directions.

#### 5.8 Dislocation Microstructure and Strain Amplitude

From the proposal that dislocations moving on the primary plane carry the strain in hardening and in saturation, it is expected that if the strain amplitude is raised, there will be two main effects.

First, since the strain introduced by each cycle is greater, the number of dislocations moving in the primary plane is greater. The numbers of dislocations in the primary pile-ups is greater than at lower strain amplitudes. Therefore the extent of secondary accommodating slip is greater and the braids grow faster. Since the hardening rate depends upon the growth rate of the braids, the hardening rate should increase as the strain amplitude increases.

The second effect of raising the strain amplitude is that the scale of the microstructure decreases and the braids at saturation are closer together. This can be explained if the strain carrying elements at saturation are the dislocations moving between the braids. Since

the mean free path of such dislocations has decreased as the braids grow closer together at higher amplitudes, then the number of dislocations carrying the strain must increase. These strain carrying dislocations are pulled from the braids on each half cycle. Since the volume fraction of braids has increased, the numbers of dislocations which can be pulled out of the braids has increased. Therefore the increase in strain amplitude can be correlated qualitatively to the decrease in braid spacing as reported by Pratt (1966).

### 5.9 Experimental Errors

In judging the validity of the present results, some attention should be given to the nature of the experimental errors inherent in the technique.

The first error concerns that in the hardening curve as plotted in graph #1 and #2 in the experimental results. The only source of error here was in the measurement of the peak stress and the plastic strain amplitude. The peak stress was calculated using the Schmid factor (for the primary system) and the crosssectional area. The error in the Schmid factor was small, of the order of  $\pm 4\%$ , which arises from errors in measuring the angles on a stereographic projection and the errors in plotting the tensile axis by Laue back reflection techniques.

The error in the crosssectional area was negligible, about  $\pm 3$  or  $4\%$ , if an error of  $\pm .003$  inches was assumed on the measurements. The crosssectional area did not vary in width by more than  $\pm .0015$  inches over the length of the gauge length for any pair of faces. The gauge lengths were as close to centrally axial as could be seen on the optical

comparator and no significant changes in curvature were seen in the profile of the surface on any specimen.

The maximum possible error in the peak stress was therefore about 10% if an error in the chart recorder is set at 2%. However, very little scatter was observed in any of the results on the hardening curves. The most probable explanation is that the error was mainly a systematic error such as an error in the Schmid factor -- which was used for all calculations. Other errors, such as crosssectional area, chart recorder errors and so on, would be random errors which would very likely appear as experimental scatter about the mean curve.

There was also an error in the plastic strain for each cycle and except for the initial few cycles (where the faster chart speed and beam speed allowed a  $\pm 2\%$  errors), the error was about  $\pm 4\%$ . Such an error, if random, would probably not affect the dislocation microstructure to any noticeable degree.

Besides the numerical errors above, there are other errors which have to do with statistics. The microscope thin films were taken from sections cut towards the centre of each gauge length at random positions. What must be assumed is that the dislocation microstructures are representative of the bulk specimen. This assumption depends on the homogeneity of the dislocation microstructure, against which there is no serious argument (at least during hardening) and also on the lack of rearrangement of dislocations as the section is thinned to a couple of thousand Ångstroms. This latter is a contentious point as mentioned in connection with Seeger's work hardening theory, and it has been assumed

here that although some rearrangement undoubtedly exists, the important characteristics of the microstructure are still intact after thinning. This is especially true after 21 cycles, where secondary slip occurs and complex tangling occurs. The braids become so dense and tangled that the rearrangement that does occur must be insignificant.

Also, a sort of statistical "error" is the assumption that the Burgers vector determinations shown in the results are typical of the whole microstructure. This and the previous "error" concerning the homogeneity of the dislocation arrangement are eliminated simply by considering a large enough area and studying many areas carefully. It is felt that such care has been taken and that the Burgers vector determinations and dislocation distributions shown are representative of the bulk microstructure.

As a final sort of error, there are errors in the images due to the aberrations inherent in the microscope and its use. Such things as chromatic aberration, spherical aberration, astigmatism and so on are covered in sufficient detail in Hirsch, Howie, Nicholson, Pashley and Whelan (1967) and no details will be discussed here.

#### 5.10 Summary

It was the initial principle of this work to utilize a simple system and to obtain the maximum information out of such a system by carefully experimentation. The simple system chosen was single crystal copper cycled in uniaxial symmetric push-pull. The experimentation was primarily the use of careful quantitative electron microscopy on a few crystals.

The most important contribution of this thesis is the addition it makes to the knowledge of the dislocation microstructure as a function of fatigue straining. Careful examination of this microstructure, in its overall geometry and in its detailed composition, has yielded considerable information with regard to the nature of the barriers to slip which are created in fatigue. This information has been analyzed to deduce the dislocation interactions which control the hardening mechanism and the following model has been proposed.

The initial reactions are the interactions of dislocations and dipoles of the primary system with forest dislocations. A large number of the dipoles appear to arise by the parallel interaction of dislocations moving on the primary plane.

Stress relief of primary dislocation pile-ups by secondary slip increases the density of secondary dislocations and produces complex braids. The distribution of secondary dislocations is in agreement with relief of internal stress of primary pile-ups by the most active secondary system. The resultant dislocations react to form Lomer-Cottrell locks parallel to the trace of the critical plane and hence stable barriers preferentially aligned along this trace.

## CHAPTER 6

### CONCLUSIONS

A detailed picture of the dislocation distribution in fatigue hardening has been obtained for copper single crystals of one orientation at room temperature.

At the initial part of hardening (2 cycles), the dislocations are mostly primary and coplanar dislocations found in isolated groups well separated from each other. Very quickly (5 cycles), the density of dislocations increases, and many of them are found in "Y" configuration braids of high density. These braids are isolated in small regions of a dislocation-free matrix. At this early stage, arrays of primary dislocations and dipoles are associated with forest dislocations.

As cycling progresses, the density of braids increases and the density of dislocations within the braids increases. Secondary non-coplanar dislocations are seen to make up a considerable proportion of the braids after 21 cycles. Lomer-Cottrell locks are seen to exist in the neighbourhood of braids as early as 21 cycles.

The density of braids continues to increase with cycling until a very uniform distribution is seen at 100 cycles. These braids are in the form of elongated "cells" (seen in the primary plane). The scale of the microstructure is virtually the same at saturation as at 100 cycles although some dislocation "walls", separating regions mis-oriented to each other by small amounts, are seen at saturation and not at 100 cycles.

Slip line studies show that the length of slip lines decreases as the hardening progresses. No direct correlation between slip line length and dislocation microstructure scale could be seen.

Based upon these experimental observations, a model for fatigue hardening was proposed. The striking similarity between the dislocation microstructures seen in stage two uni-directional work hardening and the microstructures in fatigue hardening suggested that the mechanisms of debris accumulation are identical in the two cases. A satisfactory comparison can be made between a modified form of Hirsch's stress relief model for stage two work hardening and fatigue hardening.

However, the role of point defects in fatigue hardening is not clearly understood on the basis of the experimental observations and some form of point defect hardening may occur in addition to the hardening mechanism outlined here.

#### Proposals for Future Work

The observations obtained show that there is a plausible correlation between work hardening theories and fatigue hardening models for single crystal copper deformed at room temperature.

It would be interesting to vary the temperature to determine the temperature dependence of the fatigue hardening rate. The considerable effect of temperature on point defects may be reflected in the hardening rate. In any case, more information regarding the role of vacancies in fatigue hardening could be obtained by these experiments.

An important area to be considered in the future is the detailed microstructural changes involved in the growth of structural instabilities

such as persistent slip bands. This can be approached by detailed electron microscope observations of regions close to the surface of the crystal coupled with the development of dislocation models to describe the changes in the microstructure.

The similarities between the microstructural features observed in uni-directional work hardening and fatigue hardening suggest that an investigation of fatigue hardening in two phase systems would be of considerable value. In the case of materials containing hard stable particles this may yield some information to enable a more unified approach to be made to the problems of work hardening, fatigue hardening and precipitation hardening. In the case of soft particles, detailed investigations of the type reported here may give some insight into the microstructural instabilities which give rise to low fatigue ratios in this type of material.

## BIBLIOGRAPHY

- Alden, T. H. and Backofen, W. A., 1961, Acta Met. 9, 352.
- Avery, D. H. and Backofen, W. A. 1963, Acta Met. 11, 653.
- Basinski, Z. S., 1964, Discussions of the Faraday Society, Dislocations in Solids #38, 93.
- Basinski, Z. S., and Basinski, S. J., 1964, Phil. Mag. 9, 41.
- Broom, T. and Ham, R. K., 1957, Proc. Roy. Soc., A242, 166.
- Broom, T. and Ham, R. K., 1959, Proc. Roy. Soc. A251, 186.
- Clarebrough, L. M. and Hargreaves, M. E., 1959, Prog. Met. Phys. 8, 1.
- Feltner, C. E., 1965, Phil. Mag. 12, 1229.
- Feltner, C. E. and Laird, , 1967, Acta Met. 15, 1621.
- Fourie, J. T., 1964, Phil. Mag. 10, 1027.
- Fourie, J. T. and Murphy, R. J., Phil. Mag. 7, 1617.
- Gilman, J. J., 1962, J. Appl. Phys., 33, 2703.
- Grosskreutz and Waldon, 1963, Acta Met. 11, 717.
- Hancock, J. R. and Grosskreutz, J. C., 1968, United States Air Force Contract No. AF33-615-67-C-1547
- Hirsch, P. B., 1960, Acta Cryst. 13, 114.
- Hirsch, P. B., 1963, N.P.L. #15, The Relation Between Structure and Mechanical Properties of Metals, 40.
- Hirsch, P. B., 1964, Discussions of the Faraday Society 38, 111.
- Hirsch, P. B., Howie, A., Nicholson, R. B., Pashley, D. W., Whelan, M. J., 1965, Electron Microscopy of Thin Crystals (Butterworth).

- Hirsch, P. B. and Mitchell, T. E., 1967, Can. Journ. of Phys., 45, 663.
- Holt, D. B., Nabarro, F. R. N., Basinski, Z. S., 1964, Adv. in Phys. 13, 193.
- Kemsley, D. S., and Paterson, M. S., 1960, Acta Met. 8, 453.
- Kettunen, P. O., 1967, Acta Met. 15, 125.
- Kronmuller, H., 1967, Can. Journ. Phys., 45, 631.
- Laufer, E. E. and Roberts, W. N., 1964, Phil. Mag. 10, 883.
- Laufer E. E. and Roberts, W. N., 1966, Phil. Mag. 14, 65.
- Lukas, P., Klesnil, M., Krejci, J., and Rys, P., 1966, Phys. Stat. Solidi. 15, 71.
- Mader, S., 1957, Z. Phys., 149, 73.
- Nine, H. D. and Kuhlmann-Wilsdorf, D., 1967, Can. Journ. Phys. 45, 865.
- Pratt, J. E., 1967, Acta Met. 15, 319.
- Seeger, A., 1963, Relation Between Structure and Properties of Metals, 4.
- Segall, R. L., and Partridge, P. G., 1959, Phil. Mag. 4, 912.
- Segall, R. L., Partridge, P. G. and Hirsch, P. B., 1962, Phil. Mag. 6, 1493.
- Sharp, J. V. and Makin, M. K., 1964, Phil. Mag. 10, 1011.
- Snowden, K. U., 1963, Acta Met. 11, 675.
- Steeds, J. W., 1966, Proc. Roy. Soc. A292, 343.
- Steeds, J. W., and Hazzledine, P. M., Discussions of the Faraday Society #38, Dislocations in Solids, 103.
- Tetelman, A. S., 1962, Acta Met. 10, 813.
- Addendum
- Chen, Gilman and Head (1964) Journ. App. Phys 35, 2502
- Mitchell, I. A., 1964, Phil. Mag. 10, 315.

## APPENDIX I

### FORMATION OF DIPOLES:

#### A DESCRIPTION OF 2 FUNDAMENTAL MECHANISMS

Ignoring, for the moment, dipoles formed by the interaction of partial dislocations, it seems generally accepted that there are two possible modes of dipole formation: those involving cross-slip (Gilman (1962); Fourie(1964)); and those resulting from the interaction of dislocations on parallel slip planes (Tetelman(1962)).

The cross-slip mechanisms are relatively straightforward, involving jogging of a pure screw dislocation and subsequent immobility of that jog while the screw continues to move, dragging out edge components as shown in Figure AI-1. The dipoles so produced should be elongated in the  $\bar{1}\bar{2}1$  direction, and such dipoles are in fact observed in the fatigue microstructures (Johnson and Gilman mechanism).

Now consider the geometry of the Tetelman mechanism (Fig. AI-2). If the two passing dislocations are of approximately the same proportion of edge and screw components, then each will twist approximately the same amount and the dipole will lie at an angle bisecting the angle between the 2 parent dislocations. However, one of the necessary conditions for the Tetelman mechanism is that one of the parent dislocations must be close to pure screw orientation. This is needed to provide the cross-slip process to pinch off the ends of the dipole. Now this prerequisite complicates the geometry, since, as suggested by Steeds and

Hazzledine (1964) and proven by Brown (same publication), the edges will twist more than the screws in this sort of interaction. This means that the dipoles apparently lie closer to the screw line ( $\frac{a}{2}[\bar{1}01]$ ) than to the edge line ( $[\bar{1}\bar{2}1]$ ) (See Figure A1-3).

Now from the micrographs, the dipoles lie along  $[\bar{1}\bar{2}1]$  directions (for primary dipoles) Tetelman observes that the dipole in an unstressed specimen are almost always pure edge while those in a stressed sample are sometimes not pure edge. He concludes: "the mixed dipole can shorten its length and hence lower its energy, by gliding into pure edge orientation". The mixed dipole can retain its sense if some sort of stress acting on one of the short ends restrains its from rotating into a pure edge configuration. If the mixed dipoles do rotate as Tetelman suggests, then the set of dipoles should lie along  $[\bar{1}\bar{2}1]$  if they are  $\frac{a}{2}[\bar{1}01]$  type, and along  $[\bar{1}\bar{1}\bar{2}]$  if they are  $\frac{a}{2}[\bar{1}\bar{1}0]$ . This is verified from the micrographs showing both sets in some Burgers vector determination. Hence the fact that the dipoles formed by both mechanisms lie in an edge orientation, together with the observations that two sets of dipoles along  $[\bar{1}\bar{2}1]$  and  $[\bar{1}\bar{1}\bar{2}]$  of primary and coplanar Burgers vector respectively occur in the crystal, indicates that the two systems are active from early in hardening.

MOTION OF DISLOCATION

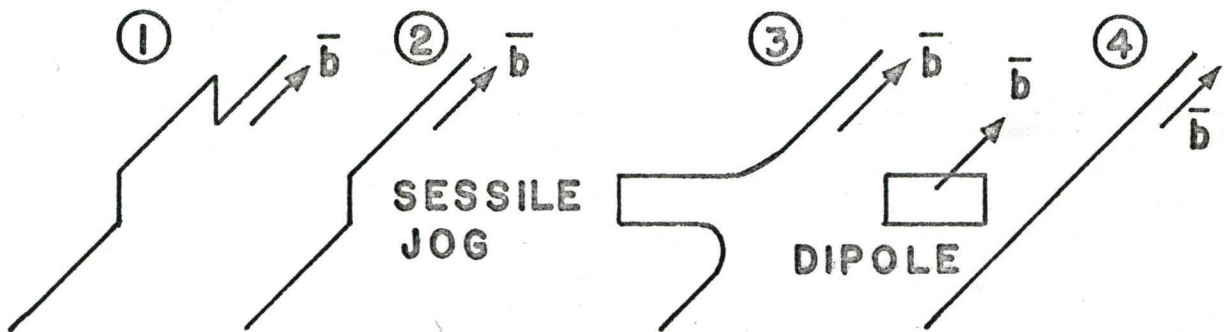


FIGURE AI-1

DIPOLE FORMATION ACCORDING TO FOURIE (1964)

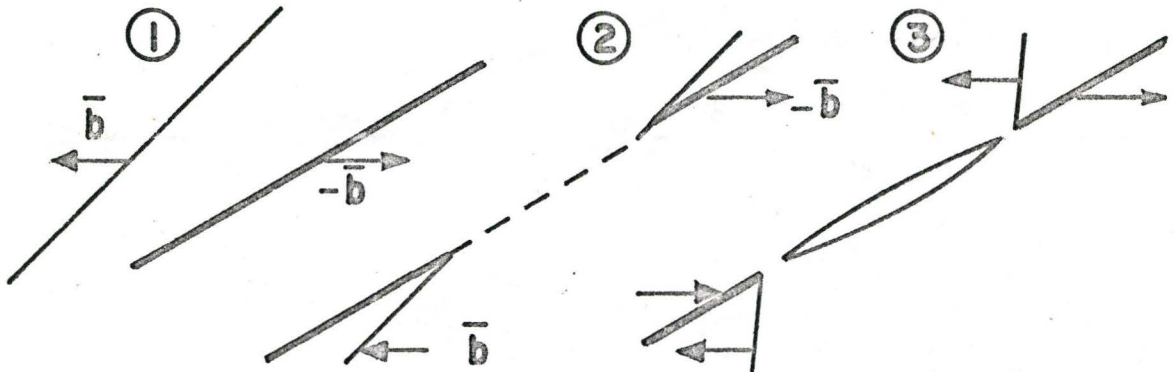


FIGURE AI-2

DIPOLE FORMATION ACCORDING TO TETELMAN (1962)

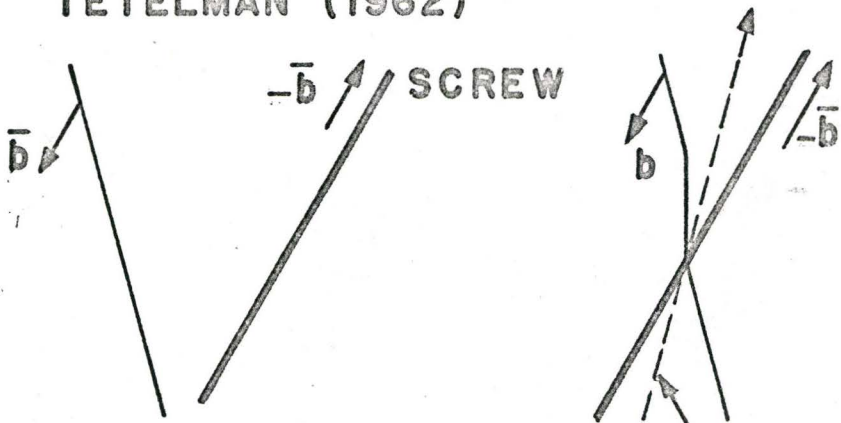


FIGURE AI-3

RESULTANT  
DIPOLE ORIENTATION

## APPENDIX 2

### BURGERS VECTOR ANALYSIS

In electron microscopy, the images observed on the final screen are simply magnified versions of the intensity distribution of electrons leaving the bottom surface of the specimen. The theory of analysis of Burgers vectors of dislocations depends upon the effect that atom displacements in the region of a dislocation have on the intensity distribution of electrons in the foil. There are two approaches to the problem of predicting such an intensity distribution: the kinematical theory and the dynamical theory. Rather than attempt an outline of either approach, an attempt which necessarily would be incomplete and insufficient, the results which are pertinent to dislocation contrast will be stated and their significance explained. An excellent and complete development of these theories is given by Hirsch, Howie, Nicholson, Pashley and Whelan (1965).

Kinematical theory shows that the amplitude of the scattered wave at the bottom surface of the crystal is

$$\phi_g = \frac{i\pi}{\xi_g} \int_0^t e^{-2\pi i \bar{g} \cdot \bar{R}} e^{-2\pi i s z} dz \quad (\text{Hirsch et al. 1965, p.163})$$

The various terms are unimportant with exception of the factor  $e^{-2\pi i \bar{g} \cdot \bar{R}}$ . It is seen that the scattered amplitude  $\phi_g$  is zero if  $e^{-2\pi i \bar{g} \cdot \bar{R}}$  is zero or if in fact  $\bar{g} \cdot \bar{R} = 0$ .

Now  $\bar{g}$  is the operating reflection and  $\bar{R}$  is the displacement of the crystal in the region of the imperfection. The expression developed from kinematical theory shows that if the displacement  $\bar{R}$  is normal to the operating reflection  $\bar{g}$ , no contrast is produced. Also, the maximum contrast is expected when  $\bar{g}$  is parallel to  $\bar{R}$ .

If we consider a screw dislocation, the displacement is given by

$$\bar{R} = \frac{b\phi}{2\pi} = \frac{\bar{b}}{2\pi} \tan^{-1} \frac{(z-y)}{x}$$

where  $\tan^{-1} \frac{(z-y)}{x}$  is the spatial coordinate relative to the dislocation of interest.

Now the condition  $\bar{g} \cdot \bar{R} = 0$  equivalently represented by  $\bar{g} \cdot \bar{b} = 0 \dots$  The condition  $\bar{g} \cdot \bar{b} = 0$  then means that  $\bar{b}$  lies in the plane whose normal is  $\bar{g}$ . Provided that one can narrow the Burgers vector type down to a few, such as  $\frac{a}{2}[110]$  types, then it is generally possible to determine the Burgers vector by examining the trace of the plane whose normal is  $\bar{g}$ , and determining the allowed  $\bar{b}$  values which lie in that trace.

For the case of a general dislocation, containing both screw and edge components, the displacement vector is

$$\bar{R} = \frac{1}{2\pi} \left\{ \bar{b}_\phi + \bar{b}_e \frac{\sin 2\phi}{4(1-\nu)} + \bar{b} \times \bar{u} \left( \frac{1-2\nu}{2(1-\nu)} \ln|r| + \frac{\cos 2\phi}{4(1-\nu)} \right) \right\}$$

where  $b_e$  is the edge component of the dislocation

$\bar{u}$  is the unit vector along the position direction of the dislocation line

$\phi$  is the angle from  $\bar{b}$ , measured in the plane normal to the dislocation

For the case of a pure edge,  $b_e = b$  and if the condition  $\bar{g} \cdot \bar{b} = 0$  is satisfied, then the first 2 terms of  $\bar{g} \cdot \bar{R}$  are zero, but we get a residual factor  $\bar{g} \cdot \bar{b} \times \bar{u}$  ( ).

Now  $\bar{g} \cdot \bar{b} \times \bar{u}$  is zero only if the slip plane is the plane normal to the beam, in this case,  $\bar{b}$  lies in the plane,  $\bar{u}$  lies in the plane, so  $(\bar{b} \times \bar{u})$  lies along the beam axis. Therefore  $\bar{g} \cdot \bar{b} = 0$ .

In general, however, the slip plane is at some angle to the beam other than  $90^\circ$ . This results in a residual image on the final screen even when  $\bar{g} \cdot \bar{b} = 0$ , if the dislocation is an edge.

However,  $\bar{b}$  can still be determined if one is aware that an edge generally leaves such a faint image on the final photograph.

### APPENDIX 3 CALCULATIONS

The tentative hardening sequence given above shows that three interactions are important in determining hardening rate: the dipole-Lomer-Cottrell lock interaction and the dipole-Frank interaction and dipole-forest. In order to more quantitatively evaluate the relative importance of the Lomer-Cottrell lock and the Frank sessile in fatigue hardening, calculations which give expressions for elastic interactions with dipoles are given.

The calculation has 2 steps: (a) the elastic interactions between an infinite length of edge on an infinite length of Lomer-Cottrell or Frank is calculated by the Bullough and Sharp<sup>(5)</sup> method; (b) the Makin and Sharp approximation to calculate stresses on dipoles is used to calculate stress on a dipole of a given length in a pure edge configuration.

#### Lomer Lock: Dipole Interaction

If the slip system is  $[\bar{1}01]$  (111), then the Lomer lock is of the form  $\frac{a}{2}[\bar{1}10]$  for which the Lomer dislocation line lies along  $[\bar{1}\bar{1}0]$ . The primary glide edge lies along the line given by  $[\bar{1}01] \times [111] = [\bar{1}\bar{2}1]$ . The angle between the dislocation lines is  $\frac{\pi}{6} = 30^\circ$ .

Consider dislocation (1) to be the glide edge and  $x_1x_3$  the glide plane (111). Then  $\alpha = \frac{\pi}{6}$  (Following Bullough and Sharp<sup>(5)</sup>).

LOMER LOCK : DIPOLE INTERACTION.

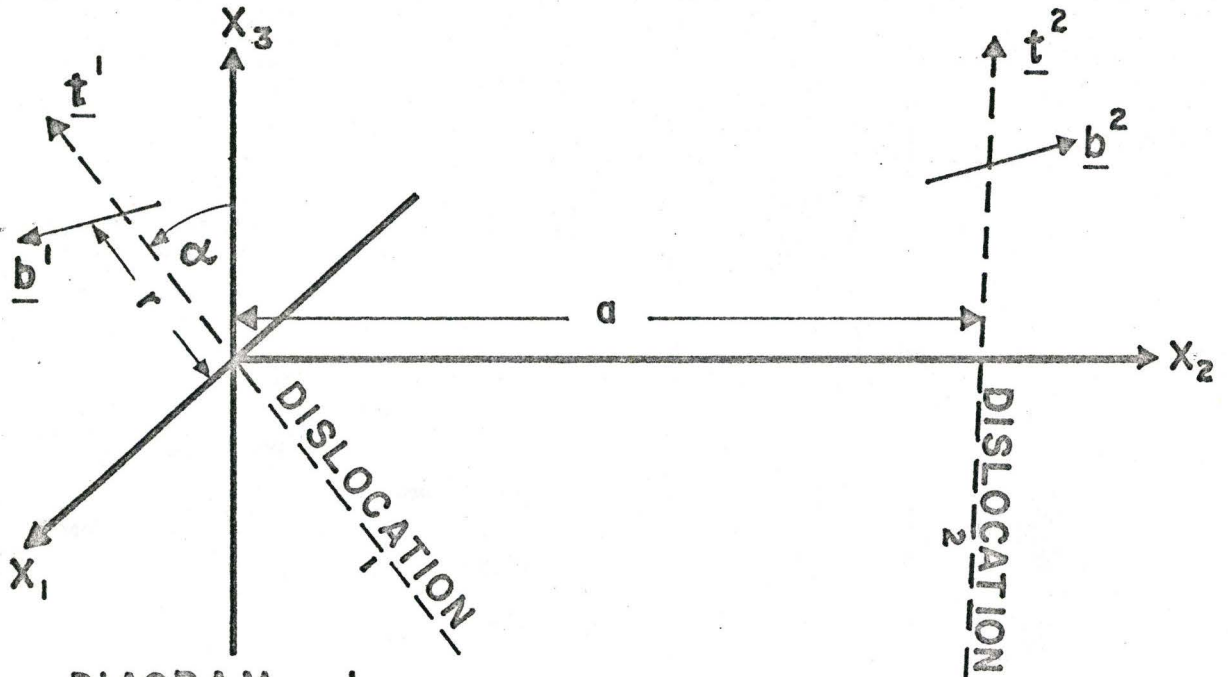


DIAGRAM - 1.

SHOWING THE RELATIVE POSITION OF TWO GENERAL DISLOCATIONS.

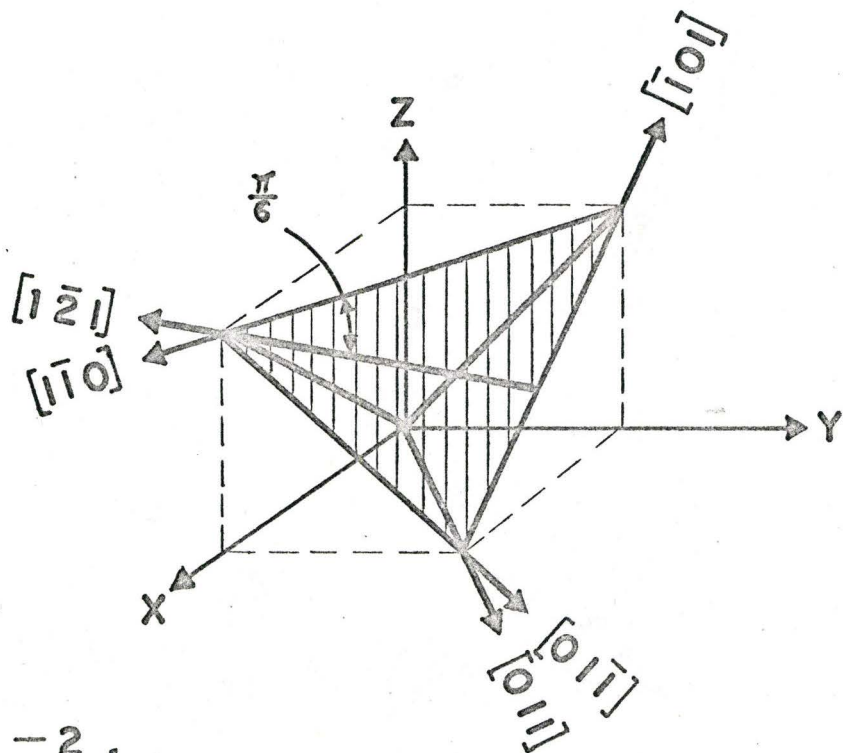


DIAGRAM - 2 .

SHOWING THOMPSON'S TETRAHEDRON.

$$\cos \alpha = \frac{\sqrt{3}}{2}$$

$$\sin \alpha = \frac{1}{2}$$

$$\underline{t}^{(1)} = [1\bar{2}1]$$

$$\underline{t}^{(2)} = (1\bar{1}0)$$

$$b^{(1)} = \frac{a}{2}[\bar{1}01] \rightarrow b_1^{(1)} = -1, b_2^{(1)} = 0, b_3^{(1)} = 1$$

$$b^{(2)} = \frac{a}{2}[110] \rightarrow b_1^{(2)} = 1, b_2^{(2)} = 1, b_3^{(2)} = 0$$

Making these substitutions into the force expressions given by Bullough and Sharp for the configuration shown in diagram (1), we obtain the following

$$\begin{aligned} F_1 &= \left[ \frac{\mu}{2\pi(1-\nu)} \right] L^2 \frac{\sqrt{3}}{2} \left[ -b^2 r K \left( \frac{1}{2} \right) + b^2 a K \right] \\ &= \left[ \frac{\mu}{2\pi(1-\nu)} \right] \frac{1}{\left[ \frac{r^2}{4} + a^2 \right]^2} \left( \frac{\sqrt{3}}{2} \right) \left\{ -b^2 r \left( \frac{1}{2} \right) \left( \frac{r^2}{4} - a^2 \right) \right. \\ &\quad \left. + b^2 a \left( \frac{r^2}{4} - a^2 \right) \right\} \\ &= \left[ \frac{\mu b^2}{2\pi(1-\nu)} \right] \frac{1}{\frac{r^2}{4} + a^2} \left[ \frac{r^2}{4} - a^2 \right] \left[ a - \frac{r}{2} \right] \left[ \frac{\sqrt{3}}{2} \right] \\ F_1 &= \frac{\sqrt{3}}{2} \frac{\mu b^2}{2\pi(1-\nu)} \cdot \frac{\frac{r^2}{4} - a^2}{\left( \frac{r^2}{4} + a^2 \right)^2} \left( a - \frac{r}{2} \right) \\ F_2 &= - \left[ \frac{\mu}{2\pi(1-\nu)} \right] L^2 \left( \frac{\sqrt{3}}{2} \right) \left\{ -b^2 a N - b^2 r K \left( \frac{1}{2} \right) \right\} - \left( \frac{\mu}{2\pi} \right) \{ 0 \} \\ &\quad + \left[ \frac{\mu \nu}{\pi(1-\nu)} \right] \left\{ b^2 a L \left( \frac{1}{2} \right) + b^2 r L \left( \frac{1}{4} \right) \right\} \end{aligned}$$

$$\begin{aligned}
&= - \left[ \frac{\mu}{2\pi(1-\nu)} \right] \frac{1}{\left(\frac{r^2}{4} + a^2\right)^2} \left( \frac{\sqrt{3}}{2} \right) \{ -b^2 \} \\
&\quad \times \left\{ a \left( \frac{3r^2}{4} + a^2 \right) + \frac{r}{2} \left( \frac{r^2}{4} - a^2 \right) \right\} \\
&+ \left[ \frac{\mu \nu}{\pi(1-\nu)} \right] \{ b^2 \} \left\{ \left( \frac{a}{2} \right) \frac{1}{\left(\frac{r^2}{4} + a^2\right)} + \frac{r}{4} \frac{1}{\left(\frac{r^2}{4} + a^2\right)} \right\} \\
F_2 &= \left( \frac{\sqrt{3}}{2} \right) \left[ \frac{\mu b^2}{2\pi(1-\nu)} \right] \left\{ \frac{a \left( \frac{3r^2}{4} + a^2 \right) + \frac{r}{2} \left( \frac{r^2}{4} - a^2 \right)}{\left(\frac{r^2}{4} + a^2\right)^2} \right\} \\
&\quad + \left[ \frac{\mu \nu b^2}{\pi(1-\nu)} \right] \frac{1}{\left(\frac{r^2}{4} + a^2\right)} \left\{ \frac{a}{2} + \frac{r}{4} \right\} \\
F_3 &= - \left[ \frac{\mu}{2\pi(1-\nu)} \right] L^2 \left( \frac{1}{2} \right) \{ -b^2 r k \cdot \frac{1}{2} + b^2 a k \} \\
&= - \left[ \frac{\mu}{2\pi(1-\nu)} \right] \frac{1}{\left(\frac{r^2}{4} + a^2\right)^2} \cdot \left( \frac{1}{2} \right) \cdot b^2 \left\{ \frac{r^2}{4} - a^2 \right\} \cdot \left\{ a - \frac{r}{2} \right\} \\
F_3 &= - \left( \frac{1}{2} \right) \frac{\mu b^2}{2\pi(1-\nu)} \frac{\left(\frac{r^2}{4} - a^2\right)}{\left(\frac{r^2}{4} + a^2\right)^2} \cdot \left\{ a - \frac{r}{2} \right\}
\end{aligned}$$

$F_1$ ,  $F_2$ ,  $F_3$  as calculated above are the forces acting on a glide edge (1) due to the Lomer lock (2). Now since  $x_1 x_3$  is the slip plane and  $\alpha = \frac{\pi}{6}$ , then the angle  $\beta$  between the burgers vector  $\frac{a}{2}[\bar{1}01]$  and the  $x_1$  axis is  $\left(\frac{\pi}{6}\right)$  and the angle between  $\frac{a}{2}[\bar{1}01]$  and the  $x_3$  axis is  $\left(\frac{2\pi}{3}\right)$ .

The force acting along the primary slip direction on the primary edge (1) is then the vector sum of the  $z$  components  $F_1$  and  $F_3$ .

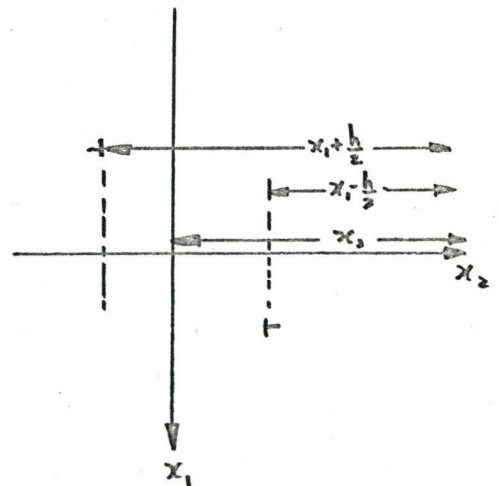
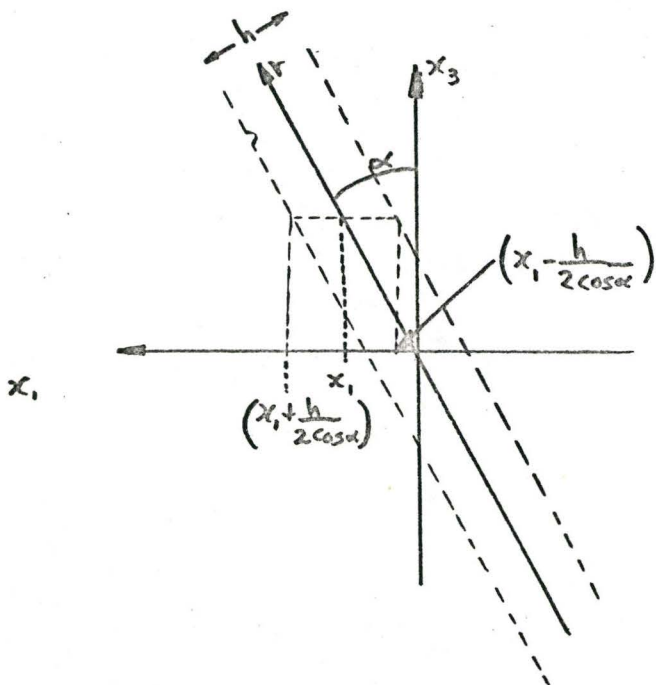
$$F_{[\bar{1}01]} = F_1 \cos \frac{\pi}{6} - F_3 \cos \frac{\pi}{3}$$

$$F_{\bar{1}01} = \frac{1}{2} F_1 - \frac{\sqrt{3}}{2} F_3$$

Substituting from expressions for  $F_1$  and  $F_3$

$$F_{\bar{1}01} = \frac{\sqrt{3}}{4} \frac{\mu b^2}{2\pi(1-\nu)} \frac{\frac{r^2}{4} - a^2}{\left(\frac{r^2}{4} + a^2\right)^2} \left(a - \frac{r}{2}\right) + \frac{\sqrt{3}}{4} \frac{\mu b^2}{2\pi(1-\nu)} \frac{\frac{r^2}{4} - a^2}{\left(\frac{r^2}{4} + a^2\right)^2} \left(a - \frac{r}{2}\right)$$

$$F_{\bar{1}01} = \frac{\sqrt{3}}{2} \frac{\mu b^2}{2\pi(1-\nu)} \frac{\frac{r^2}{4} - a^2}{\left(\frac{r^2}{4} + a^2\right)^2} \left(a - \frac{r}{2}\right)$$



Consider the slip plane  $x_1x_3$  for the moment. We now derive an expression for a pair of lines parallel to the edge dislocations lying along  $r$ .

$$x_1^1 = x_1 \pm \frac{h}{2 \cos \alpha} \quad \text{for either arm of the dipole}$$

$$\text{For } x_1^1 = x_1 + \frac{h}{2 \cos \alpha}, \quad a = x_2 - \frac{h}{2} \quad \left( \text{these values of } a \text{ derived from } x_1x_2 \text{ plane above} \right)$$

$$x_1^1 = x_1 - \frac{h}{2 \cos \alpha}, \quad a = x_2 + \frac{h}{2}$$

$$\text{Now, } x_1 = r \cos \frac{\pi}{3} = \frac{1}{2} r$$

$$\therefore r = 2x_1 \quad \text{and}$$

$$F_{[\bar{1}01]} = \frac{\sqrt{3}}{4} \frac{\mu b^2}{\pi(1-\nu)} \frac{(x_1^2 - a^2)}{(x_1^2 + a^2)^2} (a - x_1)$$

For a dipole of infinite length  $x_1^1 = x_1 \pm \frac{h}{2 \cos \alpha}$  as given below. Substitute these coordinates and take a vector sum for the 2 arms of the dipole according to the Makin and Sharp approximation.

$$F_{\text{DIPOLE}} = \left[ \frac{\sqrt{3}}{4} \frac{\mu b^2}{\pi(1-\nu)} \right] \left[ (x_2 - \frac{h}{2}) - (x_1 + \frac{h}{2 \cos \alpha}) \right] \frac{[(x_1 + \frac{h}{2 \cos \alpha})^2 - (x_2 - \frac{h}{2})^2]}{[(x_1 + \frac{h}{2 \cos \alpha})^2 + (x_2 - \frac{h}{2})^2]^2}$$

$$- \left[ \frac{\sqrt{3}}{4} \frac{\mu b^2}{\pi(1-\nu)} \right] \left[ (x_2 + \frac{h}{2}) - (x_1 - \frac{h}{2 \cos \alpha}) \right] \frac{[(x_1 - \frac{h}{2 \cos \alpha})^2 - (x_2 + \frac{h}{2})^2]}{[(x_1 - \frac{h}{2 \cos \alpha})^2 + (x_2 + \frac{h}{2})^2]^2}$$

But this expression considers the force/unit length at a particular point  $(x_1x_2)$  on the dipole (Note that the set angle  $\alpha = \frac{\pi}{6}$  means the third dimension parameter  $x_3$  is redundant and each point on the dipole is totally specified by  $(x_1x_2)$  ).

In order to get the force on a finite length of dipole, there are 3 possibilities: 1) approximate the force as the average value from centre to end; 2) approximate the force to stop the dipole as the maximum force acting on the dipole since the dipoles are relatively short and cannot bow around any obstacle to a significant extent. The dipole is then effectively pinned at its strongest point; 3) integrate  $F_{\text{DIPOLE}}$  over  $l_1 > r > l_2$  to get the analytical expression for the total force on a dipole extending from  $l_1$  to  $l_2$ .

This integration method would yield a more precise force value but the absolute accuracy of this with respect to the real values involved would probably be no better than the approximations 1) - 2) above. That is: the basic limitations here are not in the integration or approximations at this stage, but rather in the model itself -- essentially an idealized configuration useful only for order of magnitude calculations.

We shall assume here the approximation (2):

$$\text{force on dipole of length "l"} = (\text{maximum stress on dipole}) \left(\frac{1}{2} l\right)$$

The justification of this approximation is that it will certainly be correct to the order of magnitude, and this is all that is required here.

In order to find the exact direction in which the maximum stress occurs, we must plot  $F_{\text{DIPOLE}}$  vs  $x_1$  and  $x_2$  around the dislocation (2) (Lomer lock) as origin. This would yield a set of constant stress lines similar to those of Sharp and Makin<sup>(19)</sup>. This is possible only by

machine calculation and hence remains as a possible extension to this problem.

In lieu of this consider the geometry of the situation to obtain a rough idea of what the maximum stress line is like. The Makin and Sharp paper suggests a maximum stress line almost exactly along the  $x_2$ -axis. This neglects the relative tilt of the two dislocation lines, but let us approximate the maximum stress line along  $x_2$  (refer to Makin and Sharp<sup>(19)</sup>)

$$\begin{aligned}
 &\text{Consider } x_1 = 0 \\
 F_{\text{DIPOLE}} = & \left[ \left[ \left( x_2 - \frac{h}{2} \right) - \left( \frac{h}{2\sqrt{3}} \right) \right] \frac{\left[ \left( \frac{h}{2\sqrt{3}} \right)^2 - \left( x_2 - \frac{h}{2} \right)^2 \right]}{2} \right. \\
 & \left. \frac{\left[ \left( \frac{h}{2\sqrt{3}} \right)^2 + \left( x_2 - \frac{h}{2} \right)^2 \right]^2}{2} \right] \\
 & + \left[ \left[ \left( x_2 + \frac{h}{2} \right) - \left( \frac{h}{2\sqrt{3}} \right) \right] \frac{\left[ \left( \frac{h}{2\sqrt{3}} \right)^2 - \left( x_2 + \frac{h}{2} \right)^2 \right]}{2} \right. \\
 & \left. \frac{\left[ \left( \frac{h}{2\sqrt{3}} \right)^2 + \left( x_2 + \frac{h}{2} \right)^2 \right]^2}{2} \right]
 \end{aligned}$$

Now in examining the Makin and Sharp interaction curves, we see that for  $h = 200\text{\AA}$  (ie: width of dipole =  $\sqrt{2} h$ ), the maximum distance from the edge at which the sweeping up process can occur is  $\approx 1700\text{\AA}$ . Choose as an average distance  $\frac{1700}{2} = 850\text{\AA} = x_2$ . This is a rough value for the distance a dipole may be if it is being driven along the glide plane by the primary edge.

Looking at the interaction curves for the particular dipole we are considering in this paper, we see that the maximum stress which holds the dipole to the moving edge is  $\sim 22 \times 10^3 \left[ \frac{\mu b^2}{2\pi(1-\nu)} \right]$ .

Equating this force to the force acting on the dipole from a Lomer lock, we get " $x_2$ ", the interaction parameter, at which distance the dipole is locked to the Lomer dislocation and not to the glide edge.

$$\begin{aligned} & \frac{\sqrt{3}}{2} \left[ \frac{\mu b^2}{2\pi(1-\nu)} \frac{1}{2} \right] \left[ \left( x_2 - \frac{h}{2} \right) - \frac{h}{\sqrt{3}} \right] \frac{\left[ \left( \frac{h}{\sqrt{3}} \right)^2 - \left( x_2 - \frac{h}{2} \right)^2 \right]}{\left[ \left( \frac{h}{\sqrt{3}} \right)^2 + \left( x_2 - \frac{h}{2} \right)^2 \right]^2} \\ & + \frac{\sqrt{3}}{2} \left[ \frac{\mu b^2}{2\pi(1-\nu)} \frac{1}{2} \right] \left[ \left( x_2 + \frac{h}{2} \right) - \left( \frac{h}{\sqrt{3}} \right) \right] \frac{\left[ \left( -\frac{h}{\sqrt{3}} \right)^2 - \left( x_2 + \frac{h}{2} \right)^2 \right]}{\left[ \left( \frac{h}{\sqrt{3}} \right)^2 + \left( x_2 + \frac{h}{2} \right)^2 \right]^2} \\ & = \frac{\mu b^2}{2\pi(1-\nu)} (22 \times 10^3) \end{aligned}$$

$$\frac{\sqrt{3}}{4} \left[ \quad \right] \left[ \text{---} \right]_2 + \frac{\sqrt{3}}{4} \left[ \quad \right] \left[ \text{---} \right]_2 = (22 \times 10^3)$$

$$\left[ \quad \right] \left[ \text{---} \right]_2 + \left[ \quad \right] \left[ \text{---} \right]_2 = [22 \times 10^3] \frac{4}{\sqrt{3}}$$

By trial and error, it was found that the stress at a distance of  $500\text{\AA}$ , then  $300\text{\AA}$ , then  $200\text{\AA}$  was insufficient to overcome the force attacking the dipole to the edge. The dipole width was about  $200\text{\AA}$ , so  $\frac{h}{2} = 100\text{\AA}$ . This meant that the dipole must come within  $100\text{\AA}$  of the Lomer lock before anything appreciable happens. The implication is that virtually physical intersection of the dipole and lock must occur before the dipole is deposited at the lock.

#### Frank Sessile: Dipole Interactions

In a way entirely analogous to that for the Lomer lock, we find

$$b^{(1)} = \frac{a}{2} [\bar{1}01] \quad b^{(2)} = \frac{a}{3} [\bar{1}\bar{1}1]$$

$$\begin{cases} \alpha = 30^\circ \\ \cos \alpha = \frac{\sqrt{3}}{2} \\ \sin \alpha = \frac{1}{2} \end{cases}$$

The particular values were chosen from reference to Hirsch's mechanism<sup>(14)</sup> for extending a trailing dipole to produce Franck dislocations along the dipole edges.

$$\begin{aligned} F_1 &= \left[ \frac{\mu}{2\pi(1-\nu)} \right] L^2 \left( \frac{\sqrt{3}}{2} \right) \left\{ \frac{2}{3} b^2 r K \left( \frac{1}{2} \right) - \frac{2}{3} b^2 a K \left( \frac{1}{2} \right) \right\} \\ &\quad + \left[ \frac{\mu}{2\pi} \right] \frac{2}{3} b^2 L r \left( \frac{\sqrt{3}}{4} \right) \\ &= \frac{\mu}{2\pi(1-\nu)} \frac{1}{\left( \frac{r^2}{4} + a^2 \right)^2} \left( \frac{\sqrt{3}}{2} \right) \left\{ \frac{1}{3} b^2 r - \frac{2}{3} b^2 a \right\} \left\{ \frac{r^2}{4} - a^2 \right\} \\ &\quad + \frac{\mu}{2\pi} \left( \frac{2}{3} \right) b^2 \frac{1}{\left( \frac{r^2}{4} + a^2 \right)} r \frac{\sqrt{3}}{4} \\ F_1 &= \left[ \frac{\mu b^2}{2\pi(1-\nu)} \right] \frac{\left( \frac{r^2}{4} - a^2 \right)}{\left( \frac{r^2}{4} + a^2 \right)^2} \frac{\sqrt{3}}{2} \left\{ r - \frac{2}{3} a \right\} + \frac{1}{2\sqrt{3}} \left[ \frac{\mu b^2}{2\pi} \right] \frac{r}{\left( \frac{r^2}{4} + a^2 \right)} \end{aligned}$$

$$\begin{aligned} F_2 &= \left[ \frac{\mu}{2\pi(1-\nu)} \right] L^2 \left( \frac{\sqrt{3}}{2} \right) \left\{ \frac{2}{3} b^2 a N \left( \frac{1}{2} \right) + \frac{2}{3} b^2 r K \left( \frac{1}{2} \right) \right\} \\ &\quad - \left[ \frac{\mu}{2\pi} \right] \left\{ \frac{2}{3} b^2 L a \left( \frac{\sqrt{3}}{2} \right) - \frac{2}{3} b^2 a L \left( \frac{1}{2} \right) \right\} \\ &\quad + \left[ \frac{\mu \nu}{\pi(1-\nu)} \right] \left\{ - \frac{2}{3} b^2 a L \left( \frac{1}{2} \right) - \frac{2}{3} b^2 r L \left( \frac{1}{4} \right) \right\} \\ &= - \left[ \frac{\mu}{2\pi(1-\nu)} \right] \frac{1}{\left( \frac{r^2}{4} + a^2 \right)^2} \left( \frac{\sqrt{3}}{2} \right) \left\{ \frac{2}{3} b^2 a \left( \frac{3}{4} r^2 + a^2 \right) \right. \\ &\quad \left. + \frac{1}{3} b^2 r \left( \frac{r^2}{4} - a^2 \right) \right\} \end{aligned}$$

$$- \left(\frac{\mu}{2\pi}\right) \left\{ \frac{1}{\sqrt{3}} b^2 a \frac{1}{\left(\frac{r^2}{4} + a^2\right)} - \frac{1}{3} b^2 a \frac{1}{\left(\frac{r^2}{4} + a^2\right)} \right\}$$

$$+ \left[ \frac{\mu v}{\pi(1-v)} \right] \left\{ -\frac{1}{3} b^2 a \frac{1}{\left(\frac{r^2}{4} + a^2\right)} - \frac{1}{6} b^2 r \frac{1}{\left(\frac{r^2}{4} + a^2\right)} \right\}$$

$$F_2 = - \left[ \frac{\mu b^2}{2\pi(1-v)} \right] \frac{1}{\left(\frac{r^2}{4} + a^2\right)^2} \left(\frac{1}{2\sqrt{3}}\right) \left\{ 2a \left(\frac{3}{4} r^2 + a^2\right) + r \left(\frac{r^2}{4} - a^2\right) \right\}$$

$$- \left[ \frac{\mu b^2}{\pi(1-v)} \right] \left\{ \frac{1}{\left(\frac{r^2}{4} + a^2\right)} \right\} \left\{ \frac{1}{\sqrt{3}} + \frac{1}{3} \right\}$$

$$- \left[ \frac{\mu v b^2}{\pi(1-v)} \right] \left\{ \frac{1}{\left(\frac{r^2}{4} + a^2\right)} \right\} \left\{ \frac{a}{3} + \frac{r}{6} \right\}$$

$$F_3 = - \left[ \frac{\mu}{2\pi(1-v)} \right] L^2 \left(\frac{1}{2}\right) \left\{ \frac{2}{3} b^2 r K \left(\frac{1}{2}\right) - \frac{2}{3} b^2 a K \right\}$$

$$- \left[ \frac{\mu}{2\pi} \right] \left(\frac{2}{3}\right) b^2 r L \left(\frac{1}{4}\right)$$

$$= - \left[ \frac{\mu b^2}{2\pi(1-v)} \right] \frac{1}{\left(\frac{r^2}{4} + a^2\right)^2} \left\{ \frac{r}{6} \left(\frac{r^2}{4} - a^2\right) - \frac{a}{3} \left(\frac{r^2}{4} - a^2\right) \right\}$$

$$- \left[ \frac{\mu b^2}{2\pi} \right] \frac{1}{6} b^2 r \frac{1}{\left(\frac{r^2}{4} + a^2\right)}$$

$$F_3 = - \left[ \frac{\mu b^2}{2\pi(1-v)} \right] \frac{\left(\frac{r^2}{4} - a^2\right)}{\left(\frac{r^2}{4} + a^2\right)^2} \left\{ \frac{r}{3} - \frac{2a}{3} \right\} \left(\frac{1}{2}\right)$$

$$- \frac{1}{6} \left[ \frac{\mu b^2}{2\pi} \right] \frac{r}{\left(\frac{r^2}{4} + a^2\right)}$$

Now, similar to that for Lomer locks, find force along  $[\bar{1}01]$ . Since  $\alpha = 30^\circ$  again, we have a similar expression,

$$\begin{aligned}
 F_{\bar{1}01} &= \frac{1}{2} F_1 - \frac{\sqrt{3}}{2} F_3 \\
 F_{\bar{1}01} &= \left[ \frac{\mu b^2}{2\pi(1-\nu)} \right] \frac{\left[ \frac{r^2}{4} - a^2 \right]}{\left[ \frac{r^2}{4} + a^2 \right]^2} \left\{ \frac{r}{3} - \frac{2}{3} a \right\} \left[ \left\{ \frac{1}{2} \frac{\sqrt{3}}{2} \right\} + \left\{ \frac{\sqrt{3}}{2} \frac{1}{2} \right\} \right] \\
 &\quad + \left[ \frac{\mu b^2}{2\pi} \right] \frac{r}{\left( \frac{r^2}{4} + a^2 \right)} \left\{ \frac{1}{4\sqrt{3}} + \frac{\sqrt{3}}{12} \right\} \\
 &= \frac{\sqrt{3}}{4} \left[ \frac{\mu b^2}{2\pi(1-\nu)} \right] \frac{\left[ \frac{r^2}{4} - a^2 \right]}{\left[ \frac{r^2}{4} + a^2 \right]^2} \left\{ \frac{r}{3} - \frac{2}{3} a \right\} + \left[ \frac{\mu b^2}{2\pi} \right] \frac{r}{\left( \frac{r^2}{4} + a^2 \right)} \left\{ \frac{1}{2\sqrt{3}} \right\}
 \end{aligned}$$

Substitute  $r = 2x_1$  (for  $\alpha = 30^\circ$ )

$$F_{\text{DIPOLE}} = \frac{\sqrt{3}}{4} \left[ \frac{\mu b^2}{2\pi(1-\nu)} \right] \frac{(x_1^2 - a^2)}{(x_1^2 + a^2)^2} \left\{ \frac{2}{3} x_1 - \frac{2}{3} a \right\} + \left( \frac{\mu b^2}{2\pi} \right) \frac{2x_1}{(x_1^2 + a^2)} \left\{ \frac{1}{2\sqrt{3}} \right\}$$

$$\text{Substitute } x_1^1 = x_1 + \frac{h}{2\cos\alpha}, \quad a = x_2 - \frac{h}{2}$$

$$x_1^1 = x_1 - \frac{h}{2\cos\alpha}, \quad a = x_2 + \frac{h}{2}$$

$$\begin{aligned} F_{\text{DIPOLE}} = & \frac{\sqrt{3}}{4} \left[ \frac{\mu b^2}{2\pi(1-\nu)} \right] \frac{(x_1 + \frac{h}{2\cos\alpha})^2 - (x_2 - \frac{h}{2})^2}{[(x_1 + \frac{h}{2\cos\alpha})^2 + (x_2 - \frac{h}{2})^2]^2} \left\{ x_1 + \frac{h}{2\cos\alpha} - x_2 + \frac{h}{2} \right\} \frac{2}{3} \\ & + \left( \frac{\mu b^2}{2\pi} \right) \frac{2(x_1 + \frac{h}{2\cos\alpha})}{[(x_1 + \frac{h}{2\cos\alpha})^2 + (x_2 - \frac{h}{2})^2]} \left\{ \frac{1}{2\sqrt{3}} \right\} \\ - & \frac{\sqrt{3}}{4} \left[ \frac{\mu b^2}{2\pi(1-\nu)} \right] \frac{(x_1 - \frac{h}{2\cos\alpha})^2 - (x_2 + \frac{h}{2})^2}{[(x_1 - \frac{h}{2\cos\alpha})^2 + (x_2 + \frac{h}{2})^2]^2} \left\{ x_1 - \frac{h}{2\cos\alpha} - x_2 - \frac{h}{2} \right\} \frac{2}{3} \\ - & \left( \frac{\mu b^2}{2\pi} \right) \frac{2(x_1 - \frac{h}{2\cos\alpha})}{[(x_1 - \frac{h}{2\cos\alpha})^2 + (x_2 + \frac{h}{2})^2]} \left\{ \frac{1}{2\sqrt{3}} \right\} \end{aligned}$$

Again, if we let  $x_1 = 0$ ,  $h = 200\text{\AA}$  and  $x_2 = 200\text{\AA}$ , we get very small values for  $F_{\text{DIPOLE}}$ . The implication again is that the intersection of dipole and Frank must occur before locking can take place.

However, in both this case and the former case, we must be careful not to draw too definite conclusions. The Makin and Sharp interaction curves show particular directions which have virtually zero stress until a very short distance from the dipole. The only way one

can be sure that one is not considering a similar zero stress line in either of the above cases is to plot out a complete interaction curve in three dimensions. (The third dimension is necessary in these cases because the dipole and dislocation are non-parallel and hence the interaction curves vary along  $x_3$ ,  $x_2$  and  $x_1$ ).

APPENDIX 3

BIBLIOGRAPHY

- (5) Sharp and Bullough, Phil. Mag. 11, 605
- (14) Hirsch and Steeds, N.P.L. #15, January 1963, 48
- (19) Makin and Sharp, Phil. Mag. 10, 1011 (1964)